Dynamical Electroweak Symmetry Breaking on the Lattice

Liam Keegan

A thesis submitted in fulfilment of the requirements
for the degree of Doctor of Philosophy
to the
University of Edinburgh
20th May 2011

Abstract

The LHC is expected to find new physics beyond the Standard Model (BSM). Technicolor models are a class of BSM models which involve a new strongly interacting sector responsible for electroweak symmetry breaking (EWSB). The phenomenological viability of these models depends on features such as the existence of an infrared fixed point (IRFP) at strong coupling, and the size of the mass anomalous dimension at this fixed point. As these features are at strong coupling they are not accessible to perturbative methods, and so need to be investigated non–perturbatively using lattice methods.

In this thesis, two candidate Technicolor theories are investigated using two independent and complementary lattice methods, the Schrödinger Functional (SF) and the Monte Carlo Renormalisation Group (MCRG), to measure the running of the coupling and the anomalous mass dimension in these theories.

Declaration

Except where otherwise stated, the research undertaken in this thesis was the unaided work of the author. Where the work was done in collaboration with others, a significant contribution was made by the author. For the results presented in Chapter 3, I modified the HiRep RHMC code to implement Schrödinger Functional boundary conditions and observables, wrote the bootstrap analysis code, and performed the analysis and the majority of the running. For the results presented in Chapter 4, I wrote the blocking routines and observables, performed the running of the code and the analysis.

The results presented in Chapter 3 are published in:
F. Bursa, L. Del Debbio, L. Keegan, C. Pica and T. Pickup.
"Mass anomalous dimension in SU(2) with two adjoint fermions."
Phys. Rev. D **81**, 014505 (2010). arXiv:0910.4535 [hep-ph].

F. Bursa, L. Del Debbio, L. Keegan, C. Pica and T. Pickup.
"Mass anomalous dimension in SU(2) with six fundamental fermions."
Phys. Lett. B **696**(4), 374 (2011). arXiv:1007.3067 [hep-ph].

Some of the results presented in Chapter 4 are published in:
S. Catterall, L. Del Debbio, J. Giedt and L. Keegan.
"MCRG Minimal Walking Technicolor."
PoS **LATTICE2010** 057 (2010). arXiv:1010.5909 [hep-ph].

Liam Keegan
20$^{\text{th}}$ May 2011

Acknowledgements

Firstly I would like to thank my supervisor, Luigi Del Debbio, for his guidance, teaching and enthusiasm over the last four years.

Part of this research was done at Syracuse University, thanks to Simon Catterall for his hospitality and the opportunity to get involved in new projects, not to mention experience a Syracuse winter.

I have also enjoyed working with, and occasionally meeting in person, the rest of my collaborators: Francis Bursa, Joel Giedt, Claudio Pica and Thomas Pickup. I'm also very grateful to Jane Patterson for all her help, and to STFC for funding my research.

Thanks to all the members of PPT in Edinburgh, in particular my office mates Claudia, Eoin, Erik, Gavin and Sam, and happy memories of playing table football in the basement.

Finally, thanks to my parents and Tracey for their love and support.

Contents

List of Figures

List of Tables

Chapter 1

Dynamical Electroweak Symmetry Breaking

1.1 The Standard Model

1.1.1 Introduction

The Standard Model of particle physics [1] is a very successful description of the interactions of elementary particles in nature. It has been extensively experimentally tested and verified over the last thirty years [2]. It consists of a set of spin–1/2 matter fields, the quarks and leptons, which transform under a local SU(3) $\otimes$ SU(2) $\otimes$ U(1) gauge symmetry. Their interactions are mediated by a set of spin–1 gauge bosons. These particles are shown in Fig 1.1.

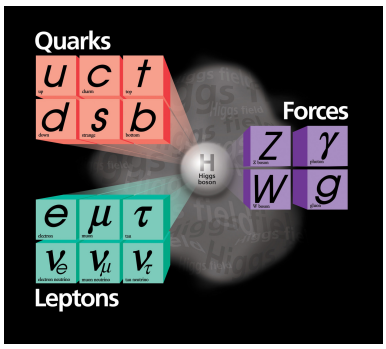

Figure 1.1: Standard Model particle content. Image from Fermilab.

In addition there is a spin–0 particle, the Higgs boson [3, 4, 5], which remains the only particle in the Standard Model yet to be experimentally verified. It

performs two key roles. The first is to spontaneously break the SU(2) ⊗ U(1) electroweak symmetry to U(1), which gives mass to the Z and W bosons via the Higgs mechanism. The second role is to give mass to the matter fields via Yukawa interaction terms in the Lagrangian.

1.1.2 Higgs Mechanism

If a Lagrangian has a global symmetry, but the vacuum expectation value of the field does not respect this symmetry, then it is said to be spontaneously broken. According to the Goldstone theorem [6, 7] each spontaneously broken symmetry gives rise to a massless spin–0 Goldstone boson. For the case of a local, or gauge symmetry, each spontaneously broken symmetry gives a mass to a previously massless gauge boson, which absorbs the corresponding Goldstone boson as a longitudinal degree of freedom.

This is the mechanism used in the Glashow–Weinberg–Salam theory of weak interactions [8, 1, 9] in the Standard Model. The Higgs boson is gauged under SU(2) ⊗ U(1). It is a doublet under SU(2) and has a charge +1/2 under U(1), with the corresponding gauge transformation

$$\phi \rightarrow e^{i\alpha^a \tau^a} e^{i\beta/2} \phi, \tag{1.1}$$

and covariant derivative

$$D_\mu \phi = \left(\partial_\mu - igA^a_\mu \tau^a - i\tfrac{1}{2} g' B_\mu\right) \phi. \tag{1.2}$$

Expanding the kinetic term in the Lagrangian $\frac{1}{2}\left|D_\mu \phi\right|^2$ about the vacuum expectation value $\langle\phi\rangle = (0, v)$ gives three massive gauge bosons, the Z, W^+, W^-, and one massless gauge boson, the photon A [10],

$$\begin{array}{lcllll} W^\pm_\mu & = & \frac{1}{\sqrt{2}}(A^1_\mu \mp iA^2_\mu) & m_W & = & gv/2 \quad \sim 80.4\,\text{GeV} \\ Z^0_\mu & = & \frac{1}{\sqrt{g^2+g'^2}}(gA^3_\mu - g'B_\mu) & m_Z & = & \sqrt{g^2+g'^2}v/2 \quad \sim 91.2\,\text{GeV} \\ A_\mu & = & \frac{1}{\sqrt{g^2+g'^2}}(g'A^3_\mu + gB_\mu) & m_A & = & 0 \end{array} \tag{1.3}$$

where $\frac{g'^2}{g^2+g'^2} = \sin^2\theta_W \sim 0.23$, and $\nu \sim 246\,\text{GeV}$. The non–zero vacuum expectation value of the Higgs also gives masses to the fermions via Yukawa

terms of the form

$$(\lambda_u v)\overline{u}_L u_R, \quad (\lambda_e v)\overline{e}_L e_R. \tag{1.4}$$

1.1.3 Theoretical Issues

The Higgs boson is the simplest way to spontaneously break electroweak symmetry, but there are a number of theoretical issues. The main one is known as the hierarchy problem [11]. Scalar fields are always accompanied by quadratic mass divergences, which means that the physical Higgs mass will naturally tend to be of the order of the Planck scale, $\sim 10^{19}$ GeV. To obtain a physical Higgs mass of the order of a GeV requires the bare mass to be fine–tuned to one part in 10^{38}, wich is considered an unnatural amount of fine–tuning.

Another issue is that the scalar ϕ^4 theory is trivial [12], meaning that without new physics at some higher energy scale the Higgs decouples and becomes non–interacting. Finally, the masses of all the fermions are free Yukawa parameters [13] which are put in by hand, there is no explanation of flavour physics.

This suggests that, while the Standard Model is a very successful low energy effective field theory, the Higgs boson is not a fundamental particle, and there exists some more fundamental theory of electroweak symmetry breaking [14].

1.2 Dynamical EWSB

1.2.1 Technicolor

In fact, even without a Higgs sector, electroweak symmetry is spontaneously broken by the quark condensate [15]

$$\langle \overline{u}_L u_R + \overline{d}_L d_R \rangle \neq 0. \tag{1.5}$$

This gives a mass to the Z and W bosons via the Higgs mechanism, where the absorbed Goldstone bosons are now the massless pions, leading to a mass

$$M_W = \frac{g F_\pi}{2} \sim 29\,\mathrm{MeV}, \tag{1.6}$$

where $F_\pi \sim 93\,\mathrm{MeV}$ is the pion decay constant, but this mass is so small compared to the measured value that its contribution is typically neglected.

The original proposal for Technicolor (TC) [16, 17] was to replace the Higgs sector with a SU(N_{TC}) gauge theory with n_f^{TC} Dirac fermions, or "techni–quarks". The scale of this theory Λ_{TC} is chosen to be much higher than the QCD scale Λ_{QCD}, such that the breaking of electroweak symmetry by the techni–quark condensate gives the experimentally observed gauge boson masses,

$$M_W = \frac{gF_\pi^{TC}}{2} \sim 80\,\text{GeV} \Rightarrow F_\pi^{TC} \sim \Lambda_{TC} \sim v \sim 246\,\text{GeV}. \tag{1.7}$$

Quark masses are generated by interactions between the Standard Model fermions and the techni–quarks. These are mediated by gauge bosons from some larger gauge group known as Extended Technicolor (ETC) [18, 19], which breaks down to the Technicolor gauge group at the scale Λ_{ETC}. The remnants of the ETC group include four–fermion interactions of the form [20]

$$\alpha_{ab}\frac{\overline{Q}_L T^a Q_R \overline{\psi}_L T^b \psi_R}{\Lambda_{ETC}^2} + \beta_{ab}\frac{\overline{\psi}_L T^a \psi_R \overline{\psi}_L T^b \psi_R}{\Lambda_{ETC}^2}, \tag{1.8}$$

where the α terms lead to Yukawa masses of the form

$$m_q \sim \frac{g_{ETC}^2}{\Lambda_{ETC}^2}\langle\overline{Q}Q\rangle_{ETC}, \tag{1.9}$$

where $\langle\overline{Q}Q\rangle_{ETC}$ is the Technicolor condensate at the ETC scale Λ_{ETC}.

1.2.2 Technicolor Problems

Technicolor is an attractive theory, but it was quickly found to have two major problems. The first is that it conflicts with precision electroweak experimental data. The vacuum polarisation effects of new physics on electroweak processes can be parameterised by the three parameters S, T and U [21], where

$$\begin{aligned} \alpha S &\equiv 4e^2\left[\Pi'_{33}(0) - \Pi'_{3Q}(0)\right], \\ \alpha T &\equiv \tfrac{e^2}{s^2c^2m_Z^2}\left[\Pi_{11}(0) - \Pi_{33}(0)\right], \\ \alpha U &\equiv 4e^2\left[\Pi'_{11}(0) - \Pi'_{33}(0)\right], \end{aligned} \tag{1.10}$$

and

$$ig^{\mu\nu}\Pi_{XY}(q^2) + (q^\mu q^\nu \text{ terms}) \equiv \int d^4x e^{-iqx}\langle J_X^\mu(x) J_Y^\nu(0)\rangle. \tag{1.11}$$

These are all zero in the Standard Model, and the experimentally measured values are also consistent with zero, shown for S and T in Fig. 1.2. The Technicolor contribution to these parameters was calculated perturbatively [22, 23], and the S parameter was found to be positive and proportional to the number of techni–quarks and colors,

$$S \simeq 0.25 \frac{n_f^{TC}}{2} \frac{N_{TC}}{3}. \tag{1.12}$$

Even for a single SU(3) doublet of techni–quarks this disagrees with the experimentally measured value $S = 0.01(10)$ [2] by a few sigma, and the disagreement grows as more matter or colors are added.

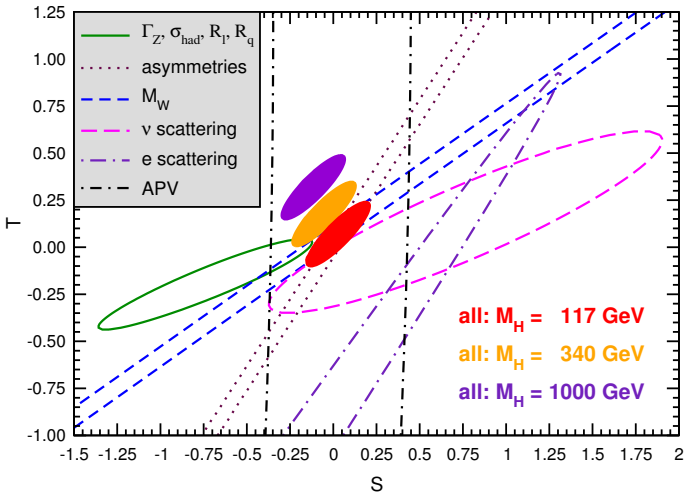

Figure 1.2: S and T parameter experimental fits for the Standard Model with $M_H = 117, 340, 1000\,\text{GeV}$. [2]

The second problem is that of generating realistic quark masses. The difficulty comes from the β terms in Eq. 1.8. These terms induce Flavor Changing Neutral Current (FCNC) interactions amongst the quarks and leptons. These are very well constrained to be small experimentally, and the contribution to the $K_L K_S$ mass difference [18] yields a lower bound on the ETC scale of

$$\Lambda_{ETC} \gtrsim 10^3\,\text{TeV}. \tag{1.13}$$

Even with the optimistic assumptions $\alpha \lesssim 10, N_{TC} \lesssim 10, \Lambda_{TC} \lesssim 1\,\text{TeV}$ this gives an upper bound on the quark masses of

$$m_q \sim \frac{\alpha N_{TC} \Lambda_{TC}^3}{\Lambda_{ETC}^2} \lesssim 100\,\text{MeV}. \tag{1.14}$$

These and other difficulties are discussed in detail in Refs. [20, 24], but it is already clear that Technicolor with QCD–like dynamics is not a viable theory. But what about gauge theories with dynamics that are very different to QCD?

1.2.3 Walking/Conformal Technicolor

One proposal to alleviate the tension between supressing the FCNC contributions, while still generating large enough quark masses, was to have a large ($n_f^{TC} \sim 4N_{TC}$) number of techni–fermions such that the theory is near–conformal [25, 26, 27].

An illustration of the qualitative differences between running, walking and conformal theories is shown in Fig. 1.3. Unlike a running theory, where the gauge coupling becomes large at small scales and the theory becomes confining, in a conformal theory with an IRFP the gauge coupling flows to its constant fixed–point value at small scales, and the theory is no longer confining. A walking theory is a near–conformal theory, where the gauge coupling remains approximately constant over a large range of scales, but eventually becomes large at small scales so that the theory is confining. Thus a walking theory is asymptotically free at high scales and confining at low scales, just as in a running QCD–like theory, but it is quasi-conformal for some intermediate range of scales.

The size of the quark masses in Eq. 1.9 are determined by the size of the Technicolor condensate at the ETC scale, $\langle \overline{Q}Q \rangle_{ETC}$. This is related to the condensate at the TC scale by the anomalous mass dimension γ,

$$\langle \overline{Q}Q \rangle_{ETC} = \exp\left(\int_{\Lambda_{TC}}^{\Lambda_{ETC}} \gamma(g^2(\mu)) d\ln\mu \right) \langle \overline{Q}Q \rangle_{TC}, \tag{1.15}$$

where $g^2(\mu)$ is the gauge coupling. In a QCD–like theory $\gamma \propto g^2(\mu) \propto 1/\ln\mu$, which leads to a (negligible) logarithmic enhancement of the condensate between

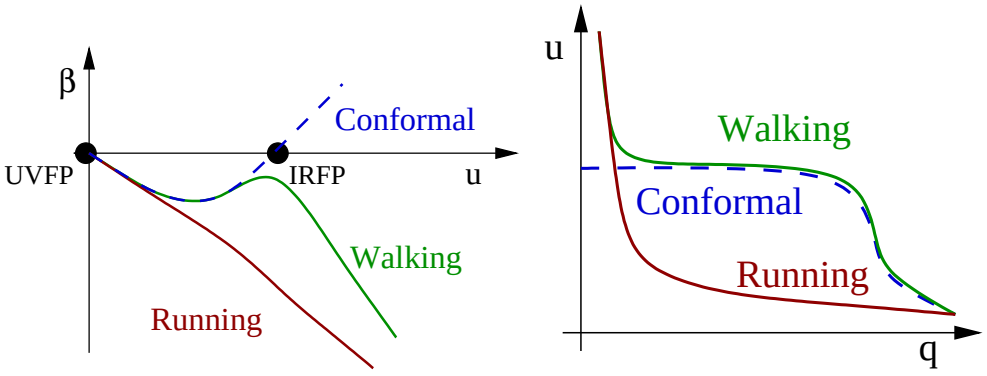

(a) Beta function (b) Coupling

Figure 1.3: Beta function and coupling for running, walking and conformal theories.

the two scales,

$$\langle \overline{Q}Q \rangle_{ETC} \sim \ln \left(\frac{\Lambda_{ETC}}{\Lambda_{TC}} \right) \langle \overline{Q}Q \rangle_{TC}. \tag{1.16}$$

By contrast in a walking theory the coupling, and hence the anomalous mass dimension, are almost constant between the TC and ETC scales, which leads to a power enhancement of the condensate,

$$\langle \overline{Q}Q \rangle_{ETC} \sim \left(\frac{\Lambda_{ETC}}{\Lambda_{TC}} \right)^{\gamma(g^{*2})} \langle \overline{Q}Q \rangle_{TC}, \tag{1.17}$$

where g^{*2} is the critical value of the coupling at the fixed point. For $\gamma(g^{*2}) \sim 1$ this gives an enhancement factor $\sim 10^3$, which would increase the quark mass upper bound of Eq. 1.14 to $m_q \lesssim 100\,\mathrm{GeV}$. Unfortunately, as can be seen from Eq. 1.12, such a large number of techi–fermions would cause an unacceptably large contribution to the S parameter, so this solution would also appear to be ruled out. However, the near–conformal dynamics will modify Eq. 1.12, and may reduce the size of the S parameter [21, 28, 29, 30]. Unlike the case of QCD–like dynamics, where all the contributions are positive, in this case there are also negative contributions. One estimate [28] gives

$$S_{walking} = (0.055a - 0.035b) n_f^{TC} N_{TC} - 0.015 n_f^{TC}. \tag{1.18}$$

where a and b are unknown $\mathcal{O}(1)$ constants, and may be such that $S_{walking} \simeq 0$.

While it is possible that this cancellation occurs, a more recent proposal is to use gauge theories with fermions in higher representations of the gauge group [31]. These theories can be close to the conformal window with a small number of fermions [32], as shown by the perturbative estimates of the conformal window for various representations in Fig. 1.4, and so will have a much smaller S parameter.

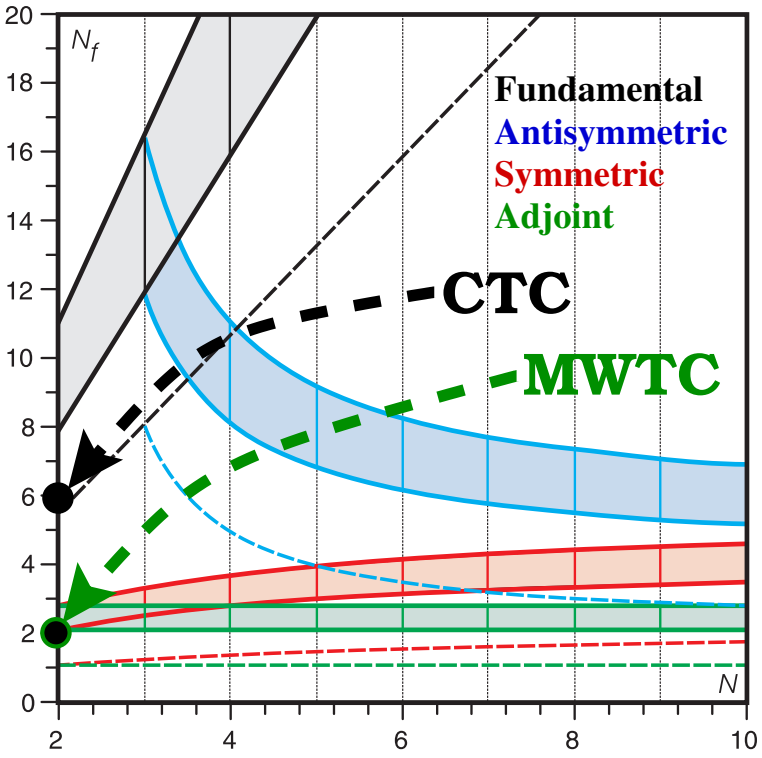

Figure 1.4: Phase diagram showing the perturbative estimate of the conformal window for SU(N) gauge theories containing N_f fermions in various representations. Based on the figure in Ref. [32]. For $N_f = 0$ all the theories are confining. As N_f is increased, the second term of the β–function changes sign (the dashed line), indicating the existence of a Banks–Zaks fixed point. At the bottom of the shaded region chiral symmetry–breaking is lost, and at the top of the shaded region asymptotic freedom is lost. In this perturbative picture conformal theories lie in the shaded regions, and walking theories just below these regions.

The two specific models investigated in this thesis are described in more detail in Sec. 1.4. For a recent review of these and other Technicolor models see Refs. [33, 34, 35], and for a recent review of the ongoing lattice investigations of these theories see Refs. [36, 37].

1.3 Scheme Dependence

The Callan–Symanzik equations describe the change of parameters in the Lagrangian of the theory as a function of the cut–off. The evolution of the coupling, for example, is described in a massless renormalisation scheme by the β function

$$\beta(g) = \frac{dg}{d\ln|\mu|}. \tag{1.19}$$

A zero of this function corresponds to an ultraviolet fixed point (UVFP) if the slope of $\beta(g)$ is negative, or an infrared fixed point (IRFP) if the slope is positive. The existence of a fixed point is universal among mass–independent schemes[1], as is the critical exponent at the fixed point,

$$y_g = -\left.\frac{d\beta(g)}{dg}\right|_{g=g^*}, \tag{1.20}$$

the slope of the β function at the fixed point. In fact y_g determines the rate at which any perturbative coupling approaches the fixed point [39]. While the rate of approach to the fixed point is scheme–independent, the value of the coupling at the fixed point, g^*, is scheme–dependent.

For small values of the coupling the β function can be expanded in powers of the coupling,

$$\beta(g) = \frac{dg}{d\ln|\mu|} = -\beta_0 g^3 - \beta_1 g^5 + \mathcal{O}(g^7), \tag{1.21}$$

where the first two terms β_0, β_1 are scheme–independent [40]. This expansion has been calculated in the $\overline{\text{MS}}$ scheme to 4–loop order [41].

"Walking" theories are typically said to have "small" β functions, such that the coupling runs slowly, as in Fig 1.3. This is a scheme–dependent statement, since a coupling which has a small β function in one scheme may appear to be running in another scheme.

The running of the mass in a massless renormalisation scheme [42] is described by the equation

$$\gamma(g) = -\frac{d\ln m}{d\ln\mu}, \tag{1.22}$$

where γ is the anomalous mass dimension, and at a fixed point where $\beta(g^*) = 0$,

[1] Assuming the transformations relating different schemes are non–singular [38]. See also Appendix A.

$\gamma(g^*)$ is a scheme independent quantity.

For small values of the coupling this function can also be expanded in powers of the coupling,

$$\gamma(g) = -\frac{d\ln m}{d\ln \mu} = d_0 g^2 + \mathcal{O}(g^4), \tag{1.23}$$

where the first term d_0 is scheme–independent [43]. This expansion has also been calculated in the $\overline{\text{MS}}$ scheme to 4–loop order [44]. See Appendix A for further details of the scheme dependence of these quantities.

The key point of all this is that the only physical, scheme independent quantities we can measure are

- the existence of a fixed point g^{*2} in the coupling,
- the slope of the β function at that fixed point, y_g,
- the size of the anomalous mass dimension at that fixed point, γ.

1.4 Specific Models

1.4.1 Minimal Walking Technicolor

Minimal Walking Technicolor (MWT) [31, 45, 46] is an SU(2) gauge theory with two adjoint Dirac fermions. The combination of a small number of flavours and colors along with near–conformal behaviour means the S parameter is expected to be small [47], and that realistic quark masses can be generated while supressing FCNC interactions.

The left handed techni–quarks are doublets of the $\text{SU}(2)_L$ weak interaction, and the right handed techni–quarks are singlets,

$$Q_L^a = \begin{pmatrix} U^a \\ D^a \end{pmatrix}_L, \quad Q_R^a = (U_R^a), (D_R^a), \quad a = 1, 2, 3. \tag{1.24}$$

In general, an SU(2) gauge theory with an odd number of left–handed fermion doublets suffers from the Witten topological anomaly [48]. To solve this problem the model also contains a weakly charged fermionic doublet which is a technicolor singlet [49],

$$L_L = \begin{pmatrix} N \\ E \end{pmatrix}_L, \quad L_R = (N_R, E_R). \tag{1.25}$$

The action has a global SU(4) flavour symmetry, which when broken to the maximal diagonal subgroup O(4), leads to nine Goldstone bosons. Three of these are absorbed as longitudinal degrees of freedom by the weak gauge bosons, and the remaining six will receive masses from ETC interactions.

The first two terms in the beta function, which are scheme independent, are of opposite sign and hence predict a fixed point,

$$g^{*2} = -\frac{\beta_0}{\beta_1} = \frac{4\pi^2}{5} \simeq 7.9, \tag{1.26}$$

with a corresponding anomalous mass dimension

$$\gamma = d_0 g^{*2} = \frac{3g^{*2}}{4\pi^2} = 0.6, \tag{1.27}$$

and a coupling critical exponent

$$y_g = \frac{5\beta_0^2}{\beta_1} = -0.1. \tag{1.28}$$

This is at relatively strong coupling, where it is not clear that perturbation theory is valid. In the $\overline{\text{MS}}$ scheme these perturbative expansions have been worked out to 4 loops [41, 44], and predict the following:

order	g^{*2}	γ	y_g
$2-\text{loop}$	7.90	0.820	-0.1000
$3-\text{loop}$	5.77	0.543	-0.0927
$4-\text{loop}$	5.66	0.500	-0.0937

(1.29)

The stability of γ and y_g as the number of loops is increased suggests that perturbation theory may be reliable in this region. The anomalous mass dimension at the fixed point can also be computed analytically using the conjectured all–order beta function [50], which predicts[2]

$$\gamma = \frac{11C_2(A) - 4T_R n_f^{TC}}{2n_f^{TC} T_R \left(1 + \frac{7}{11}\frac{C_2(A)}{C_2(R)}\right)} = \frac{11}{24} \simeq 0.458, \tag{1.30}$$

[2]This prediction supersedes the original all–order conjecture [51] of $\gamma = [11C_2(A) - 4T_R n_f^{TC}]/[2n_f^{TC} T_R] = 0.75$ for this model.

where expressions for the group invariants are given in Table E.1. This value is consistent with the perturbative predictions [52].

This model has been the subject of many lattice spectrum studies in recent years [53, 40, 54, 55, 56, 57, 58, 59, 60, 61, 62], as well as several Schrödinger Functional studies [63, 64], in addition to the results presented in Sec. 3.2. and Chapter 4 of this thesis.

1.4.2 Minimal Conformal Technicolor

Minimal Conformal Technicolor (MCT) [65, 66] is an SU(2) gauge theory with $(2+n)$ fundamental Dirac fermions, where n is large enough that the theory has a fixed point. It contains the following fermions which transform under $\mathrm{SU}(2)_{\mathrm{CTC}} \otimes \mathrm{SU}(2)_{\mathrm{W}} \otimes \mathrm{U}(1)_{\mathrm{Y}}$ as

$$\begin{aligned} \psi &\sim (2,2)_0, \\ \widetilde{\psi}_1 &\sim (2,1)_{-\frac{1}{2}}, \\ \widetilde{\psi}_2 &\sim (2,1)_{+\frac{1}{2}}, \\ \chi &\sim (2,1)_0 \times n. \end{aligned} \tag{1.31}$$

The conformal symmetry is softly broken by technifermion mass terms,

$$\Delta\mathcal{L} = -\kappa\psi\psi - \widetilde{\kappa}\widetilde{\psi}_1\widetilde{\psi}_2 - K\chi\chi + \text{h.c.}, \tag{1.32}$$

where it is assumed that $K \gg \kappa, \widetilde{\kappa}$. This means that at the TC scale the n χ fermions can be integrated out, leaving an effective asymptotically free SU(2) gauge theory with 2 fundamental Dirac fermions. These fermions have an approximate SU(4) symmetry, which when broken to Sp(4) leads to 5 Goldstone bosons. Three of these are absorbed as longitudinal degrees of freedom by the weak gauge bosons, and the remaining two are a composite Higgs scalar h and a pseudoscalar A.

We consider the case of the SU(2) gauge theory with six fundamental fermions. The first two terms in the beta function, which are scheme independent, are of opposite sign and hence predict a fixed point,

$$g^{*2} = -\frac{\beta_0}{\beta_1} = \frac{160\pi^2}{11} \simeq 143.6. \tag{1.33}$$

This is clearly at strong coupling where perturbation theory is not reliable, and so this needs to be investigated non–perturbatively. The conjectured all–order beta function predicts[3] $\gamma = 55/89 \simeq 0.618$.

While SU(3) gauge theories with many fundamental fermions have been the subject of many recent lattice studies [67, 68, 69, 70, 71, 72, 73, 74, 75, 76, 77, 78, 79, 80, 81, 82, 83], the results presented in Sec. 3.3 are the first for an SU(2) gauge theory with many fundamental fermions.

1.5 Summary

Technicolor theories with QCD–like dynamics have been ruled out by experiment, but recent "walking" incarnations provide promising dynamical theories of electroweak symmetry breaking. Whether or not they are actually phenomenologically viable depends on their strong dynamics, which are not perturbatively accessible. Of particular importance is the existence of an IRFP at strong coupling in these theories, and the size of the anomalous mass dimension at this fixed point.

The goal of the work described in this thesis is to obtain non–perturbative measurements of these scheme independent quantities in two candidate walking Technicolor theories: Minimal Walking Technicolor - two Dirac fermions in the adjoint representation of SU(2), and Conformal Technicolor - six Dirac fermions in the fundamental representation of SU(2).

[3]This prediction supersedes the original all–order conjecture of $\gamma = [11C_2(A) - 4T_R n_f^{TC}]/[2n_f^{TC}T_R] = 5/3$ for this model.

Chapter 2

Higher Representations on the Lattice

2.1 Continuum QCD

2.1.1 Introduction

The QCD Lagrangian in four–dimensional Euclidean space is given by [84]

$$\mathcal{L}_{QCD} = \overline{\psi}_i \left(\gamma^\mu [\partial_\mu - igA_\mu(x)] + m_i\right) \psi_i - \tfrac{1}{4} F_{\mu\nu} F^{\mu\nu}, \tag{2.1}$$

where the gamma matrices are defined in Eq E.2, ψ_i is a fermion field with mass m_i and A_μ is the gluon field which can be written

$$A_\mu = T^a A^a_\mu(x). \tag{2.2}$$

$F_{\mu\nu}$ is the field strength tensor which can be similarly decomposed as

$$F_{\mu\nu} = T^a F^a_{\mu\nu}(x), \tag{2.3}$$

where

$$F^a_{\mu\nu} = \partial_\mu A^a_\nu(x) - \partial_\nu A^a_\mu(x) + g f_{abc} A^b_\mu A^c_\nu, \tag{2.4}$$

and T^a are the generators of the color gauge group and f_{abc} are the structure constants.

This Lagrangian is invariant under a number of symmetries, in particular it

is locally gauge–invariant, and chirally invariant in the massless limit.

2.1.2 Gauge Symmetry

The Lagrangian is invariant under a local gauge transformation,

$$\begin{array}{lcl} \psi & \rightarrow & G(x)\psi, \\ \overline{\psi} & \rightarrow & \overline{\psi}G^{-1}(x), \\ A_\mu & \rightarrow & G(x)A_\mu G^{-1}(x) - \frac{i}{g}\left(\partial_\mu G(x)\right)G^{-1}(x), \\ F_{\mu\nu} & \rightarrow & G(x)F_{\mu\nu}G^{-1}(x), \end{array} \tag{2.5}$$

where

$$G(x) = e^{iw^a(x)T^a}, \tag{2.6}$$

is an element of the color gauge group.

2.1.3 Chiral Symmetry

In a quantum theory, symmetries are encoded in Ward identities. In the massless limit $m \rightarrow 0$ the lagrangian is invariant under an infinitesimal chiral transformation [85],

$$\begin{array}{lcl} \psi & \rightarrow & \psi + iw^a(x)T^a\gamma_5\psi, \\ \overline{\psi} & \rightarrow & \overline{\psi} + iw^a(x)\overline{\psi}T^a\gamma_5, \end{array} \tag{2.7}$$

where it is assumed there are N mass-degenerate quarks forming an SU(N) multiplet with generators T^a.

Such a change of integration variables does not change the value of a physical observable,

$$\langle\mathcal{O}\rangle = \int d\psi(x)d\overline{\psi}(x)\mathcal{O}e^{-S} = \int \mathcal{J}d\psi(x)d\overline{\psi}(x)(\mathcal{O}+\delta\mathcal{O})e^{-(S+\delta S)}, \tag{2.8}$$

and since the matrices T^a are traceless the measure is invariant, $\mathcal{J} = 1$, so expanding to first order this gives the Ward identity

$$\langle\delta\mathcal{O}\rangle = \langle\mathcal{O}\delta S\rangle. \tag{2.9}$$

The variation in the action is then

$$\begin{aligned}\delta S &= \int d^4x \left[\overline{\psi} w^a(x)\gamma_5 T^a(\gamma^\mu\partial_\mu + m)\psi + \overline{\psi}(\gamma^\mu\partial_\mu + m)w^a(x)T^a\gamma_5\psi\right] \\ &= \int d^4x \left[2mw^a(x)\overline{\psi}\gamma_5 T^a\psi + \overline{\psi}T^a\{\gamma_5,\gamma^\mu\}\partial_\mu\psi + (\partial_\mu w^a(x))\overline{\psi}\gamma^\mu T^a\gamma_5\psi\right]\end{aligned} \tag{2.10}$$

The second term is zero since $\{\gamma_5, \gamma_\mu\} = 0$, and the third term can be rewritten by integration by parts (assuming $w^a(x)$ smoothly goes to zero at the boundary), to give

$$\delta S = \int d^4x w^a(x)\left(-\partial_\mu A^{\mu a}(x) + 2mP^a(x)\right), \tag{2.11}$$

where the isovector axial current A^a_μ and density P^a are given by

$$A^a_\mu(x) = \overline{\psi}(x)\gamma_\mu\gamma_5 T^a\psi(x), \quad P^a = \overline{\psi}(x)\gamma_5 T^a\psi(x). \tag{2.12}$$

Inserting this expression into Eq 2.9, and assuming that $\mathcal{O}$ lies outside the domain of integration so that $\langle\delta\mathcal{O}\rangle = 0$, gives the PCAC equation (Partially Conserved Axial Current),

$$\langle\partial_\mu A^{\mu a}(x)\mathcal{O}\rangle = 2m\langle P^a(x)\mathcal{O}\rangle, \tag{2.13}$$

showing that the axial current is conserved in the massless limit. The conservation of this axial current, as well as other similar Ward identities, show that the quantised theory is chirally invariant in the $m \to 0$ limit.

2.2 Lattice QCD

2.2.1 Introduction

To simulate the QCD Lagrangian on a computer, a discretised version of Eq 2.1 is required, defined on a lattice with $L_x \times L_y \times L_z \times L_t$ points and a lattice spacing a. There is considerable freedom in how to do this, but any discretisation must reduce to the original theory in the $a \to 0$ continuum limit, be gauge–invariant, and be chirally symmetric in the massless limit.

2.2.2 Gauge Action

Gauge links $U_{x,\mu}$ are defined on the links between every site x and $x+\hat{\mu}$. They are related to the vector potential A_μ through

$$U_{x,\mu} = e^{igaA^b_\mu T^b}, \tag{2.14}$$

and under a gauge transformation they transform as

$$U_{x,\mu} \to G(x)U_{x,\mu}G^{-1}(x+\hat{\mu}). \tag{2.15}$$

The gauge part of the action can be constructed from a closed loop of these links, the simplest example being the Wilson gauge action

$$S_g = \beta \sum_{\mu<\nu} \left(1 - \tfrac{1}{N}\Re tr\mathcal{P}_{\mu\nu}\right), \tag{2.16}$$

where $\beta = 2N/g^2$, and

$$\mathcal{P}_{\mu\nu} = U_{x,\mu}U_{x+\hat{\mu},\nu}U^\dagger_{x+\hat{\nu},\mu}U^\dagger_{x,\nu}. \tag{2.17}$$

2.2.3 Naive Fermions

The 'naive' discretisation procedure for the fermionic part of the action is to replace the covariant derivative with a symmetrised difference,

$$[\partial_\mu - igA_\mu(x)]\psi_x \to \frac{1}{2a}\left(U_{x,\mu}\psi_{x+\hat{\mu}} - U^\dagger_{x-\hat{\mu},\mu}\psi_{x-\hat{\mu}}\right), \tag{2.18}$$

which preserves the anti–hermicity of the differential operator. This leads to a discrete action

$$S_f^{naive} = a^4 \sum_n \overline{\psi}_n \left(\frac{1}{2a}\sum_{\mu=0}^{3}\gamma^\mu\left(U_{n,\mu}\psi_{n+\hat{\mu}} - U^\dagger_{n-\hat{\mu},\mu}\psi_{n-\hat{\mu}}\right) + m\psi_n\right) \tag{2.19}$$

where n is an index running over all lattice sites with periodic boundary conditions. Unfortunately this discretisation produces a doubling of species from the discretisation in each dimension [86], as can be seen by considering the above

Dirac operator in momentum space for massless free fermions (so that $\psi \propto e^{-ip.x}$),

$$D(p) = \frac{1}{2a}\sum_{\mu}\gamma^{\mu}(e^{ip_{\mu}a} - e^{-ip_{\mu}a}) = \frac{1}{a}\sum_{\mu}\gamma^{\mu}\sin(p_{\mu}a). \tag{2.20}$$

In lattice units of $a = 1$ this has 16 zeros in the first Brillouin zone for $p_{\mu} = (p_1, p_2, p_3, p_4)$, where $p_i = 0, \pi$. The means that the fermion propagator formed by inverting this operator has 16 poles, corresponding to 16 fermions instead of the 1 expected in the continuum limit.

2.2.4 Wilson Fermions

One solution to this is to add a Wilson mass term to the lagrangian [87],

$$m\sum_{n}\overline{\psi}_n\psi_n \rightarrow m\sum_{n}\overline{\psi}_n\psi_n + \frac{ar}{2}\sum_{n,\mu}\partial_{\mu}\overline{\psi}_n\partial_{\mu}\psi_n, \tag{2.21}$$

which effectively gives the doubler fermions a mass proportional to $1/a$, so that their mass will be of the order of the cut-off and decouple from the low energy physics. The Wilson term itself tends to zero in the continuum limit, so that the original Lagrangian is recovered. The constant r can take various values, the simplest being $r = 1$. This leads to the Wilson-Dirac action

$$S_f = a^4\sum_{n}\overline{\psi}_n\left(\tfrac{-1}{2a}\sum_{\mu=0}^{3}\left\{(1-\gamma_{\mu})U_{x,\mu}\psi_{x+\mu} + (1+\gamma_{\mu})U^{\dagger}_{x-\mu,\mu}\psi_{x-\mu}\right\} + (\tfrac{4}{a}+m)\overline{\psi}_x\right), \tag{2.22}$$

which contains a Wilson momentum–dependent mass term that vanishes at the zero of the Brillouin zone. Considering the ward identity of Eq 2.9 under the chiral transformation of Eq 2.7, the change in the action is given by [88]

$$\delta S = \nabla^{\mu}_x A^a_{\mu}(x) - \overline{\psi}(x)\{T^a, m\}\gamma_5\psi(x) + X^a(x), \tag{2.23}$$

where $X^a(x)$ is the chiral variation of the Wilson term

$$\begin{aligned} X^a(x) = -\tfrac{r}{2a}\textstyle\sum_{\mu} \quad & \Big[\overline{\psi}_x T^a\gamma_5 U_{\mu,x}\psi_{x+\hat{\mu}} + \overline{\psi}_{x+\hat{\mu}}T^a\gamma_5 U^{\dagger}_{\mu,x}\psi_{x+\hat{\mu}} \\ & + \overline{\psi}_{x-\hat{\mu}}T^a\gamma_5 U_{\mu,x-\hat{\mu}}\psi_x + \overline{\psi}_x T^a\gamma_5 U^{\dagger}_{\mu,x-\hat{\mu}}\psi_x - 4\overline{\psi}_x T^a\gamma_5\psi_x\Big] \end{aligned} \tag{2.24}$$

and the isovector axial current A^a_μ is given by

$$A^a_\mu(x) = \frac{1}{2}\left[\overline{\psi}(x+\hat{\mu})\gamma_\mu\gamma_5 T^a U_\mu(x)\psi(x) + \text{h.c.}\right]. \tag{2.25}$$

At tree level $X^a(x)$ vanishes for vanishing lattice spacing, since $U \to e^0 = 1$ in the limit $a \to 0$, but ultraviolet divergences of the loop integrals also need to be considered. A multiplicatively renormalizable operator $\overline{X}^a(x)$ is defined by removing lower dimensional operators from $X^a(x)$,

$$\overline{X}^a = X^a + \overline{\psi}\{T^a, \overline{m}\gamma_5\}\psi + (Z_A - 1)\partial^\mu A^a_\mu \tag{2.26}$$

where Z_A and $\overline{m}$ are completely defined by the additional requirement

$$\langle \overline{X}^a(x)\psi(x_1)\overline{\psi}(x_2)\rangle \to 0 \tag{2.27}$$

in the $a \to 0$ continuum limit. Rewriting the Ward identity in terms of this operator and taking the continuum limit (so that $\langle \overline{X}^a(x)\rangle \to 0$) gives

$$Z_A\langle \partial_\mu A^a_\mu\rangle = \langle \overline{\psi}\{T^a, m - \overline{m}\}\gamma_5\psi\rangle \tag{2.28}$$

This is the PCAC in the continuum limit for Wilson fermions. The matrix elements of A^a_μ can be shown to satisfy the normalisation condition $\langle Z_A A^a_\mu\rangle = Z_A\langle A^a_\mu\rangle$, so that the Axial Current is conserved for a critical bare mass

$$m = m_{cr} \equiv \overline{m}(m_{cr}, r, g_0). \tag{2.29}$$

We can now write a discretised version of the QCD lagrangian as

$$S = S_g + S_f \tag{2.30}$$

where S_g is the Wilson gauge action defined in Eq 2.16, and S_f is the Wilson-Dirac fermion action defined in Eq 2.22. This action is gauge invariant, has the correct continuum limit, and is chirally symmetric in the massless limit as long as the bare quark mass is appropriately tuned to compensate for the additive quark mass renormalization [89].

2.3 Higher Representations on the Lattice

2.3.1 Introduction

To simulate gauge theories with fermions in higher representations of the gauge group some changes are required. The Wilson gauge action is unchanged, Eq 2.16 can still be used with the link variables in the fundamental representation of the gauge group, exactly the same as for QCD. The fermionic part of the action needs to be changed however.

2.3.2 Generic Representation Wilson Fermions

The action for fermions in some representation R of the gauge group can be written

$$S^R = S_g + a^4 \sum_x \overline{\psi}_x D_m \overline{\psi}_x, \tag{2.31}$$

where S_g is the Wilson gauge action of Eq 2.16, and

$$D_m \psi_x = (\tfrac{4}{a} + m_0)\psi_x - \tfrac{1}{2a} \sum_\mu \left\{ (1-\gamma_\mu) U^R_{x,\mu} \psi_{x+\mu} + (1+\gamma_\mu)(U^R_{x-\mu,\mu})^\dagger \psi_{x-\mu} \right\}. \tag{2.32}$$

If the chosen representation is the fundamental, then the gauge link variables are given by

$$U^F_{x,\mu} = e^{iw^a(x,\mu)T^a_F}, \tag{2.33}$$

where T^a_F are the generators of the fundamental representation, and the action is identical to Eq. 2.30.

If the fermions are in a higher representation then the gauge link variables are instead given by

$$U^R_{x,\mu} = e^{iw^a(x,\mu)T^a_R}, \tag{2.34}$$

where T^a_R are the generators of the higher representation, and the functions $w^a(x,\mu)$ are the same in both Eq 2.33 and Eq 2.34.

2.4 HiRep

HiRep [54] is an implementation of the RHMC algorithm [90] for gauge theories with any number of flavours and colours, and in a variety of representations of the gauge group.

It uses HMC molecular dynamics update algorithm to simulate the action of Eq 2.31, for fermions in the fundamental, adjoint, symmetric and anti–symmetric representation of the SU(N) gauge group for any N. In addition it uses the RHMC algorithm to efficiently simulate a range of different numbers of fermion flavours, and uses even–odd preconditioning to speed up the inversion of the Dirac operator.

Chapter 3

Schrödinger Functional Method

3.1 The Schrödinger Functional

To determine the critical coupling and the anomalous mass dimension, we need a scheme to measure the coupling and mass for a range of scales. The Schrödinger Functional (SF) [91, 92, 93, 94, 95] is a finite volume renormalisation scheme which allows us to do this. Space–time is defined as a L^4 cylinder with periodic spatial boundary conditions, and Dirichlet boundary conditions in time. The scale μ is inversely proportional to the size of the cylinder, $\mu \sim 1/L$, so the scale dependence of renormalised quantities can be determined by varying L.

The gauge fields are fixed on the timelike boundaries,

$$A_k(x)|_{x^0=0} = C_k, \quad A_k(x)|_{x^0=L} = C'_k, \tag{3.1}$$

where C_k, C'_k are classical gauge potentials which generate a gauge configuration B which is a minimum of the action. The partition function under these boundary conditions is the quantum mechanical transition amplitude from a state $|C\rangle$ to a state $|C'\rangle$ after a (Euclidean) time T.

Since this background field is a minimum of the action it dominates the path integral for weak coupling g_0, and the action has a perturbative expansion

$$\begin{array}{lcl} \Gamma[B] & = & \frac{1}{g_0^2}\Gamma_0[B] + \Gamma_1[B] + g_0^2\Gamma_2[B] + \ldots, \\ \Gamma_0[B] & \equiv & g_0^2 S[B]. \end{array} \tag{3.2}$$

The strength of the background gauge fields is parametrised by a single

dimensionless quantity η. The observable $\Gamma' = \left\langle \frac{\partial S}{\partial \eta} \right\rangle$ is used to define a renormalized coupling $\overline{g}^2(L)$, which is chosen to coincide with the bare coupling g_0^2 at weak coupling,

$$\overline{g}^2(L) = \Gamma'_0[B]/\Gamma'[B]. \tag{3.3}$$

3.1.1 Lattice Formulation

The SF can be formulated on a lattice with $\hat{L}^4$ points, with lattice spacing a, so that $L = \hat{L}a$. The spatial dimensions have the usual periodic boundary conditions but the time dimension is finite, with constant gauge fields on the boundaries.

A specific choice for the gauge group SU(2) is the abelian background field induced by the boundary values [96]

$$C_k = \frac{i}{L}\begin{pmatrix} -\eta & 0 \\ 0 & \eta \end{pmatrix}, \quad C'_k = \frac{i}{L}\begin{pmatrix} \eta - \pi & 0 \\ 0 & \pi - \eta \end{pmatrix}, \tag{3.4}$$

evaluated at $\eta = \pi/4$. From these the boundary spatial gauge fields can be formed,

$$U_{x,k}|_{x_0=0} = e^{aC_k}, \quad U_{x,k}|_{x_0=L-a} = e^{aC'_k}. \tag{3.5}$$

In addition boundary conditions are required for the fermions [94, 97],

$$\begin{aligned} P_+\psi|_{x_0=0} &= 0, \quad P_-\psi|_{x_0=L-a} = 0, \\ \overline{\psi}P_-|_{x_0=0} &= 0, \quad \overline{\psi}P_+|_{x_0=L-a} = 0, \end{aligned} \tag{3.6}$$

where $P_\pm = \frac{1}{2}(1 \pm \gamma_0)$.

Since the dirac operator is a first order differential equation only half the boundary terms need to be specified for a unique solution, and for consistency the complementary components of the boundary values not fixed by Eq. 3.6 must vanish [98]. The choice of vanishing fermionic boundary conditions in Eq. 3.6 ensures that apart from the renormalisation of the coupling and the quark mass, no additional renormalisation of the SF is necessary [99]. Outside of the manifold, i.e. sites with $x_0 < 0$ or $x_0 > L - a$, the fermions are set to zero, and the gauge links are set to the identity.

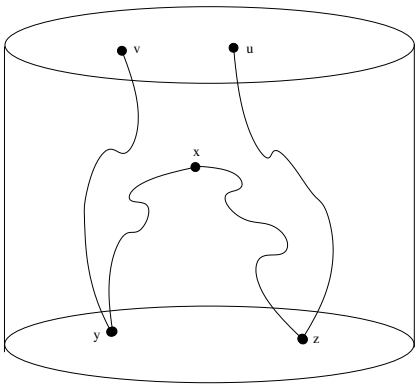

Figure 3.1: Boundary-to-boundary and boundary-to-bulk correlators used to measure the PCAC mass in the SF scheme.

3.1.2 Renormalised Coupling

The observable used to determine the running coupling defined in Eq. 3.3 is

$$\frac{\partial\Gamma}{\partial\eta} = \left\langle \frac{\mathrm{d}S}{\mathrm{d}\eta} \right\rangle = \left\langle \frac{\mathrm{d}S_{\mathrm{g}}}{\mathrm{d}\eta} \right\rangle + \left\langle \frac{\mathrm{d}S_{\mathrm{f}}^{\mathrm{eff}}}{\mathrm{d}\eta} \right\rangle , \tag{3.7}$$

where S is the Wilson action. The pure gauge part $\mathrm{d}S_{\mathrm{g}}/\mathrm{d}\eta$ is given by the colour 8 component of the electric field at the boundary [99],

$$\frac{\partial S_g}{\partial\eta} = -\frac{2a^3}{g_0^2 L}\sum_{\mathbf{x}} \{E_k(\mathbf{x}) - (E_k)'(\mathbf{x})\} , \tag{3.8}$$

where

$$E_k(\mathbf{x}) = \frac{1}{a^2}\mathrm{Re}\,\mathrm{tr}\left\{ i\lambda U_{x,k} U_{x+a\hat{k},0} U^{-1}_{x+a\hat{0},k} U^{-1}_{x,0} \right\}_{x_0=0} , \tag{3.9}$$

$$(E_k)'(\mathbf{x}) = -\frac{1}{a^2}\mathrm{Re}\,\mathrm{tr}\left\{ i\lambda U^{-1}_{x+a\hat{0},k} U^{-1}_{x,0} U_{x,k} U_{x+a\hat{k},0} \right\}_{x_0=L-a} , \tag{3.10}$$

and $\lambda = \mathrm{diag}(1,-1)$.

The fermionic part $\left\langle \frac{\mathrm{d}S_{\mathrm{f}}^{\mathrm{eff}}}{\mathrm{d}\eta} \right\rangle$ is zero for the Wilson action [100], so the renormalised coupling on the lattice is only a function of the gauge fields [98],

$$\overline{g}^2(L) = -24\frac{L^2}{a^2}\sin\left[\frac{a^2}{L^2}(\pi - 2\eta)\right] \Big/ \left\langle \frac{\partial S_g}{\partial\eta} \right\rangle . \tag{3.11}$$

3.1.3 PCAC Mass

Using the relation between the partially conserved axial current (PCAC) and the vector current we can define a PCAC mass in terms of correlators between the $x_0 = 0$ boundary and the bulk [101]

$$m_{pos}(x_0) = \frac{\frac{1}{2}(\partial_0 + \partial_0^*) f_A(x_0)}{2 f_P(x_0)} = \frac{f_A(x_0 + a\hat{0}) - f_A(x_0 - a\hat{0})}{4 f_P(x_0)} \tag{3.12}$$

where $x_0 \simeq T/2$, and

$$f_A(x_0) = \frac{a^6}{2} \sum_{y,z} \left\langle \mathrm{Tr} \left\{ \left[\zeta(z)\overline{\psi}(x)\right]_F \gamma_0\gamma_5 \left[\psi(x)\overline{\zeta}(y)\right]_F \gamma_5 \right\} \right\rangle_G \tag{3.13}$$

$$f_P(x_0) = \frac{a^6}{2} \sum_{y,z} \left\langle \mathrm{Tr} \left\{ \left[\zeta(z)\overline{\psi}(x)\right]_F \gamma_5 \left[\psi(x)\overline{\zeta}(y)\right]_F \gamma_5 \right\} \right\rangle_G \tag{3.14}$$

where the trace is over dirac and color indices [102].

A PCAC mass can also be defined using correlators between the $x_0 = T - a$ boundary and the bulk

$$m_{neg}(x_0) = \frac{\frac{1}{2}(\partial_0 + \partial_0^*) f'_A(x_0)}{2 f'_P(x_0)} = \frac{f'_A(x_0 + a\hat{0}) - f'_A(x_0 - a\hat{0})}{4 f'_P(x_0)} \tag{3.15}$$

where $x_0 \simeq T/2$, and

$$f'_A(x_0) = -\frac{a^6}{2} \sum_{y,z} \left\langle \mathrm{Tr} \left\{ \left[\zeta'(z)\overline{\psi}(x)\right]_F \gamma_0\gamma_5 \left[\psi(x)\overline{\zeta}'(y)\right]_F \gamma_5 \right\} \right\rangle_G \tag{3.16}$$

$$f'_P(x_0) = \frac{a^6}{2} \sum_{y,z} \left\langle \mathrm{Tr} \left\{ \left[\zeta'(z)\overline{\psi}(x)\right]_F \gamma_5 \left[\psi(x)\overline{\zeta}'(y)\right]_F \gamma_5 \right\} \right\rangle_G \tag{3.17}$$

The difference between the correlators is just a time reversal, but since the boundary gauge fields are in general different the correlators will not be identical. However, the two definitions of the PCAC mass should be equivalent up to $\mathcal{O}(a)$ effects - so the difference between the two values will give an indication of the size of these effects.

When measuring the running of the mass we choose to use unit boundary gauge fields, so in this case the boundary gauge fields are the same and so m_{pos} and m_{neg} can be averaged, improving the statistical accuracy of the measurement.

The Schrödinger Functional is defined at zero mass, but the physical quark mass is additively renormalized when using the Wilson action. This means that to simulate at the massless point, κ must be tuned to its critical value, κ_c, where the PCAC mass is zero. Note that this is the bare PCAC mass, the renormalised PCAC mass has an additional $\frac{Z_A}{Z_P}$ factor, but the bare PCAC mass is sufficient for finding κ_c.

3.1.4 Renormalised Mass

To investigate the running of the mass we need to measure the renormalized mass $\overline{m}(\mu)$

$$\overline{m}(\mu) = \frac{Z_A(g_0)}{Z_P(g_0, a\mu)} m(g_0) \tag{3.18}$$

The factor Z_A is scale independent and only depends on the bare coupling g_0 [103]. So the running depends only on the factor Z_P [104]

$$Z_P(g_0, a\mu) = \left. \frac{\sqrt{3f_1}}{f_P(L/2)} \right|_{\kappa=\kappa_c} \tag{3.19}$$

which is 1 at tree level, and where $f_P(L/2)$ is the correlator defined in Eq. 3.14 for m_{pos} and in Eq. 3.17 for m_{neg}. So the only additional observable required is the boundary to boundary correlator f_1 [95]

$$f_1 = \frac{a^{12}}{2L^6} \sum_{u,v,y,z} \left\langle \mathrm{Tr} \left\{ \left[\zeta(z) \overline{\zeta}'(u) \right]_F \gamma_5 \left[\zeta'(v) \overline{\zeta}(y) \right]_F \gamma_5 \right\} \right\rangle_G \tag{3.20}$$

Again when measuring the running of the mass we use unit boundary gauge fields so that Z_{Ppos} and Z_{Pneg} can be averaged.

3.1.5 Implementation

The Schrödinger Functional was implemented by modifying the HiRep code described in Sec. 2.4. Full details of the implementation are given in Appendix C, and the tests performed on the code to ensure it was working correctly are given in Appendix D.

3.2 Minimal Walking Technicolor Results

The Schrödinger Functional method was used to measure the running of the coupling and the mass in Minimal Walking Technicolor, the SU(2) gauge theory with two adjoint Dirac fermions described in Sec. 1.4.1. These results are published in Ref. [43].

3.2.1 Lattice parameters

We used the Wilson plaquette gauge action, together with adjoint Wilson fermions, and an RHMC algorithm with 2 pseudofermions. We performed two sets of simulations in order to determine the running coupling and Z_P. The parameters of the runs are summarised respectively in Tab. 3.1, and 3.2. Note that Z_P is determined from a different set of runs at similar values of β, L, κ. The values of κ_c are obtained from the PCAC relation as described in Section 3.1.3.

We measured the average plaquette for a range of values of β and κ, shown in Fig. 3.2. There is a clear jump in the plaquette for $\beta \lesssim 2.0$, implying the presence of a bulk transition. The lowest β we use for our measurements of $\overline{g}^2$ and Z_P is $\beta = 2.0$, so our results should not be affected by this transition.

3.2.2 Results for the coupling

We measured the coupling $\overline{g}^2(\beta, L)$ for a range of β, L. Our results are reported in Tab. 3.3, and plotted in Fig. 3.3: it is clear that the coupling is very similar for different L/a at a given value of β, and hence that it runs slowly.

In Fig. 3.4 we compare our results to those obtained in Ref. [63]. Our results are directly comparable since we use the same action and definition of the running coupling, and it is reassuring to see that they agree within statistical errors. The numbers reported in the figure have been obtained using completely independent codes; they constitute an important sanity check at these early stages of simulating theories beyond QCD.

The running of the coupling is encoded in the step scaling function $\sigma(u, s)$ as

$$\Sigma(u, s, a/L) = \overline{g}^2(g_0, sL/a)\big|_{\overline{g}^2(g_0, L/a)=u} , \tag{3.21}$$

$$\sigma(u, s) = \lim_{a/L \to 0} \Sigma(u, s, a/L) , \tag{3.22}$$

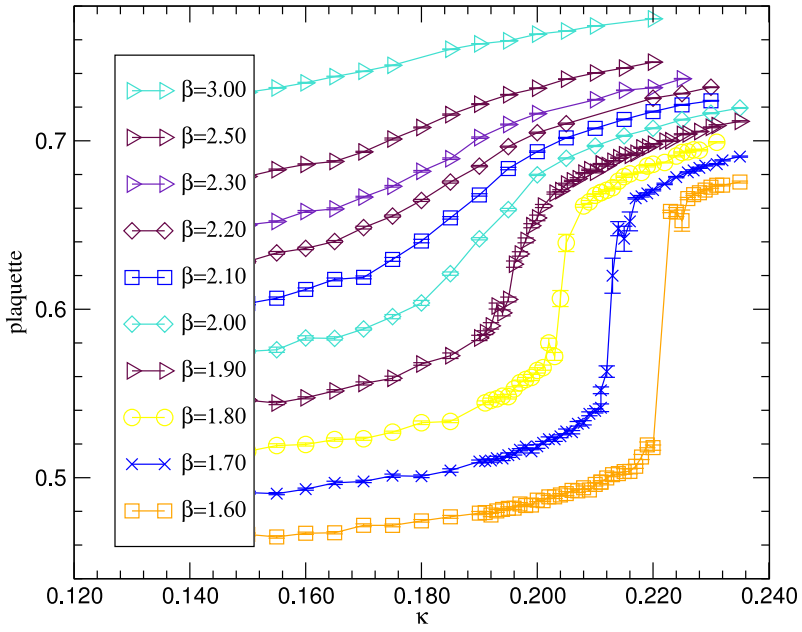

Figure 3.2: The average plaquette for a range of β and κ on 6^4 lattices. The bulk transition occurs around $\beta = 2.0$.

β	L=6	L=8	L=12	L=16
2.00	0.190834	-	-	-
2.10	0.186174	-	-	-
2.20	0.182120	0.181447	0.180500	-
2.25	0.180514	0.179679	-	-
2.30	0.178805	0.178045	-	-
2.40	0.175480	0.174887	-	-
2.50	0.172830	0.172305	0.171720	0.171720
2.60	0.170162	0.169756	-	-
2.70	0.167706	-	-	-
2.80	0.165932	0.165550	0.165050	-
3.00	0.162320	0.162020	0.161636	0.161636
3.25	0.158505	-	0.158000	-
3.50	0.155571	0.155361	0.155132	0.155132
3.75	0.152803	-	-	-
4.00	0.150822	0.150655	-	-
4.50	0.147250	0.147200	0.147120	0.147120
8.00	0.136500	0.136450	0.136415	-

Table 3.1: Values of β, L, κ used for the determination of $\overline{g}^2$. The entries in the table are the values of κ_c used for each combination of β and L.

β	L=6	L=8	L=12	L=16
2.00	0.190834	-	-	-
2.05	0.188504	-	0.186250	-
2.10	0.186174	-	-	-
2.20	0.182120	0.181447	0.180500	-
2.25	0.180514	0.179679	-	-
2.30	0.178805	0.178045	-	-
2.40	-	0.174887	-	-
2.50	0.172830	0.172305	0.171720	0.171720
2.60	0.170162	0.169756	-	-
2.70	0.167706	-	-	-
2.80	0.165932	0.165550	0.165050	-
3.00	0.162320	0.162020	0.161636	0.161636
3.25	0.158505	-	0.158000	-
3.50	0.155571	0.155361	0.155132	0.155132
3.75	0.152803	-	-	-
4.00	0.150822	0.150655	0.150510	-
4.50	0.147250	0.147200	0.147120	0.147120
8.00	0.136500	0.136450	0.136415	0.136415
16.0	0.130200	0.130200	0.130200	0.130375

Table 3.2: Values of β, L, κ used for the determination of Z_P. The entries in the table are the values of κ_c used for each combination of β and L.

as described in Ref. [93]. The function $\sigma(u, s)$ is the continuum extrapolation of $\Sigma(u, s, a/L)$, and is a discrete version of the β function. The relation between the two functions for a generic rescaling of lengths by a factor s is given by:

$$-2\log s = \int_u^{\sigma(u,s)} \frac{dx}{\sqrt{x}\beta(\sqrt{x})}\,. \tag{3.23}$$

It can be seen directly from the definition of $\sigma(u, s)$ in Eq. (3.22) that an IRFP corresponds to $\sigma(u, s) = u$, or in other words the condition that the coupling doesn't change when the scale is changed by a factor s.

Starting from the actual data, we interpolate quadratically in a/L to find values of $\overline{g}^2(\beta, L)$ at $L = 9, 10\frac{2}{3}$, so that we obtain data for four steps of size $s = 4/3$ for $L \to sL$: $L = 6, 8, 9, 12$; $sL = 8, 10\frac{2}{3}, 12, 16$. Then for each L we perform an interpolation in β using the same functional form as Ref. [80]:

$$\frac{1}{\overline{g}^2(\beta, L/a)} = \frac{\beta}{2N}\left[\sum_{i=0}^{n} c_i \left(\frac{2N}{\beta}\right)^i\right] \tag{3.24}$$

We choose to truncate the series with the number of parameters that minimises

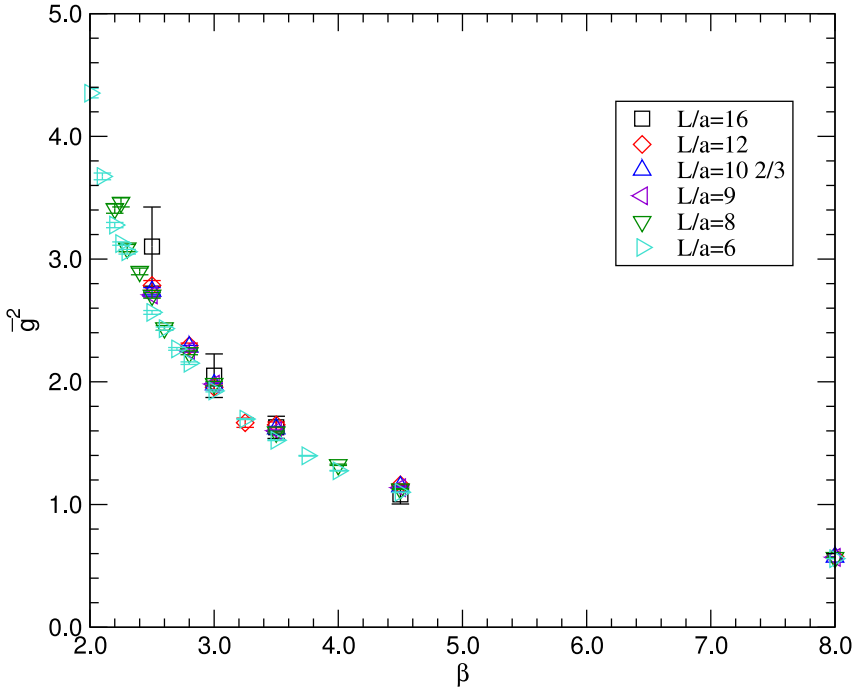

Figure 3.3: Data for the running coupling as computed from lattice simulations of the Schrödinger functional. Numerical simulations are performed at several values of the bare coupling β, and for several lattice resolutions L/a. The points at $L/a = 9, 10\frac{2}{3}$ are interpolated.

β	L=6	L=8	L=12	L=16
2.00	4.237(58)	-	-	-
2.10	3.682(39)	-	-	-
2.20	3.262(31)	3.457(59)	-	-
2.25	3.125(19)	3.394(54)	-	-
2.30	3.000(25)	3.090(46)	-	-
2.40	2.813(21)	2.887(44)	-	-
2.50	2.590(20)	2.682(35)	2.751(68)	3.201(324)
2.60	2.428(16)	2.460(29)	-	-
2.70	2.268(14)	-	-	-
2.80	2.141(12)	2.218(22)	2.309(40)	-
3.00	1.922(10)	1.975(25)	1.958(32)	2.025(157)
3.25	1.694(5)	-	1.830(90)	-
3.50	1.522(4)	1.585(11)	1.626(30)	1.603(76)
3.75	1.397(3)	-	-	-
4.00	1.275(3)	1.320(7)	-	-
4.50	1.101(3)	1.128(5)	1.152(10)	1.106(64)
8.00	0.558(1)	0.567(2)	0.574(3)	-

Table 3.3: Measured values of $\overline{g}^2$ on different volumes as a function of the bare coupling β.

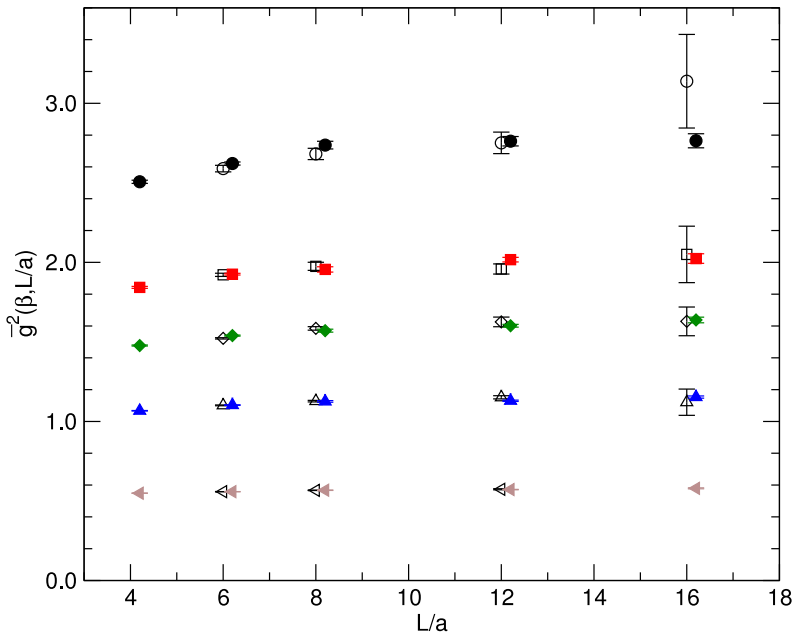

Figure 3.4: The results of our numerical simulations are compared to recent results obtained in Ref. [63]. Different symbols correspond to different values of the lattice bare coupling β, corresponding respectively to $\beta = 2.5, 3.0, 3.5, 4.5, 8.0$. Empty symbols correspond to the data obtained in this work. Full symbols correspond to the data in Ref. [63]. Symbols have been shifted horizontally for easier reading of the plot.

the χ^2 per degree of freedom.

All the subsequent analysis is based on these interpolating functions, and does not make further use of the original data. Using the fitted function in Eq. (3.24), we compute $\Sigma(u, 4/3, a/L)$ at a number of points in the range $u \in [0.5, 3.5]$. A continuum extrapolation is then performed in a/L using these points to give a single estimate of $\sigma(u) \equiv \sigma(u, 4/3)$. Example extrapolations for three values of u are shown in Fig. 3.5. The $L = 6$ data were found to have large $O(a)$ artifacts, and are not used in the continuum extrapolation. The $L = 16$ data have a large statistical error, which limits their current impact on the continuum extrapolation. The sources of systematic uncertainty in our final results for $\sigma(u)$ are due to the interpolation in L and β and to the extrapolation to the continuum limit. Full details of the statistical and systematic error analysis are provided in Appendix B.1.

The resulting values for $\sigma(u)$ with statistical errors only can be seen as the black circles in Fig. 3.6. The red error bars in Fig. 3.6 also include systematic errors, but using only a constant continuum extrapolation. This is equivalent to the assumption that lattice artefacts are negligible in our data. A similar assumption has been used in Ref. [63], where the data at finite a/L were used directly to constrain the parameters that appear in the β function of the theory.

Our current values for the step scaling function are consistent with a fixed point in the region $\overline{g}^2 \sim 2.0 - 3.2$, as reported in Ref. [63]. Further simulation at higher $\overline{g}^2$ is limited by the bulk transition at $\beta \simeq 2.0$, shown in Fig. 3.2, and observed in Refs. [55, 57].

The errors from also including the linear continuum extrapolation are much larger and mask any evidence for a fixed point, as shown in Fig. 3.7. This should be a conservative estimate of the total uncertainty on $\sigma(u)$, which is dominated by systematic errors.

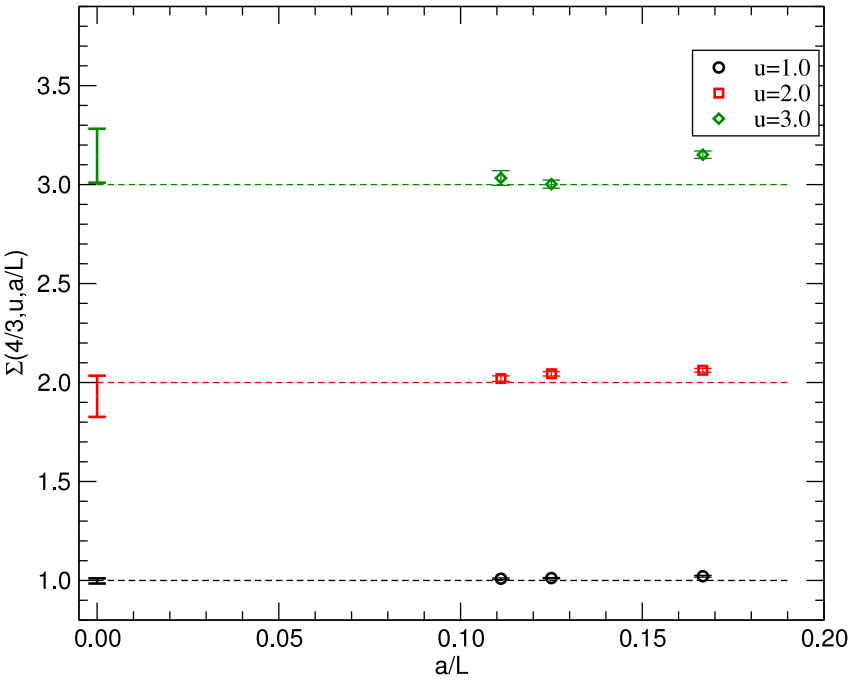

Figure 3.5: Results for the lattice step–scaling function $\Sigma(4/3, u, a/L)$. The dashed lines represent the initial value of u. The point at $x = 0$ yields the value of $\sigma(u)$, *i.e.* the extrapolation of Σ to the continuum limit. The error bar shows the difference between constant and linear extrapolation functions, and gives an estimate of the systematic error in the extrapolation as discussed in the text.

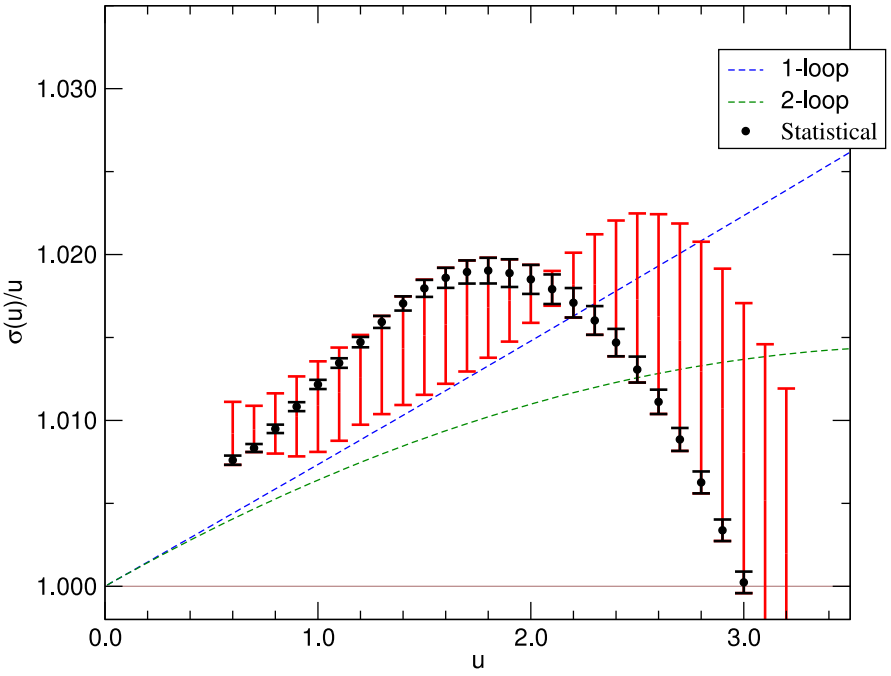

Figure 3.6: The relative step–scaling function $\sigma(u)/u$ obtained after extrapolating the lattice data to the continuum limit. The black circles have a statistical error only. The red error bars also include systematic errors, but using only a constant continuum extrapolation (i.e. ignoring lattice artifacts). Note that a fixed point is identified by the condition $\sigma(u)/u = 1$.

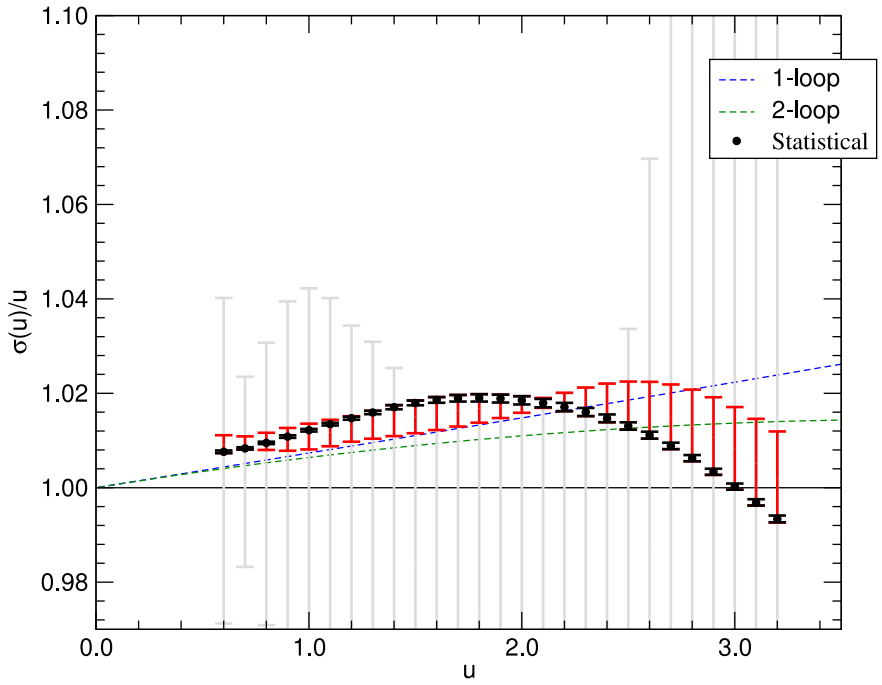

Figure 3.7: The relative step–scaling function $\sigma(u)/u$ obtained after extrapolating the lattice data to the continuum limit. The black circles have a statistical error only, the red error bars include systematic errors but using only a constant continuum extrapolation, and the grey error bars give an idea of the total error by including both constant and linear continuum extrapolations.

3.2.3 Running mass

The running of the fermion mass is determined by the scale–dependence of the renormalisation constant for the pseudoscalar fermion bilinear Z_P defined in Eq. (3.19). Note that Z_P is both scheme and scale dependent. The same step scaling technique described for the gauge coupling can be used to follow the nonperturbative evolution of the fermion mass in the SF scheme. In this work, we follow closely the procedure outlined in Ref. [101].

We have measured the pseudoscalar density renormalisation constant $Z_P(\beta, L)$ for a range of β, L. Our results are reported in Tab. 3.4, and plotted in Fig. 3.8, where we see that there is a clear trend in Z_P as a function of L at all values of β.

The lattice step scaling function for the mass is defined as:

$$\Sigma_P(u, s, a/L) = \left.\frac{Z_P(g_0, sL/a)}{Z_P(g_0, L/a)}\right|_{\overline{g}^2(L)=u} ; \tag{3.25}$$

the mass step scaling function in the continuum limit, $\sigma_P(u, s)$, is given by:

$$\sigma_P(u, s) = \lim_{a\to 0} \Sigma_P(u, s, a/L)\,. \tag{3.26}$$

The method for calculating $\sigma_P(u) \equiv \sigma_P(u, 4/3)$ is similar to that outlined in Sec. 3.2.2 for calculating $\sigma(u)$. We interpolate in β using a function of the form:

$$Z_P(\beta, L/a) = \sum_{i=0}^{n} c_i \left(\frac{1}{\beta}\right)^i \tag{3.27}$$

Full details of the procedure are given in Appendix B.2. Again the errors are dominated by systematics, in particular the choice of continuum extrapolation function. In Fig. 3.9 we see that, unlike $\overline{g}^2$, Z_P has a significant variation with a/L that is fit well by a linear continuum extrapolation. The constant extrapolation is only used to quantify the errors in extrapolation.

The mass step scaling function is related to the mass anomalous dimension (see e.g. Ref. [101]):

$$\sigma_P(u) = \left(\frac{u}{\sigma(u)}\right)^{(d_0/(2\beta_0))} \exp\left[\int_{\sqrt{u}}^{\sqrt{\sigma(u)}} dx \left(\frac{\gamma(x)}{\beta(x)} - \frac{d_0}{\beta_0 x}\right)\right] . \tag{3.28}$$

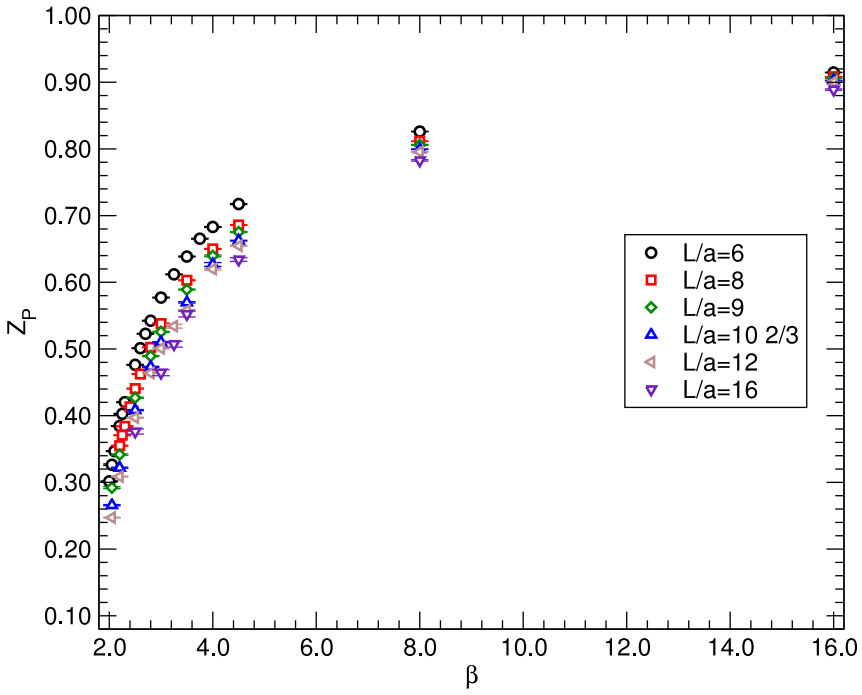

Figure 3.8: Data for the renormalisation constant Z_P as computed from lattice simulations of the Schrödinger functional. Numerical simulations are performed at several values of the bare coupling β, and for several lattice resolutions L/a. The points at $L/a = 9, 10\frac{2}{3}$ are interpolated.

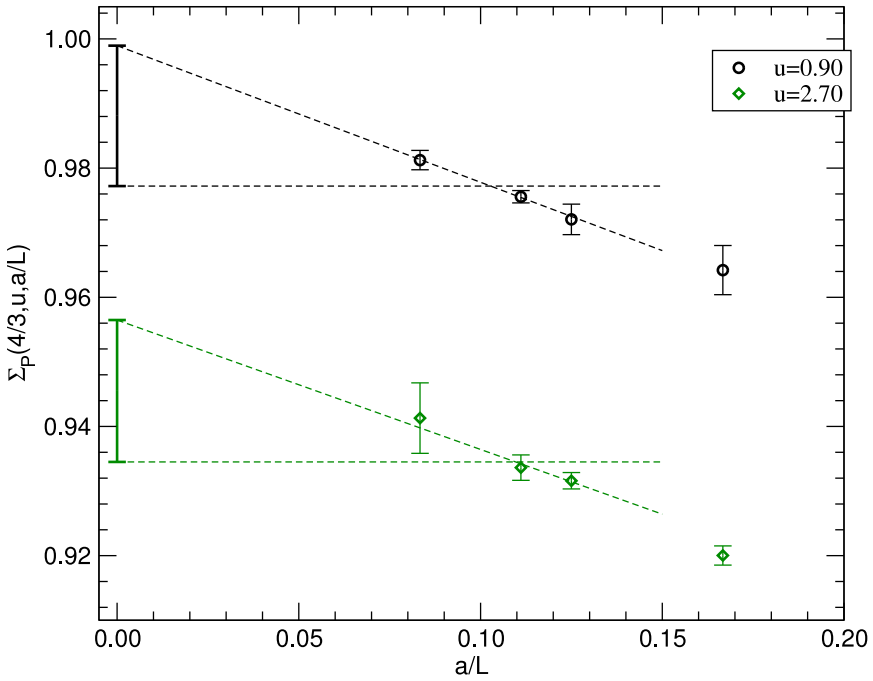

Figure 3.9: Results for the lattice step–scaling function $\Sigma_P(4/3, u, a/L)$. The point at $x = 0$ yields the value of $\sigma_P(u)$, *i.e.* the extrapolation of Σ_P to the continuum limit. The error bar shows the difference between constant and linear extrapolation functions, and gives a conservative estimate of the systematic error in the extrapolation as discussed in the text.

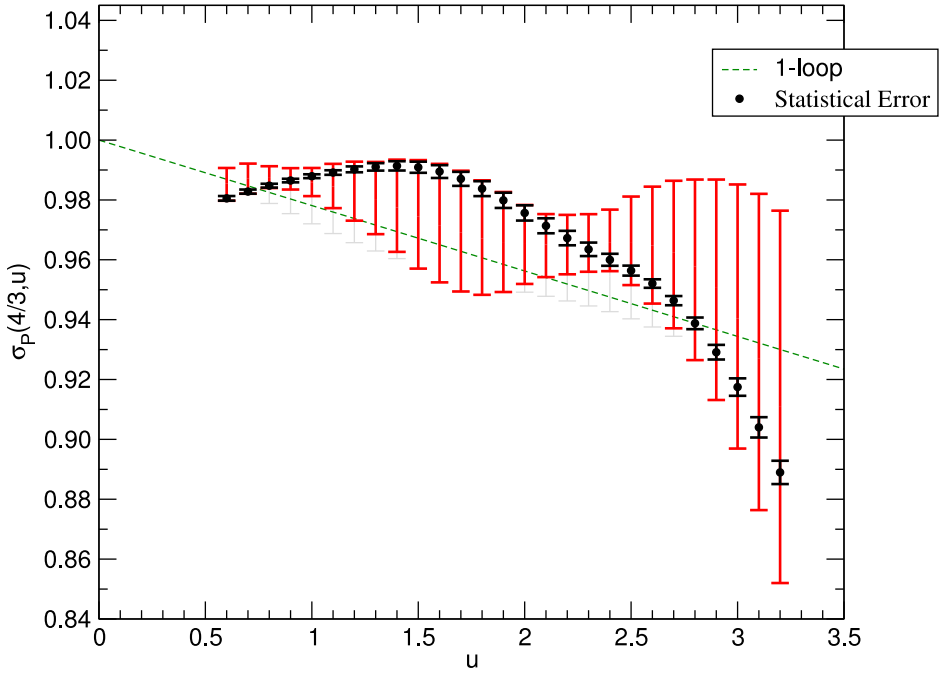

Figure 3.10: The step-scaling function for the running mass $\sigma_P(u)$, using a linear continuum extrapolation. The black circles have a statistical error only, the red error bars include systematic errors using a linear continuum extrapolation. The grey error bars come from also including a constant extrapolation of the two points closest to the continuum, and give an idea of the systematic error in the continuum extrapolation.

β	L=6	L=8	L=12	L=16
2.00	0.3016(6)	-	-	-
2.05	0.3265(11)	-	0.2466(6)	-
2.10	0.3469(6)	-	-	-
2.20	0.3845(6)	0.3550(7)	0.3087(6)	-
2.25	0.4028(6)	0.3707(7)	-	-
2.30	0.4203(6)	0.3841(7)	-	-
2.40	-	0.4134(7)	-	-
2.50	0.4762(6)	0.4406(9)	0.3970(7)	0.3763(39)
2.60	0.5012(7)	0.4624(7)	-	-
2.70	0.5228(6)	-	-	-
2.80	0.5424(7)	0.5025(6)	0.4639(6)	-
3.00	0.5770(7)	0.5381(7)	0.5008(8)	0.4647(55)
3.25	0.6120(6)	-	0.5342(30)	0.5063(44)
3.50	0.6385(7)	0.6030(7)	0.5580(10)	0.5523(43)
3.75	0.6654(6)	-	-	-
4.00	0.6830(6)	0.6501(6)	0.6197(14)	-
4.50	0.7173(7)	0.6859(6)	0.6547(4)	0.6341(27)
8.00	0.8261(3)	0.8114(3)	0.7956(2)	0.7827(11)
16.0	0.9146(4)	0.9082(2)	0.9005(5)	0.8887(15)

Table 3.4: Measured values of Z_P on different volumes as a function of the bare coupling β.

We find good agreement with the 1-loop perturbative prediction, as shown in Fig. 3.10.

In the vicinity of an IRFP the relation between σ_P and γ simplifies. Denoting by γ^* the value of the anomalous dimension at the IRFP, we obtain:

$$\int_{\overline{m}(\mu)}^{\overline{m}(\mu/s)} \frac{dm}{m} = -\gamma^* \int_{\mu}^{\mu/s} \frac{dq}{q}\,, \tag{3.29}$$

and hence:

$$\log|\sigma_P(s,u)| = -\gamma^* \log s\,. \tag{3.30}$$

We can therefore define an estimator

$$\hat{\gamma}(u) = -\frac{\log|\sigma_P(u,s)|}{\log|s|}\,, \tag{3.31}$$

which yields the value of the anomalous dimension at the fixed point. Away from the fixed point $\hat{\gamma}$ will deviate from the anomalous dimension, with the discrepancy becoming larger as the anomalous dimension develops a sizeable dependence on the energy scale.

We plot the estimator $\hat{\gamma}$ in Fig. 3.11. Again the error bars come from evaluating the above expression using the extremal values of $\sigma_P(u)$ at each u. We see that the actual value of $\hat{\gamma}$ is rather small over the range of interest. In

particular at $\overline{g}^2 = 2.2$, the benchmark value for the IRFP tentatively found in Ref. [63], we have $\hat{\gamma} = 0.116^{+43}_{-28}$ using just the linear continuum extrapolation, and $\hat{\gamma} = 0.116^{+76}_{-28}$ if we include the constant continuum extrapolation as well. In the presence of an IRFP $\hat{\gamma}$ yields the value of the anomalous dimension, and therefore the values above can be used to bound the possible values of γ^*. The results of Ref. [63] suggest the IRFP is in the range $\overline{g}^2 = 2.0-3.2$; at the extremes of this range we find $\gamma^* = 0.086^{+85}_{-10}$ and 0.41^{+15}_{-33} using just the linear continuum extrapolation, and $\gamma^* = 0.086^{+105}_{-10}$ and 0.41^{+15}_{-33} including the constant continuum extrapolation. Over the entire range of couplings consistent with an IRFP, γ^* is constrained to lie in the range $0.05 < \gamma^* < 0.56$, even with our more conservative assessment of the continuum extrapolation errors.

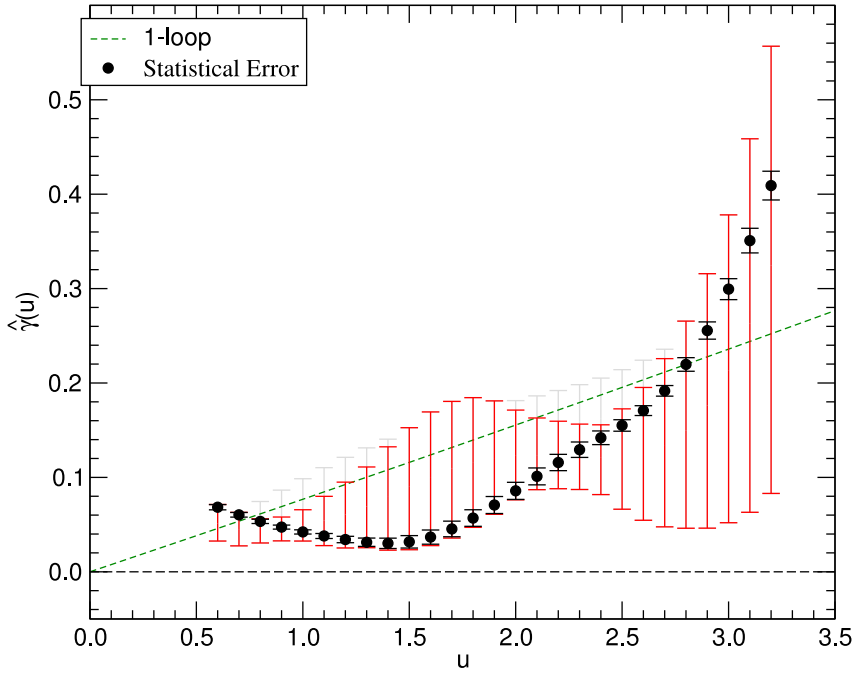

Figure 3.11: The mass anomalous dimension estimator $\hat{\gamma}(u)$. The dashed line shows the 1-loop perturbative result, the black circles have a statistical error only, and the red error bars include systematic errors using a linear continuum extrapolation. The grey error bars also include a constant extrapolation of the two points closest to the continuum, giving an idea of the systematic error involved in the continuum extrapolation.

3.2.4 Conclusion

Our results for the running of the coupling are completely consistent with those of Ref. [63]. While our statistical errors are larger, we have carried out our analysis in a way that aims at disentangling clearly the scale dependence from the lattice artefacts. Our analysis can be systematically improved as more extensive studies are performed, and will ultimately allow us to take the continuum limit with full control over the resulting systematic errors, in particular by using a linear and quadratic extrapolation in place of the current use of a constant and a linear extrapolation. Our results appear to show a slowing in the running of the coupling above $\overline{g}^2 = 2$ or so, and are consistent with the presence of a fixed point where the running stops at somewhat higher $\overline{g}^2$. However, once we include the systematic errors from the continuum extrapolation we find that our results no longer give any evidence for a fixed point. The fundamental reason for this is that the running of the coupling is very slow in this theory and so great accuracy is needed, in particular near a possible fixed point.

By contrast, we find that the behaviour of the anomalous dimension γ is much easier to establish. The systematic errors from the continuum extrapolation are much smaller than the signal, and we find a moderate anomalous dimension, close to the 1-loop perturbative prediction, throughout the range of β explored. In particular, in the range $\overline{g}^2 = 2.0 - 3.2$, where there may be an infrared fixed point, we find $0.05 < \gamma < 0.56$. Our conclusion that γ is not large is unlikely to be affected by using larger lattices. One can see this by considering the continuum extrapolations in Fig. 3.9. For γ to reach 1 in the continuum limit, we would need Σ_P to be $3/4 = 0.75$ at $a/L = 0$. However we see that the dependence on a/L is much too small for this to be possible, and indeed is in the wrong direction. Only a very unlikely conspiracy of lattice artifacts would make it possible for Σ_P to be as small as 0.75 in the continuum limit. On the other hand the value of $\bar{g}$ corresponding to the IRFP is currently not known with sufficient accuracy.

The results presented here are the first computation of the anomalous dimension at a putative fixed point; the systematic errors need to be reduced to make our conclusions more robust. In particular, using larger lattices would give results at smaller a/L and hence make the continuum extrapolations more accurate. It may also be necessary to use an improved action in the long term to achieve the precision required to show the existence of an IRFP or of walking

behaviour. However, as described above, this is very unlikely to affect our phenomenologically most important result, namely that γ is not large, and hence that the theory is not a viable walking technicolor candidate.

3.3 Conformal Technicolor Results

We used the same method to investigate the SU(2) gauge theory with six fundamental Dirac fermions, a candidate Conformal Technicolor theory as described in Sec. 1.4.2. These results are published in Ref. [105].

3.3.1 Lattice parameters

We used the Wilson plaquette gauge action, this time with six flavours of fundamental Wilson fermions, and an RHMC algorithm with 4 pseudofermions. We performed two sets of simulations in order to determine $\overline{g}^2$ and Z_P, the parameters of the runs are summarised in Tab. 3.5. To determine κ_c we measured am for 5 values of κ for each β on $L = 6, 8, 10, 12$ lattices and interpolated to find κ_c for each. We then extrapolated in a/L to determine κ_c for the $L = 14, 16$ lattices.

In practice we achieve $|am| \lesssim 0.005$. At some values of β and L we have additional results at moderately small masses of $|am| \sim 0.01$, shown in Fig. 3.12. We observe no mass-dependence within our statistical errors, confirming that any residual finite-mass errors are extremely small.

We also used more values of L (six instead of four) compared to our previous simulations to improve the quality of the continuum limit extrapolations, and increased the step scaling factor from $s = 4/3$ to $s = 3/2$ to improve the measurement of the slow running of the coupling.

To ensure our results are not affected by the presence of a bulk transition, we measured the average plaquette for a range of values of β and κ, shown in Fig. 3.13. There is a clear jump in the plaquette at low β, implying the presence of a bulk transition. However, this disappears around $\beta = 1.6$. Since the lowest β we use for our measurements of $\overline{g}^2$ and Z_P is $\beta = 2.0$, our results should not be affected by this transition.

3.3.2 Results for the coupling

We measured the coupling $\overline{g}^2(\beta, L)$, for a range of β, L. Our results are shown in Table 3.6, and again we see immediately that the coupling is very similar for different L/a at constant β, so it runs slowly.

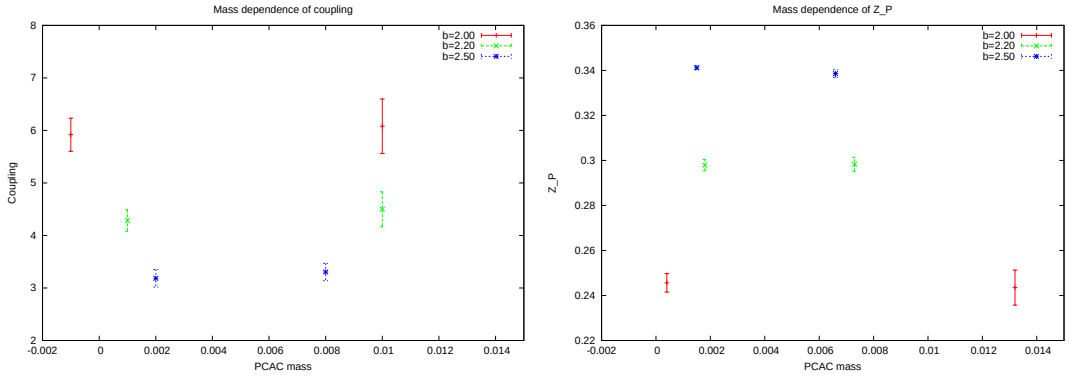

Figure 3.12: A comparison of measurements of $\overline{g}^2$ and Z_P at $m \simeq 0.00$ and $m \simeq 0.01$ on 14^4 lattices. There is no mass–dependence within the statistical errors, confirming that any residual finite-mass errors are extremely small.

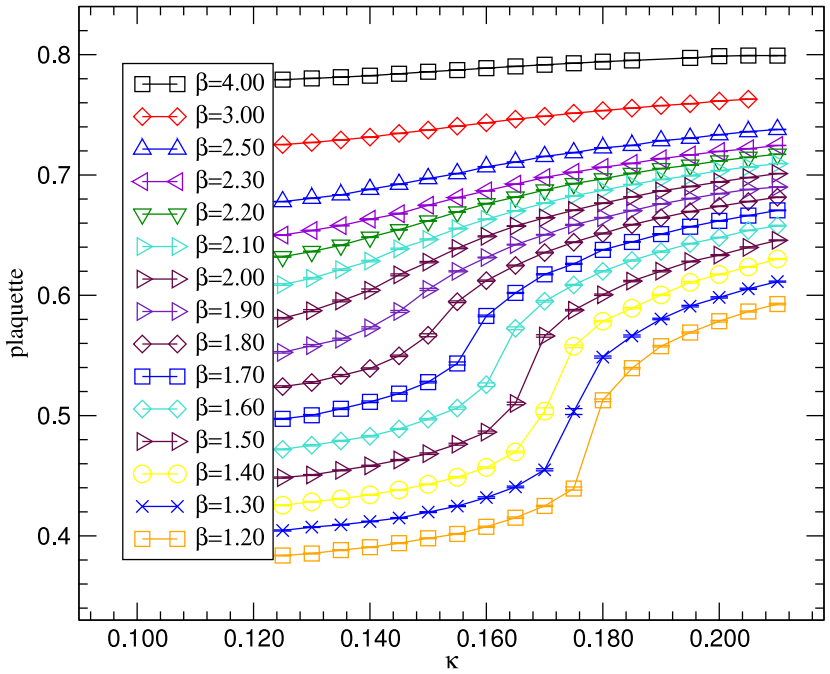

Figure 3.13: The average plaquette for a range of β and κ on 6^4 lattices. The bulk transition occurs around $\beta = 1.6$, well below our lowest value of $\beta = 2.0$.

β	L=6	L=8	$L = 10$	L=12	$L = 14$	L=16
2.0	0.151788	0.150970	0.150576	0.150491	0.150334	0.150252
2.2	0.147447	0.146939	0.146755	0.146782	0.146615	0.146565
2.5	0.143209	0.142825	0.142767	0.142811	0.142730	0.142716
3.0	0.138869	0.138684	0.138651	0.138562	0.138523	0.138493
3.5	0.136130	0.136143	0.136104	0.136103	0.136096	0.136091
4.0	0.134394	0.134350	0.134353	0.134339	0.134332	0.134327
5.0	-	0.132142	0.132142	0.132142	0.132142	0.132142
6.0	0.130753	0.130737	0.130748	0.130740	0.130739	0.130738
8.0	0.129131	0.129145	0.129167	0.129172	0.129177	0.129182

Table 3.5: Values of β, L, κ used for the determination of $\overline{g}^2$ and Z_P. The entries in the table are the values of κ_c used for each combination of β and L.

β	L=6	L=8	$L = 10$	L=12	$L = 14$	L=16
2.0	4.941(61)	5.521(143)	6.053(418)	6.109(289)	5.913(362)	5.726(485)
2.2	3.755(32)	4.025(70)	4.390(158)	4.506(345)	4.279(233)	4.379(252)
2.5	2.973(21)	3.038(37)	3.103(72)	3.170(67)	3.187(174)	3.316(151)
3.0	2.123(10)	2.173(20)	2.150(37)	2.291(90)	2.336(55)	2.338(75)
3.5	1.660(8)	1.707(37)	1.730(20)	1.751(29)	1.825(50)	1.715(46)
4.0	1.376(4)	1.390(8)	1.425(16)	1.399(30)	1.420(19)	1.445(31)
5.0	-	1.033(3)	1.054(7)	1.050(9)	1.063(15)	1.041(16)
6.0	0.814(1)	0.822(3)	0.823(6)	0.842(6)	0.829(12)	0.827(11)
8.0	0.576(1)	0.581(1)	0.575(3)	0.586(3)	0.585(6)	0.593(6)

Table 3.6: The entries in the table are the measured values of $\overline{g}^2$ for each combination of β and L.

$\overline{g}^2$	L/a							
	8	$9\frac{1}{3}$	10	$10\frac{2}{3}$	12	14	15	16
params	3	4	4	4	3	2	2	2
χ^2/dof	1.92	0.54	1.24	0.48	1.66	1.54	1.88	1.36

Table 3.7: Interpolation best fit parameters for $\overline{g}^2$.

We first discard the $L = 6$ data since we found it had large lattice artifacts. We then interpolate the remaining data quadratically in a/L at each β to find $\overline{g}^2(\beta, L)$ at $L = 9\frac{1}{3}, 10\frac{2}{3}, 15$. Then for each L we interpolate in β using the functional form [80, 43]

$$\frac{1}{\overline{g}^2(\beta, L/a)} = \frac{\beta}{2N}\left[\sum_{i=0}^{n} c_i \left(\frac{2N}{\beta}\right)^i\right]. \tag{3.32}$$

We choose the smallest n which results in a χ^2 such that the fit is not ruled out at a 95% CL, and also use $n + 1$ as the next best fit; this gives a 2-5 parameter fit in each case. The number of parameters we use for each L/a and the χ^2/dof for each fit are shown in Tables 3.7 and 3.8.

We now calculate $\Sigma(u, s, a/L)$ using the fits from Eq. 3.32 for $L = 8, 9\frac{1}{3}, 10, 10\frac{2}{3}$ and $s = 3/2$. Finally we extrapolate to $a/L = 0$ to obtain $\sigma(u, s)$.

We carry out a constant continuum extrapolation, using the data at the two values of a/L closest to the continuum limit. We estimate the errors using the same multistage bootstrapping procedure as before, described in Appendix B.1. We have also attempted a linear continuum extrapolation, but the statistical errors on our results are still too large for reliable fits, as shown in Fig. 3.14. Thus the choice of continuum extrapolation remains as a systematic error on our results.

The results for $\sigma(u)$ using the constant continuum extrapolation are plotted in Fig. 3.15, where the statistical errors only are in black and the error from changing the number of fitting parameters are in grey. Our results are consistent with a fixed point in the region $\overline{g}^2 > 4.02$. They are also compatible with the possibility that there is no fixed point at all in the range of couplings we have measured. However, it is clear that $\sigma(u)$ is considerably below the 1-loop prediction at strong coupling.

In the vicinity of a fixed point at a coupling g^*, the beta function is linear in

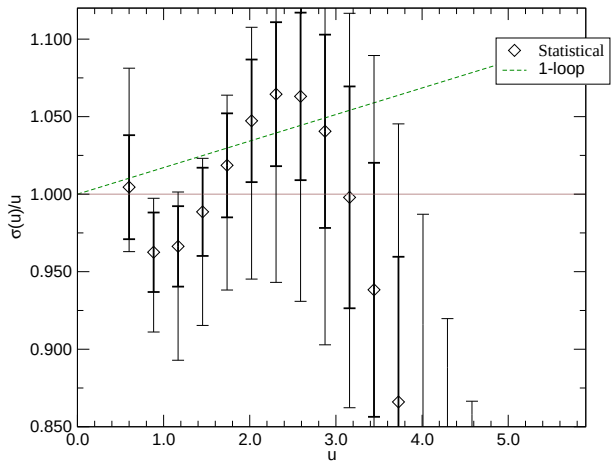

Figure 3.14: $\sigma(u)$ using a linear continuum extrapolation of the four points closest to the continuum. Statistical error using the optimal fit parameters in black, systematic error from using different numbers of parameters in the fits in grey.

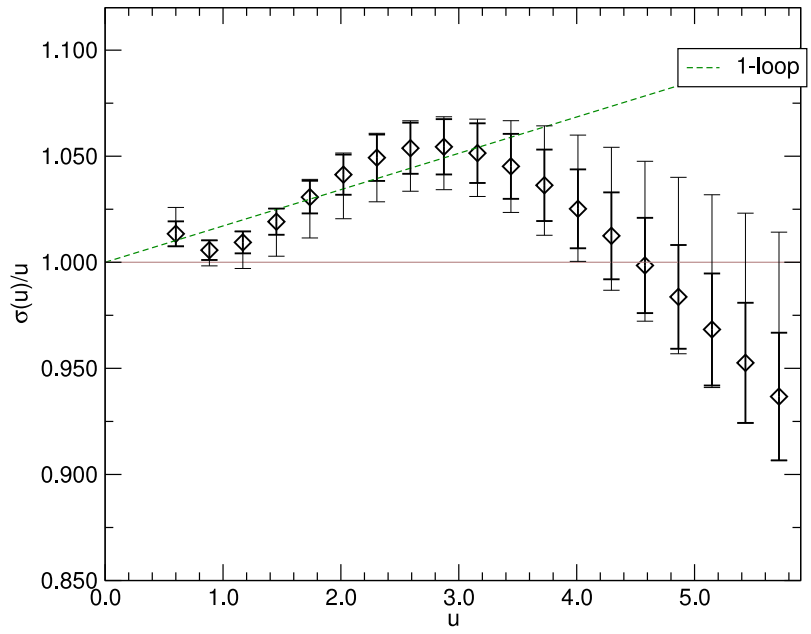

Figure 3.15: $\sigma(u)$ using a constant continuum extrapolation of the two points closest to the continuum. Statistical error using the optimal fit parameters in black, systematic error from using different numbers of parameters in the fits in grey.

$\overline{g}^2$	L/a							
	8	$9\frac{1}{3}$	10	$10\frac{2}{3}$	12	14	15	16
params	4	5	5	5	4	3	3	3
χ^2/dof	1.25	0.58	1.42	0.54	1.19	1.61	1.06	1.05

Table 3.8: Interpolation next-best fit parameters for $\overline{g}^2$.

the coupling,

$$\beta(g) = \beta^*(g - g^*) + ... \tag{3.33}$$

where β^* is a scheme-independent coefficient, which, as described in Ref. [39], yields further information on the physics of these theories. In terms of the step-scaling function $\sigma(u, s)$, this gives:

$$\sqrt{\sigma}(u, s) = g^* + (\sqrt{u} - g^*)s^{-\beta^*}. \tag{3.34}$$

We have estimated β^* by fitting $\sigma(u, s)$ in the vicinity of the fixed point, and find $\beta^* = 0.62(12)^{+13}_{-28}$, where the first error is statistical and the second is systematic, for those fits where we see a fixed point in the range of couplings covered by our data. This does not include the systematic error due to the choice of a constant rather than a linear continuum extrapolation. Better data would be needed to make the systematic errors on β^* more robust.

3.3.3 Running mass

We measured the pseudoscalar density renormalisation constant Z_P for a range of β, L. Our results are shown in Tab. 3.9 and Fig. 3.16. We see that Z_P decreases with increasing L/a at constant β, indicating a positive anomalous mass dimension, but the running appears to be slow.

To extract γ we first calculate $\Sigma_P(u, s, a/L)$, defined in Eq. 3.25, then proceed similarly as for $\Sigma(u, s, a/L)$. We first discard the $L = 6$ data, and then interpolate quadratically in a/L to find $Z_P(\beta, L)$ at $L = 9\frac{1}{3}, 10\frac{2}{3}, 15$. Then for each L we interpolate in β using the functional form in Eq. 3.27. We choose the smallest n which results in an acceptable χ^2, as for the $\overline{g}^2$ fits; this gives a 5-6 parameter fit in each case. We also use $n + 1$ as a next-best fit to estimate the systematic errors from the choice of n. The number of parameters we use for each L/a and the χ^2/dof for each fit are shown in Tables 3.10 and 3.11.

We can now calculate $\Sigma_P(u, s, a/L)$ using Eq. 3.25 and the fits from Eq. 3.27,

β	L=6	L=8	$L = 10$	L=12	$L = 14$	L=16
2.00	0.26636(249)	0.27219(306)	0.27117(241)	0.25956(527)	0.24564(414)	0.24130(578)
2.20	0.33220(167)	0.32060(216)	0.30788(537)	0.30929(137)	0.29792(246)	0.29198(215)
2.50	0.37504(32)	0.36203(49)	0.35095(87)	0.34672(73)	0.34118(88)	0.33255(162)
3.00	0.40488(21)	0.39186(31)	0.38451(52)	0.37955(50)	0.37453(53)	0.37170(56)
3.50	0.42102(30)	0.40981(82)	0.40383(32)	0.39832(43)	0.39461(62)	0.39241(93)
4.00	0.43105(14)	0.42192(21)	0.41691(31)	0.41256(34)	0.40997(29)	0.40746(36)
6.00	0.45368(8)	0.44908(12)	0.44597(16)	0.44417(10)	0.44232(15)	0.44045(20)
8.00	0.46540(5)	0.46229(7)	0.46005(10)	0.45822(7)	0.45683(10)	0.45575(9)

Table 3.9: The entries in the table are the measured values of Z_P for each combination of β and L.

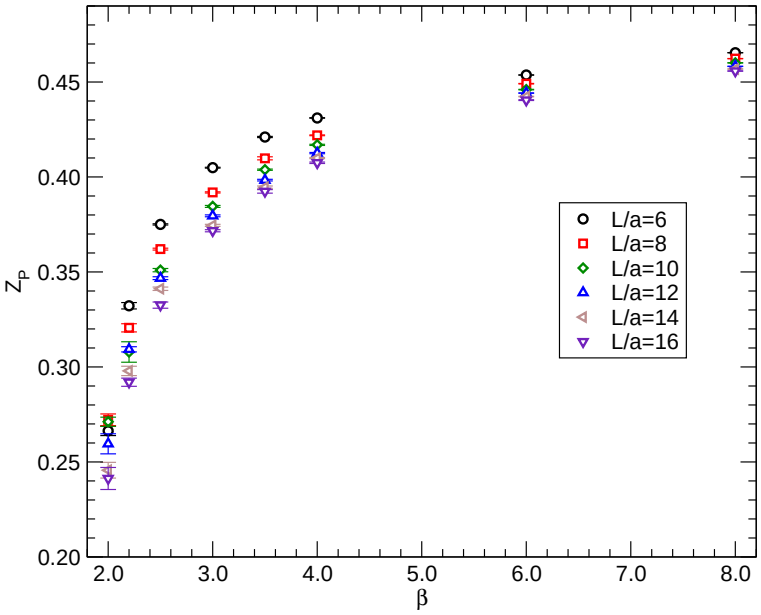

Figure 3.16: Data for the renormalisation constant Z_P as computed from lattice simulations of the Schrödinger functional. Numerical simulations are performed at several values of the bare coupling β, and for several lattice resolutions L/a.

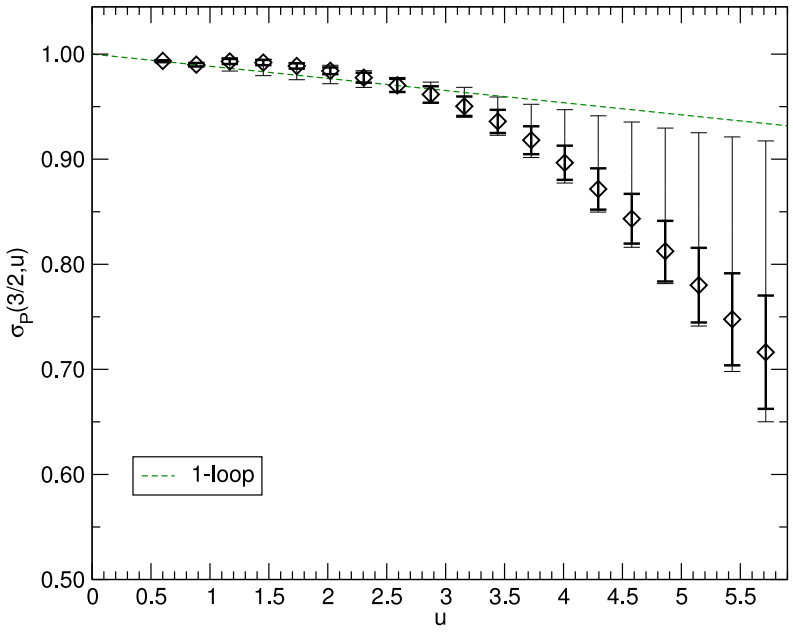

Figure 3.17: $\sigma_P(u)$ using both a constant continuum extrapolation of the two points closest to the continuum, and a linear continuum extrapolation. Statistical error using the optimal fit parameters with a linear continuum extrapolation in black, systematic error including the choice of continuum extrapolation in grey.

and finally extrapolate to the continuum limit to obtain $\sigma_P(u, s)$. The errors are smaller than for the running coupling, so we are able to use both constant and linear continuum extrapolations to control the systematic error from the choice of extrapolation. We estimate the errors using the same multistage bootstrapping procedure as before, described in Appendix B.2

We plot σ_P in Figure 3.17, where the statistical error is in black, and the systematic error arising both from the choice of the number of fit parameters and the continuum extrapolation is in grey. We also plot the 1-loop perturbative prediction for σ_P. Our results are close to the 1-loop prediction, with the running becoming a little faster at strong couplings.

In the vicinity of an IRFP, we can define an estimator $\hat{\gamma}(u)$, see Eq. 3.31, which is equal to the anomalous dimension γ at the fixed point, and deviates away from

$\overline{g}^2$	L/a							
	8	$9\frac{1}{3}$	10	$10\frac{2}{3}$	12	14	15	16
params	6	5	5	5	5	5	5	5
χ^2/dof	1.79	0.86	1.09	0.62	0.99	1.60	1.63	1.22

Table 3.10: Interpolation best fit parameters for Z_P.

$\overline{g}^2$	L/a							
	8	$9\frac{1}{3}$	10	$10\frac{2}{3}$	12	14	15	16
params	7	6	6	6	6	6	6	6
χ^2/dof	2.09	0.46	1.03	0.43	1.18	0.93	1.32	1.47

Table 3.11: Interpolation next-best fit parameters for Z_P.

the fixed point as the anomalous dimension begins to run. We plot this estimator in Figure 3.18. Again the black error bars show the statistical errors, and the grey the systematic errors. We see that $\hat{\gamma}(u)$ is small in most of the range of couplings that we measure. However, it becomes larger at our strongest couplings. Our data is consistent with it reaching values $\gamma \approx 1$ that are interesting for models of technicolor, although our error bars are large and it is also possible that it is as small as 0.135, our lower bound at $\overline{g}^2 = 4.02$, the smallest coupling at which a fixed point is consistent with our results. The highest value compatible with our data is $\hat{\gamma} = 1.03$ at $\overline{g}^2 = 5.52$, the highest coupling at which we have results for all L.

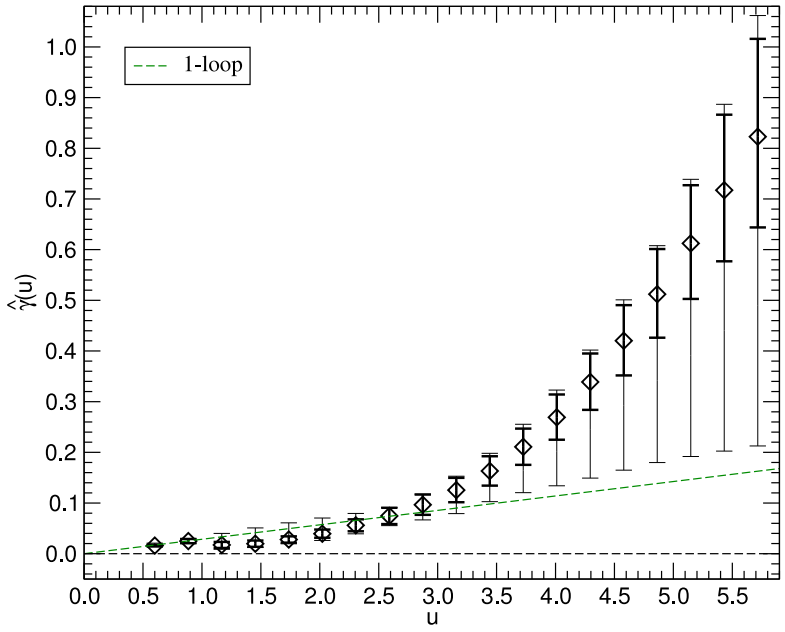

Figure 3.18: $\hat{\gamma}(u)$ using both a constant continuum extrapolation of the two points closest to the continuum, and a linear continuum extrapolation. Statistical error using the optimal fit parameters with a linear continuum extrapolation in black, systematic error including the choice of continuum extrapolation in grey.

3.3.4 Conclusion

Our results for the running of the coupling have relatively large errors. This is due to the difficulty of measuring the small difference in the coupling between two nearby scales, a problem that becomes particularly acute as we approach a possible fixed point where the difference falls. We observe that the running of the coupling is slower than the (already slow) one-loop perturbative prediction. Our results are consistent with the presence of a fixed point above $\overline{g}^2 = 4.02$, but the large errors prevent us from distinguishing a fixed point from merely slow running. We have not been able to perform a linear continuum extrapolation for the coupling, which introduces an additional uncertainty.

Our results for the running of the mass are clearer. We find the anomalous dimension is small throughout most of the range of couplings we measure, but it becomes larger for our strongest couplings, with a possibility that it reaches values around 1. If true, this would be very interesting for technicolor models. The accuracy of our results would be improved in particular by using larger lattices, which would give a larger range of a/L for the continuum extrapolations. This would help to clarify the existence and location of the fixed point, and to reduce the errors on the anomalous dimension.

For both Minimal Walking Technicolor and Conformal Technicolor we have performed Schrödinger Functional simulations to measure the running of the coupling and the mass. We have found slow running of the coupling in both cases, and a relatively small anomalous dimension, but we were unable to conclusively identify a fixed point in the coupling in either case. Simulating on larger lattices, and possibly with an improved action, should resolve this issue.

In the meantime, if we could somehow measure the anomalous mass dimension at the fixed point, without having to find the value of the coupling at the fixed point, we would avoid the main difficulty in the Schrödinger Functional method. The MCRG method could potentially allow us to do exactly this, and is described in the following chapter.

Chapter 4

Monte Carlo Renormalisation Group Method

4.1 Introduction

In the Schrödinger Functional method we measured a discrete version of the Callan-Symanzik equations, where a fixed point was indicated by a zero of the β function. Another approach to studying Renormalisation Group transformations is to use the inherently non-perturbative Wilson RG. Here the evolution of all possible couplings that preserve the internal symmetries of the system are considered, and cut-off level UV modes are integrated out. Fixed points are characterised by the number of relevant couplings (ones with positive scaling dimensions, that flow away from the FP). Irrelevant couplings have negative scaling dimensions, and flow towards the FP, so that their IR values are independent of their UV values. This is qualitatively illustrated in Fig 4.1.

The Monte Carlo Renormalisation Group [106] has been used to study the critical properties of various models on the lattice. In particular the 2–lattice matching technique used in this work was first used to investigate quenched QCD [107, 108, 109], and more recently QCD with many flavours of fermions [81, 82].

This method was used to measure the running of the coupling and the mass in Minimal Walking Technicolor, the SU(2) gauge theory with two adjoint Dirac fermions described in Sec. 1.4.1. Some of these results are published in Ref. [110].

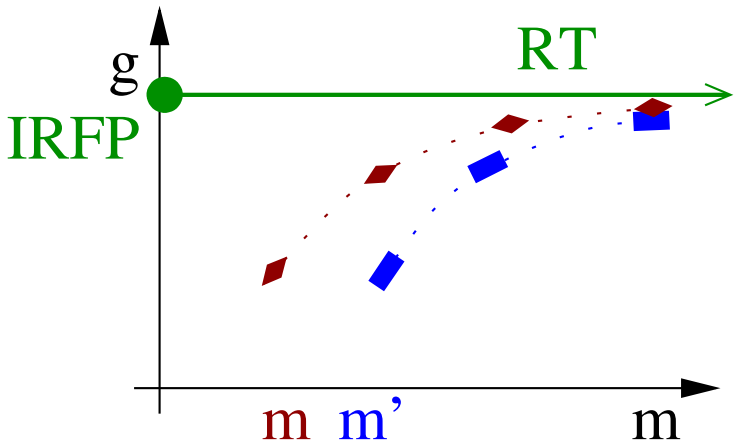

Figure 4.1: An example of RG flow under blocking steps near an IRFP with one relevant coupling, m, and one irrelevant coupling, g. The irrelevant coupling flows to it's FP value, while the relevant coupling flows away from the FP.

4.2 Method

With each RG step, changing the scale by a factor s, irrelevant couplings will flow towards the fixed point, and relevant couplings will flow away from it. After a few steps the irrelevant couplings should die out, leaving the flow following the unique renormalised trajectory (RT). If we can identify two sets of couplings which end up at the same point along the RT after the same number of steps, then they must have the same lattice correlation lengths, $\hat{\xi} = \hat{\xi}'$. Since the physical correlation length $\xi = \hat{\xi}a$ should not be changed by the RG transform, this means that they both must have the same lattice spacing a, or inverse cutoff $\Lambda^{-1} \sim a$. If they end up at the same point, but one takes an extra step, then their lattice correlation lengths must differ by a factor s, and hence so must their UV cutoffs.

To identify such a pair of couplings, we need to show that after n and $(n-1)$ RG steps respectively their actions are identical. Explicitly calculating the flow of the couplings in the action would be complicated, but instead the gauge configurations themselves can be RG block transformed, and showing that the expectation values of all observables on these gauge configurations agree is equivalent to directly comparing the actions that generated them.

4.2.1 2–Lattice Matching Procedure

Starting with the SU(2) pure gauge theory, where the gauge coupling is the only revelant parameter, the procedure is as follows.

1. Generate an ensemble of gauge configurations with an action $S(\beta)$ on a L^4 lattice.

2. Block these n times to produce an ensemble of configurations on a $(L/s^n)^4$ lattice, and measure the expectation values of various observables on them.

3. Generate a new ensemble of gauge configurations with an action $S(\beta')$ on a $(L/s)^4$ lattice, for a range of values of β'.

4. Block each of these $n-1$ times to produce an ensemble of configurations on a $(L/s^n)^4$ lattice, and measure the same observables for each β'.

5. Interpolate in β' such that each observable after taking n steps on the larger lattice agrees with the same observable after taking $(n-1)$ steps on the smaller lattice.

6. Repeat for different n, e.g. for $s = 2, L = 32$, three values can be used: $n = 2, 3, 4$.

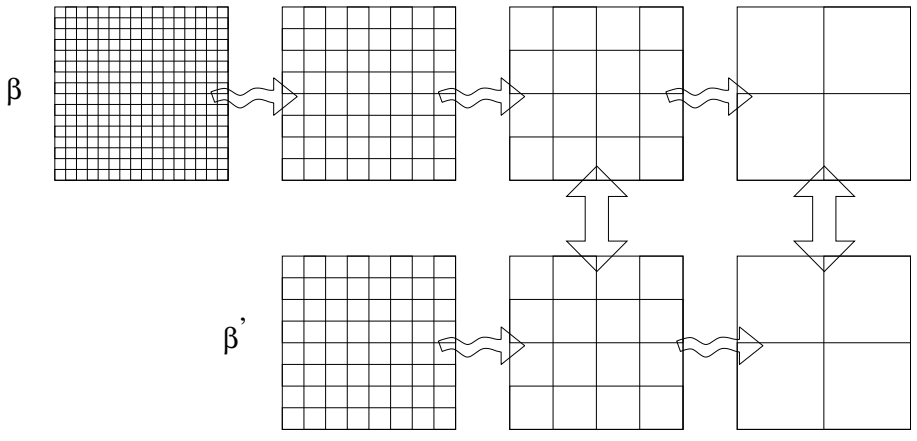

Figure 4.2: The 2–lattice matching procedure described in Sec. 4.2.1. Horizontal arrows represent RG blocking steps, and vertical arrows indicate matched lattices. In this case the matching is done after 2(1) and 3(2) blocking steps on the $16^4(8^4)$ lattices.

We have now identified, for each n, a pair of bare gauge couplings (β, β'), with lattice correlation lengths that differ by a factor s, $\hat{\xi}' = \hat{\xi}/s$. In the limit $n \to \infty$, the quantity

$$\Delta\beta = \beta - \beta' \equiv s_b(\beta; s) \tag{4.1}$$

is the step scaling function for the bare gauge coupling. This is the analog of the Schrödinger Functional step scaling function for the renormalised coupling, $\sigma(u, s)$, and in the UV limit where $\overline{g}^2 \to g_0^2 = 2N/\beta$, there is a simple relation between the two:

$$\frac{s_b(\beta; s)}{\beta} = \frac{\sigma(u, s)}{u} - 1. \tag{4.2}$$

We use the following $s = 2$ RG blocking transform, labelled ORIG following the naming convention used in Ref. [81],

$$V^{\mathrm{ORIG}}_{n,\mu} = Proj\left[(1-\alpha)U_{2n,\mu}U_{2n+\hat{\mu},\mu} + \frac{\alpha}{6}\sum_{\nu\neq\mu} U_{2n,\nu}U_{2n+\hat{\nu},\mu}U_{2n+\hat{\mu}+\hat{\nu},\mu}U^{\dagger}_{2n+2\hat{\mu},\nu}\right], \tag{4.3}$$

where U is the original gauge field on a L^4 lattice, V is the blocked gauge field on a $(L/2)^4$ lattice, and α is a free parameter, which can be varied to optimise the transformation. Changing α changes the location of the FP, and how quickly the unique RT is approached in a given number of steps. Ideally it should be chosen such that

- All operators predict the same matching coupling between $(n, n-1)$ pairs for a given blocking step n. (Deviations are a measure of the systematic error from not being at exactly the same point along the RT)
- Consecutive blocking steps predict the same matching coupling, i.e. the coupling for which $(n, n-1)$ pairs agree should be the same for all n. (Deviations show that the RT is still being approached in the irrelevant directions)

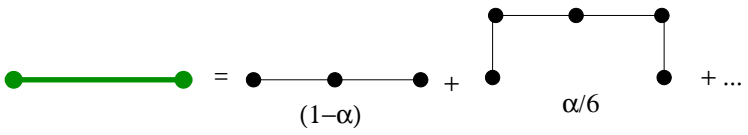

Figure 4.3: The ORIG blocking transform defined in Eq 4.3.

We also use two different $s = 2$ RG blocking transforms constructed using HYP smeared links, labelled HYP and HYP2 [82]. HYP blocking uses a product of HYP smeared links with smearing parameters $(\alpha, 0.6, 0.3)$,

$$V^{\mathrm{HYP}}_{n,\mu} = W[U]_{2n,\mu} W[U]_{2n+\hat{\mu},\mu} \tag{4.4}$$

where U is the original gauge field and $W[U]_{x,\mu}$ is the HYP smeared link at (x, μ).

The HYP smeared link $W[U]_{x,\mu}$ is constructed in three stages [111], each stage consisting of a modified APE blocking step [112] projected back into the gauge group. In the first stage a set of decorated links $\bar{V}$ are constructed from the original links U,

$$\bar{V}_{n,\mu;\nu\,\rho} = Proj\left[(1-\alpha_3)U_{n,\mu} + \frac{\alpha_3}{2}\sum_{\pm\eta\neq\rho,\nu,\mu} U_{n,\eta}U_{n+\hat{\eta},\mu}U^{\dagger}_{n+\hat{\mu},\eta}\right]. \tag{4.5}$$

From these a second set of decorated links $\tilde{V}$ are constructed,

$$\tilde{V}_{n,\mu;\nu} = Proj\left[(1-\alpha_2)U_{n,\mu} + \frac{\alpha_2}{4}\sum_{\pm\rho\neq\nu,\mu} \bar{V}_{n,\rho;\nu\,\mu}\bar{V}_{n+\hat{\rho},\mu;\rho\,\nu}\bar{V}^{\dagger}_{n+\hat{\mu},\rho;\nu\,\mu}\right], \tag{4.6}$$

and finally the HYP smeared links are constructed from this second set of dressed links,

$$W[U]_{n,\mu} = Proj\left[(1-\alpha_1)U_{n,\mu} + \frac{\alpha_1}{6}\sum_{\pm\nu\neq\mu} \tilde{V}_{n,\nu;\mu}\tilde{V}_{n+\hat{\nu},\mu;\nu}\tilde{V}^{\dagger}_{n+\hat{\mu},\nu;\mu}\right]. \tag{4.7}$$

HYP2 blocking is the same except that HYP smearing is applied twice to each link with smearing parameters $(\alpha, 0.3, 0.3)$.

$$V^{\mathrm{HYP2}}_{n,\mu} = W^2[U]_{2n,\mu} W^2[U]_{2n+\mu,\mu} \tag{4.8}$$

Using these HYP and HYP2 blocking transforms in addition to the ORIG blocking transform is a useful check that the results are independent of the choice of blocking.

4.3 Pure Gauge Results

As an initial test of the method, matching in β between 32(16) and 16(8) lattices was performed using $\sim$ 2000 SU(2) pure gauge configurations for each β. We matched in the plaquette, the three six-link loops, and three 8-link loops, shown in Fig. 4.4. Explicit expressions for the seven observables used in the matching are given in Appendix F.1.

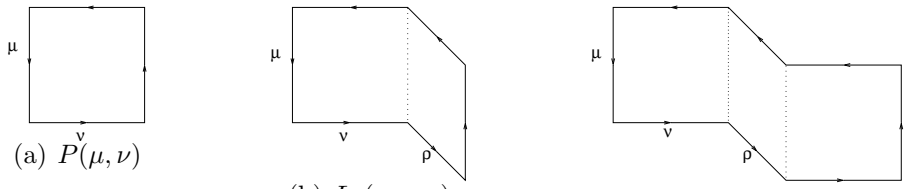

(a) $P(\mu, \nu)$ (b) $L_6(\mu, \nu, \rho)$ (c) $L_8(\mu, \nu, \rho, \alpha)$

Figure 4.4: The plaquette, 6-link and 8-link gauge observables used in the matching.

An example of the matching of the plaquette is shown in Figure 4.5(a). The red, green and blue horizontal lines show the average plaquette on the 32^4 lattice after 2, 3 and 4 ORIG blocking steps respectively, at $\beta = 3.0, \alpha = 0.57$. The interpolated red, green and blue points show the average plaquette on the 16^4 lattice after 1, 2 and 3 blocking steps respectively, as a function of β', also at $\alpha = 0.57$. The value of β' where the two red lines intersect gives the matching coupling for $n = 2$, similarly the green and blue lines give the matching coupling for $n = 3$ and 4.

This matching is repeated for each observable, and the spread of predicted matchings for each n gives a systematic error on the central matching value. The whole procedure is then repeated for various values of α, as shown in Figure 4.5(b), to find an optimal value of α where subsequent RG steps predict the same matching value. The intersection of the last two blocking steps gives a central value for $s_b(\beta = 3.0; s = 2)$, while the range of couplings for which any of the blocking steps intersect within errors gives the uncertainty on this central value. This was repeated for other values of β, and also with the HYP and HYP2 blocking transforms. Figure 4.6 shows the resulting step scaling of the bare coupling s_b, determined using ORIG, HYP and HYP2 blocking on both 32(16) and 16(8) lattices, along with the 1-loop and 2-loop perturbative predictions.

In the scaling region s_b agrees well with the perturbative prediction, and the agreement between the different blocking transforms and lattice sizes shows that finite size errors are small, at least for the pure gauge case.

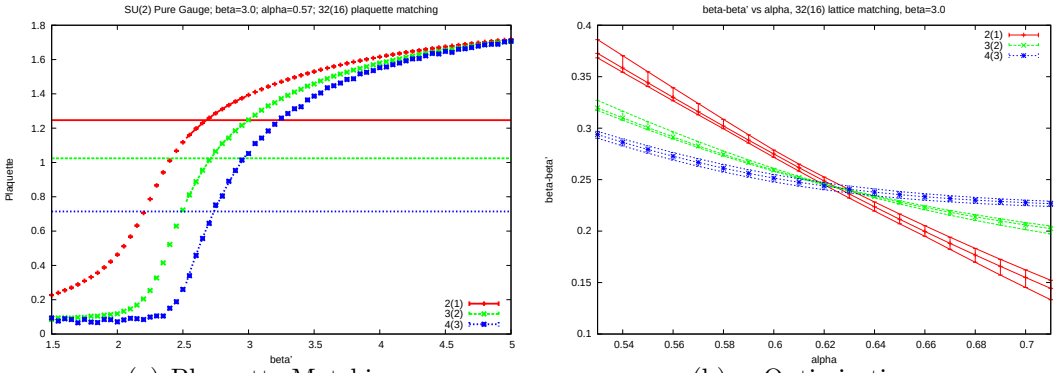

(a) Plaquette Matching (b) α-Optimisation

Figure 4.5: An example of the matching of the plaquette in β for the pure gauge case using ORIG blocking on 32(16) lattices. This is repeated for each observable to give a systematic error for each matching, then α is varied such that all blocking steps predict the same matching.

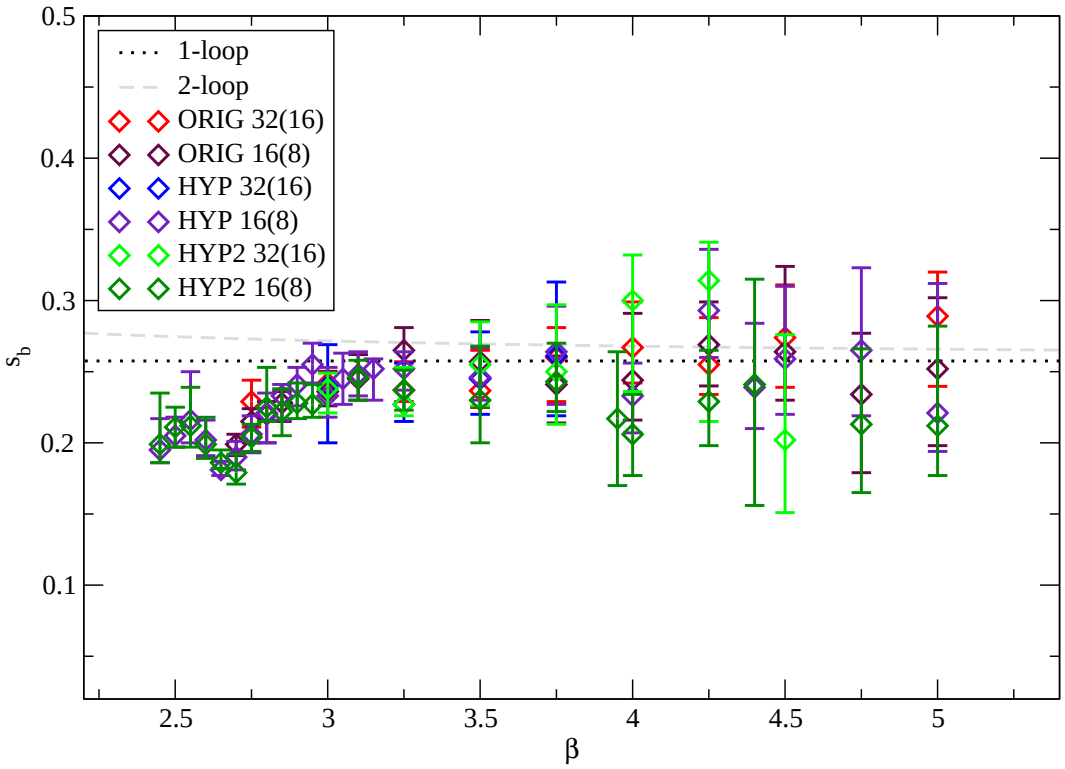

Figure 4.6: Bare step scaling s_b for the pure gauge theory. Matching is performed on 32(16) and 16(8) lattices using ORIG, HYP and HYP2 blocking transforms. All give results consistent with each other and with perturbation theory.

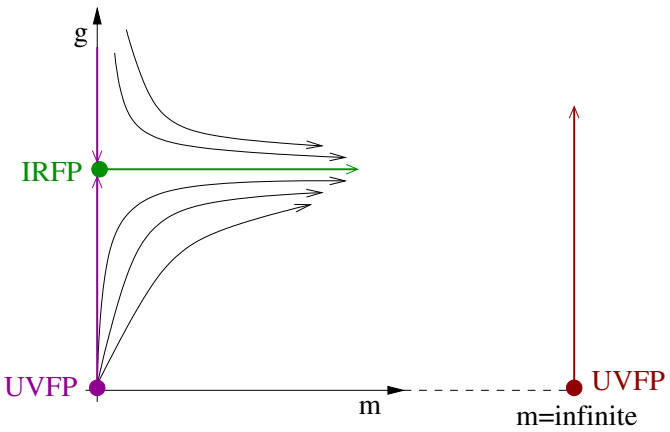

Figure 4.7: Phase diagram showing RG flows near an IRFP with an irrelevant coupling g and a relevant coupling m. Also shown is the flow near a UVFP at infinite mass with a relevant coupling g, which corresponds to the pure SU(2) gauge theory.

4.4 MWT Results - Anomalous Dimension

Having confirmed that the 2–lattice MCRG method works for the SU(2) pure gauge case, we now turn to the full Minimal Walking Technicolor theory of two Dirac fermions in the adjoint representation of SU(2).

There are two couplings of interest in this theory, the gauge coupling and the mass. At an IRFP the gauge coupling is expected to be irrelevant, leaving the mass as the only relevant operator, as shown qualitatively in Fig. 4.7. So we should in principle be able to match in the mass at arbitrary couplings, as long as we have sufficient RG steps for the gauge coupling to flow to its FP value. In practice we only have a small number of RG steps, and the coupling flows slowly towards its FP value, so we set $\beta' = \beta$ assuming the flow in the coupling is negligible. We match observables as for the pure gauge case, but instead of matching in β, we fix $\beta' = \beta$, and match pairs of bare masses (m, m').

We use the Wilson plaquette gauge action with adjoint Wilson fermions and an RHMC algorithm with two pseudofermions. We generated ~ 3000 configurations on 16^4 and 8^4 lattices, for a range of bare masses at each β. This allows two matching steps, after 2(1) and 3(2) steps on the $16^4(8^4)$ lattices respectively. See Fig 4.8 for an example of this matching and subsequent α–optimisation.

Because the bare mass is additively renormalised we convert the bare masses to PCAC masses. We measure the PCAC mass, $\overline{m}$, as a function of bare mass for each β, as shown in Figure 4.9. We do this on the largest lattices we have in order to minimise finite volume effects, and then use this to convert the bare masses on both 8^4 and 16^4 lattices to PCAC masses. Our previous result [110] for the anomalous mass dimension used PCAC masses measured on the 8^4 lattices which suffer from a significant finite volume effect, as described in App F.2, which has been removed in the present work.

$$\overline{m} = m_{PCAC}\left(\tfrac{L}{2}\right), \quad m_{PCAC}(x_0) = \frac{D_0^s f_A(x_0)}{2 f_P(x_0)} \tag{4.9}$$

The anomalous mass dimension appears in the RG equation for the mass

$$\frac{d\overline{m}}{d\ln|\mu|} = -y_m \overline{m} = -(1+\gamma)\overline{m} \tag{4.10}$$

At an IRFP the anomalous mass dimension is a constant, so the expression can

β	γ	$d.o.f.$
2.15	$-0.07(10)$	3
2.25	$-0.02(12)$	6
2.35	$-0.09(17)$	5
2.50	0.12(15)	5
all	$-0.03(13)$	22

Table 4.1: Fitted values of γ for each set of β, and a combined fit - all are consistent with a vanishing anomalous mass dimension.

be integrated to give

$$\frac{\overline{m}'}{\overline{m}} = 2^{\gamma+1} \tag{4.11}$$

for a pair of matching masses $(\overline{m}, \overline{m}')$, from which a value for γ can be extracted. We used four values of β, $\beta = 2.15, 2.25, 2.35, 2.50$, and the matching PCAC mass pairs using the HYP blocking transform are shown in Fig. 4.10. We also repeated the matching using ORIG and HYP2 blocking. A comparison of the three blocking methods is shown for each β value in Fig 4.13, and the agreement between them is very good.

Different β values seem to predict consistent values for the anomalous mass dimension, as shown in Fig. 4.11, which uses all the beta values and masses in the range $0.02 < m < 0.14$. Masses above this range are excluded because the data are no longer consistent with a linear fit, as can be see in Fig. 4.10, suggesting that we are beyond the small–mass linear scaling region described by Eq. 4.11. The masses below $m = 0.02$ are excluded because they are likely to contain a significant unwanted contribution from the running of the coupling, as described in Appendix F.3.

The $\chi^2/d.o.f.$ for a linear fit of the form in Eq. 4.11 is shown in Fig. 4.12, and the resulting values for γ are listed in Tab. 4.1. The fits favour a vanishing anomalous mass dimension, and a combined fit to all β and m gives $\gamma = -0.03(13)$, with $\gamma > 0.13$ ruled out at a 95% confidence level.

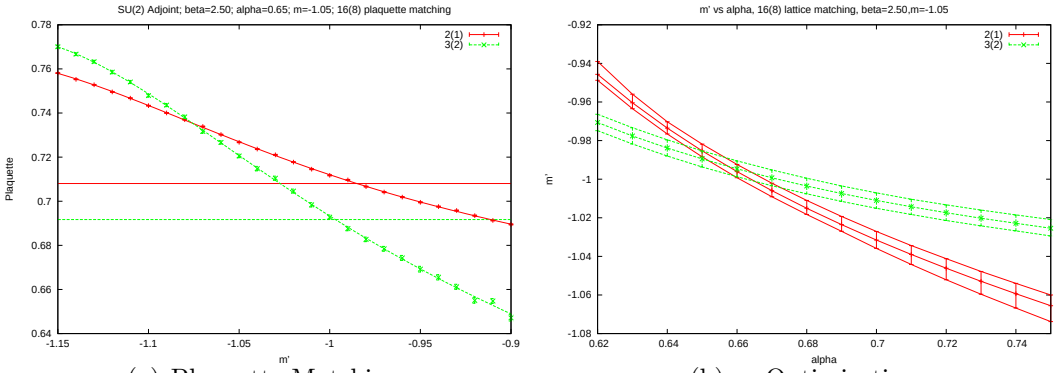

(a) Plaquette Matching (b) α–Optimisation

Figure 4.8: An example of the matching of the plaquette in the bare mass m. This is repeated for each observable to give a systematic error for each matching, then α is varied such that all blocking steps predict the same matching.

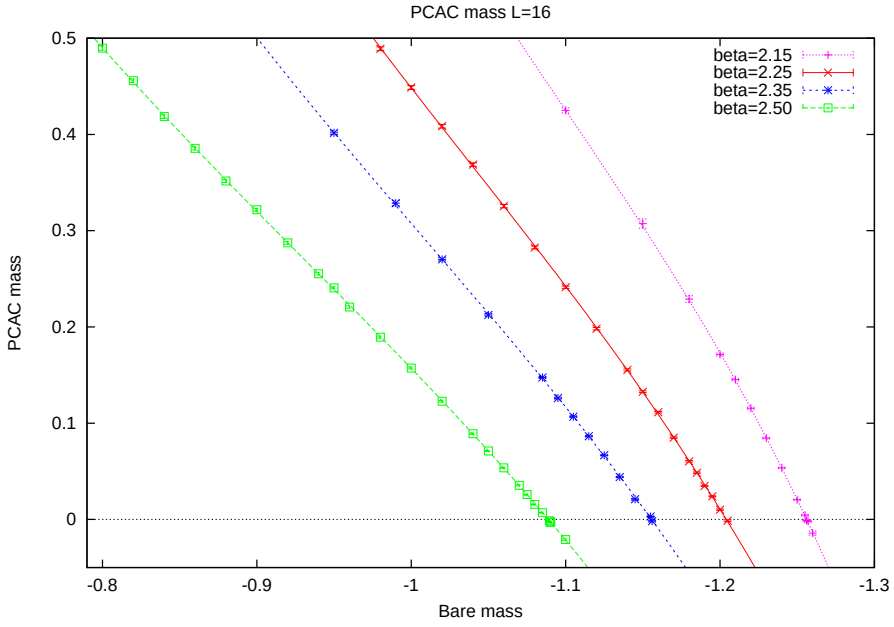

Figure 4.9: PCAC mass as a function of the bare mass on 16^4 lattices for $\beta = 2.15, 2.25, 2.50, 3.00$

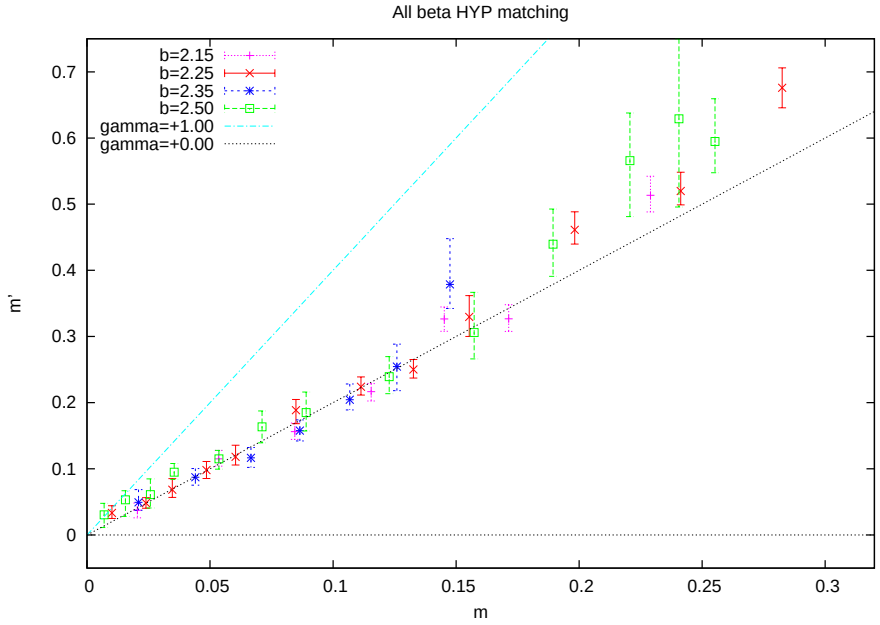

Figure 4.10: HYP matching in mass for $\beta = 2.15, 2.25, 2.35, 2.50$.

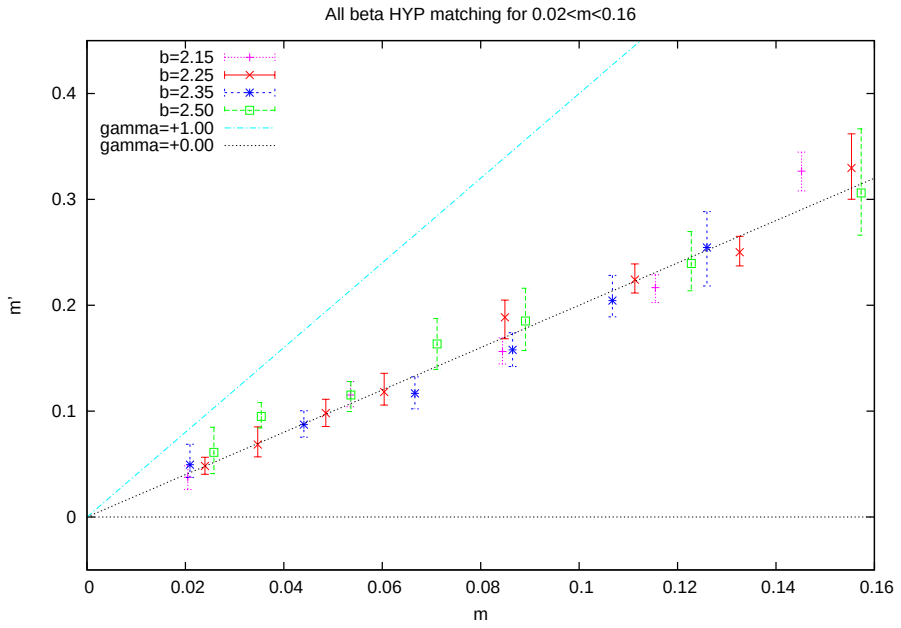

Figure 4.11: HYP Matching in mass using all β values in the mass range $0.02 < m < 0.14$. Consistent with a vanishing anomalous mass dimension, $\gamma = 1$ is strongly disfavoured.

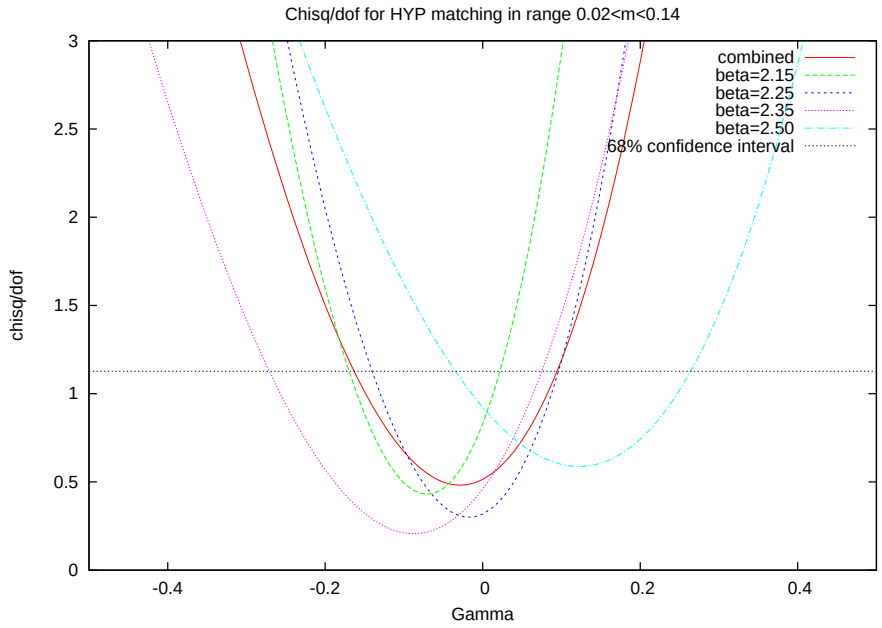

Figure 4.12: $\chi^2/d.o.f$ of γ with HYP Matching in mass using all β values in the mass range $0.02 < m < 0.14$. Combined best fit with 18 $d.o.f$ gives $\gamma = -0.01(13)$.

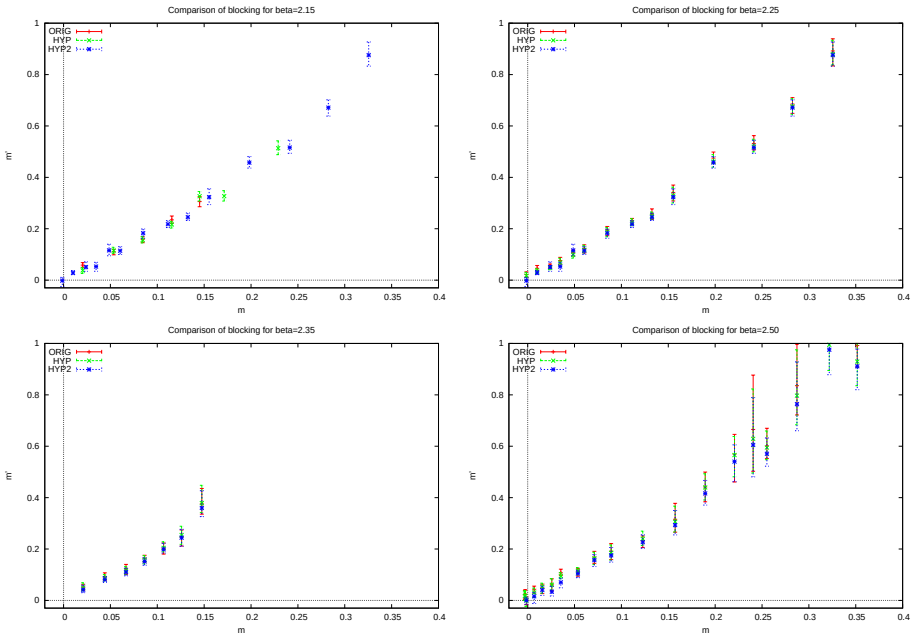

Figure 4.13: Comparison of matching mass pairs using different blocking transforms.

4.5 MWT Results - Coupling

It would also be interesting to directly measure the step scaling of the bare coupling $s_b(\beta, s)$ for the full theory, as was done for the pure gauge case. A fixed point would be indicated by a change of sign in this quantity as the bare coupling is varied from weak to strong coupling. The difficulty is that the mass is a relevant operator, while the coupling is expected to be at best nearly marginal, so in order for the MCRG to pick out the behaviour of the coupling the mass would have to be tuned to zero. Furthermore, even if the mass is tuned sufficiently close to zero that we are initially following the evolution of the gauge coupling (assuming it is the least irrelevant remaining operator), we can no longer take $n \to \infty$ limit, because the coupling will flow to its FP value, and the flow of the mass will eventually dominate.

So the method is to tune the mass close to zero initially, then take a few RG steps, where the flow is hopefully following the gauge coupling, and extract the running of the coupling from this, before the flow in the mass becomes significant.

We measure the PCAC mass on 16^4 lattices for a range of β values at small masses, and for each β extract the critical bare mass using a linear interpolation in the PCAC masses, as shown in Fig. 4.14.

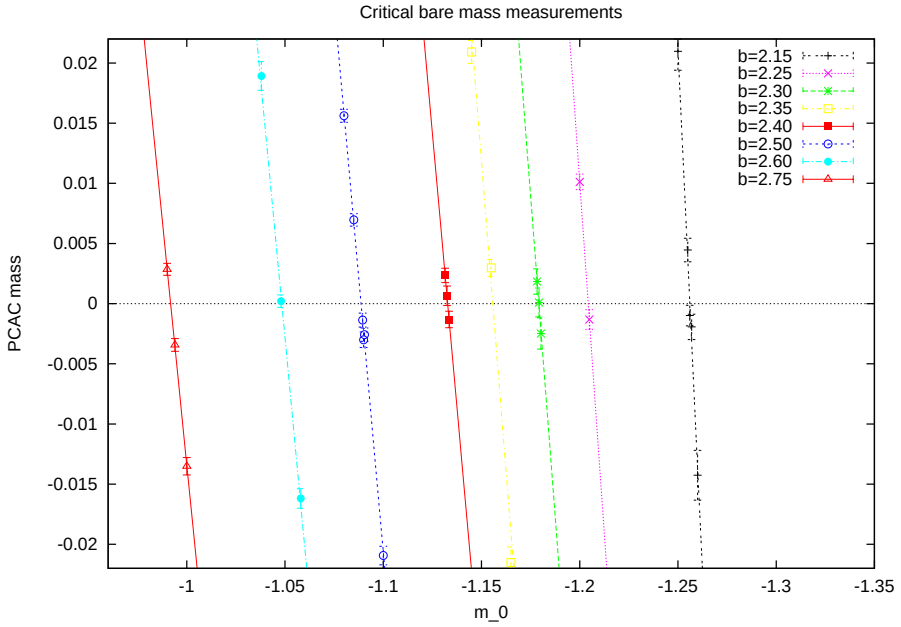

Figure 4.14: Measurement of critical m_0 values from 16^4 lattices.

We then fit an interpolating function in β to these critical masses, as shown in Fig. 4.15, which gives us the critical bare mass for any β in the range $2.15 < \beta < 2.75$. The systematic error in the PCAC mass due to this interpolation is small, < 0.002, as described in Appendix F.4.

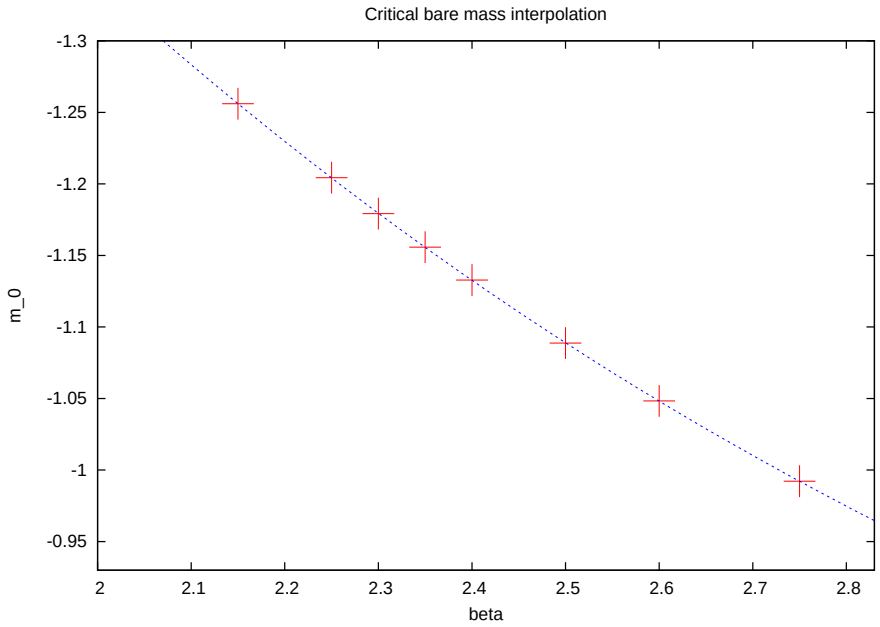

Figure 4.15: Interpolation of critical m_0 values from 16^4 lattices, to be used to determine critical m_0 values for the massless 8^4 runs.

The measured PCAC masses for the 16^4 critical runs are shown in Fig. 4.16, along with some runs at small masses to allow us to check for any systematic mass–dependence.

We generated ~ 3000 configurations on 16^4 and 8^4 lattices for a range of β values, each run at the critical bare mass. The matching procedure in β is then essentially the same as for the pure gauge case. An example of the matching in the plaquette, and subsequent α–optimisation is shown in Fig. 4.17.

The resulting measurement of $s_b(\beta)$ is shown in Fig. 4.18. This includes both the massless and small mass 16^4 runs - within errors s_b shows no mass dependence for these small masses. The ORIG matching values of s_b are clearly positive throughout, the HYP values are lower, and the HYP2 values are consistent with zero within error bars. There is no clear cross–over from positive to negative values of s_b for any of the blocking transforms, so while the data are consistent with a fixed point, they are not sufficiently precise to distinguish slow running

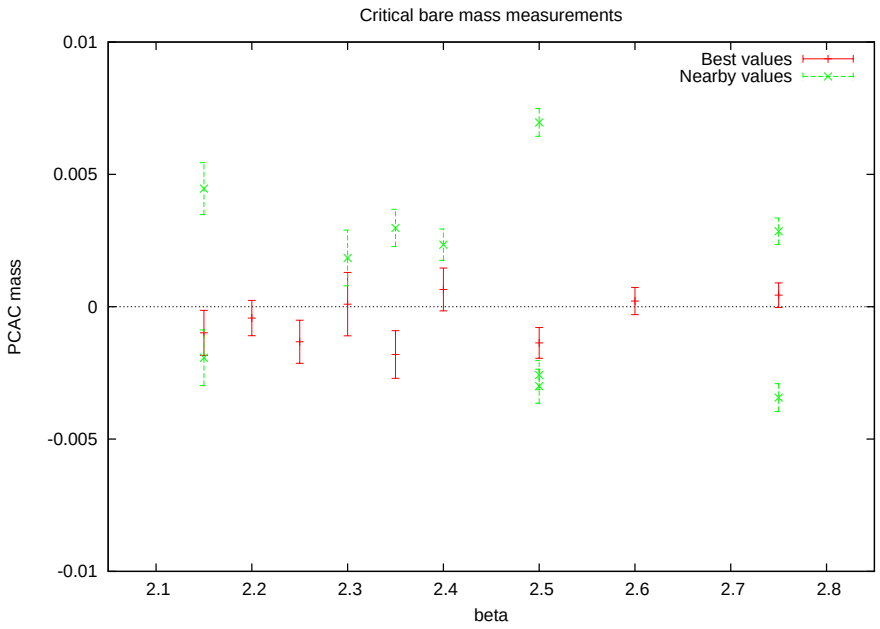

Figure 4.16: Measured PCAC mass of critical 16^4 runs used for massless matching.

from a fixed point.

4.6 Systematics

There are a number of systematic errors in this method which are not yet fully under control, and potentially large. In particular the set of observables used for the matching does not seem sufficiently broad to uniquely identify the matching couplings. Finite volume effects are also likely to be present as the mass is decreased, and it is not clear what effect they will have.

4.6.1 Matching Observables

In principle, for a given (β, m) there should be a unique matching set of couplings (β', m'), for which all blocked observables agree. In this work we have set $\beta = \beta'$ and we were able to find m' such that the blocked observables matched. In practice, however, all of our observables are small Wilson loops, and as such are strongly correlated and have a very similar dependence on β' and m'. This means that we can in fact find a "matching" m' for a range of values of β', which, given that we do not know the correct value of β' to use, significantly increases the

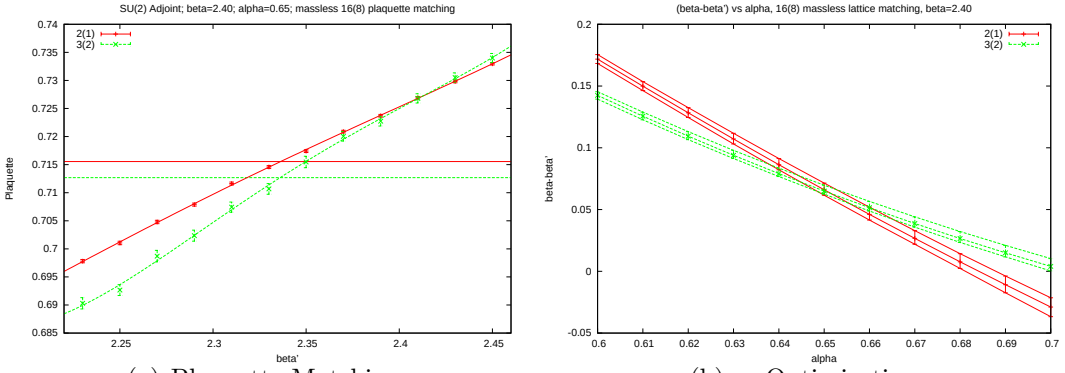

(a) Plaquette Matching (b) α–Optimisation

Figure 4.17: An example of the matching of the plaquette in β' for the massless case using ORIG blocking. This is repeated for each observable to give a systematic error for each matching, then α is varied such that all blocking steps predict the same matching.

error on our determination of γ.

To resolve this issue, more observables which are "orthogonal" to the Wilson loops would need to be included in the matching determination to determine which of these blocked configurations are actually matched.

4.6.2 Finite–Volume

The calculations of γ require us to compute the flow in the mass parameter for a conformal or near–conformal field theory (CFT) in the presence of a small mass deformation. In principle both the mass parameter and the lattice size then determine any correlation length. In order to extract the correct physics for the infinite volume CFT it is important to make sure that the correlation lengths we are measuring and matching are not being strongly influenced by the finite box size. So we should make sure that the physical lattice size is much larger than the correlation length or equivalently $m \gg 1/L$ where L is the lattice length.

Thus we are forced to consider masses that are sufficiently large to satisfy this constraint. Unfortunately, if we use too large a mass we will move the system a long way from any IRFP and the simple MCRG techniques we are using will not apply. The only obvious way to reconcile these two things is to use large enough boxes that we can keep $L \gg 1/m$ while making m small enough to keep us close enough to the CFT fixed point.

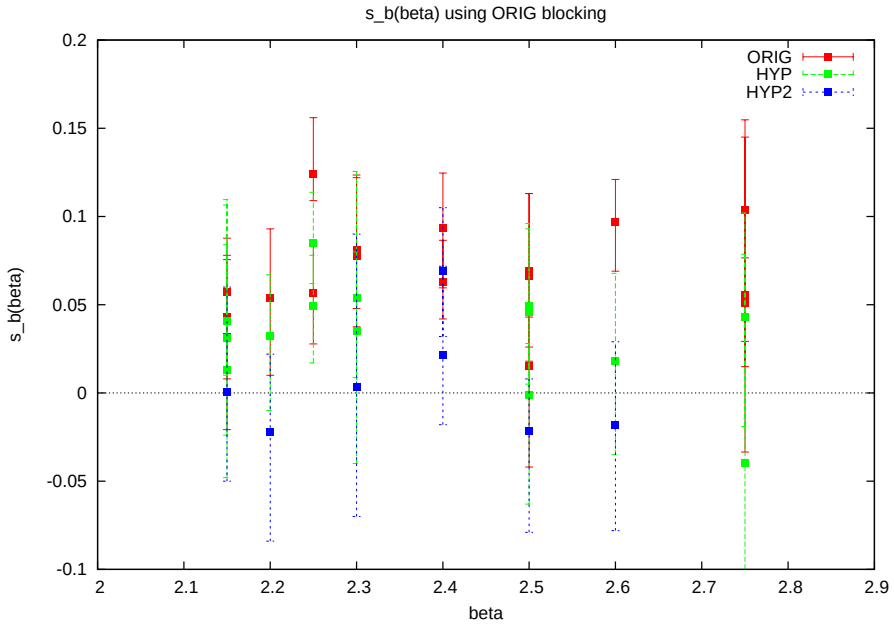

Figure 4.18: Massless matching in β on 16(8) lattices.

For our $L/a = 16$ lattices we would need $ma \gtrsim 0.1$ which may be simply too big to keep close the system close to the fixed point.

4.7 Conclusion

We measure the anomalous mass dimension for Minimal Walking Technicolor and find $\gamma = -0.03(13)$. This is smaller than previous lattice results, and much smaller than would be desired for a phenomenologically viable theory. The error is however likely to be underestimated due to the systematic errors discussed above.

We have also directly measured the running of the coupling to look for a fixed point. Our data show slow running of the coupling and are compatible with a fixed point, but are not sufficently precise to distinguish these two cases.

The systematics of this method are still not fully under control. Using 32^4 lattices would allow a number of improvements. Most importantly they would allow a further RG blocking step to be taken, as well as to check for finite size and finite volume effects in our current results. These larger volume simulations are currently in progress, as are investigations of other possible matching observables to add to the method.

Chapter 5

Conclusion

5.1 Summary

In this thesis I presented some non–perturbative lattice investigations of two candidate walking Technicolor models, Minimal Walking Technicolor - two Dirac fermions in the adjoint representation of SU(2), and Conformal Technicolor - six Dirac fermions in the fundamental representation of SU(2). Two complementary lattice methods were used, the Schrödinger Functional and the 2–lattice matching MCRG method.

5.1.1 Minimal Walking Technicolor

Turning first to the Schrödinger Functional results for Minimal Walking Technicolor, our results for the running of the coupling are completely consistent with those of Ref. [63], and appear to show a slowing in the running of the coupling above $\overline{g}^2 = 2$ or so. They are consistent with the presence of a fixed point where the running stops at somewhat higher $\overline{g}^2$, however once we include the systematic errors from the continuum extrapolation we find that our results no longer give any evidence for a fixed point.

The behaviour of the anomalous dimension γ is much easier to establish. The systematic errors from the continuum extrapolation are much smaller than the signal, and we find a moderate anomalous dimension, close to the 1-loop perturbative prediction, throughout the range of β explored. In particular, in the range $\overline{g}^2 = 2.0 - 3.2$, where there may be an infrared fixed point, we find

$0.05 < \gamma < 0.56$. The error is mostly due to the uncertainty in the location of IRFP.

The same theory was also investigated using the 2–lattice matching MCRG method. We directly measured the running of the coupling to look for a fixed point. Our data show slow running of the coupling and are compatible with a fixed point, but are not sufficently precise to distinguish these two cases.

We also measure the anomalous mass dimension, and with the assumption that the running of the coupling is negligible, our result $\gamma = -0.03(13)$ is consistent with a vanishing anomalous mass dimension. This assumption introduces a potentially large systematic error to our results, however. Without this assumption, the set of matching observables we use are not sufficiently broad to uniquely identify the correct matching coupling, which means we can get a large variation in our measurement of the anomalous mass dimension by varying the matching coupling. So the true error on the quoted value is likely to be larger once the systematic errors are better understood.

Both the Schrödinger Functional and the MCRG results suggest that Minimal Walking Technicolor has an IRFP, with a small anomalous dimension at the IRFP. While neither set of results are conclusive on their own, they are in agreement with a growing body of non–perturbative studies of this theory, so that it seems likely that the theory does in fact have an IRFP, but with an anomalous mass dimension smaller than would be required for the construction of a phenomenologically viable theory.

5.1.2 Conformal Technicolor

Measuring the running of the coupling for six Dirac fermions in the fundamental representation of SU(2) using the Schrödinger Functional method suffers from the same issues as two Dirac fermions in the adjoint representation of SU(2) did. We observe that the running of the coupling is slower than the (already slow) one-loop perturbative prediction. Our results are consistent with the presence of a fixed point above $\overline{g}^2 = 4.02$, but it is also possible that there is no fixed point in the range of couplings we have measured. We have not been able to perform a linear continuum extrapolation for the coupling, which introduces an additional uncertainty.

Once again the results for the running of the mass are clearer. We find

the anomalous dimension is small throughout most of the range of couplings we measure, but it becomes larger for our strongest couplings, with a possibility that it reaches values around 1. If true, this would be very interesting for technicolor models, but the uncertainty in the location or existence of an IRFP remains the limiting factor in constraining the value of the anomalous mass dimension.

This is the first non–perturbative investigation of this theory, unlike the case of Minimal Walking Technicolor. Our results are consistent with the existence of an IRFP, with a potentially large anomalous dimension, so pending further studies this theory remains a viable Technicolor candidate.

5.1.3 Lattice Methods

The Schrödinger Functional method has the advantage that the systematic errors are understood and under control, allowing an extrapolation to the continuum limit of measured quantities. The disadvantage of the method is that measuring the running of the coupling is a very difficult problem. This is due to the difficulty of measuring the small difference in the coupling between two nearby scales, a problem that becomes particularly acute as we approach a possible fixed point where the difference falls. The observable is also noisy and so requires very high statistics to determine it sufficiently accurately, increasing the cost of simulations. The measurement of the anomalous mass dimension on the other hand is much more tractable, and the final uncertainty on the measured value is largely due to the difficulty of determining the location of the IRFP in the coupling.

Thus to improve our results using this method, larger lattices than the ones used in these studies would be required, as well an improved action to remove the $\mathcal{O}(a)$ finite size effects, such as the chirally improved formulation [113, 114], or the formulation with clover improvement [115, 116, 117]. This would allow us to take the continuum limit and distinguish a fixed point from merely very slow running. This would help to clarify the existence and location of the fixed point, and would significantly reduce the errors on the anomalous dimension.

The MCRG method on the other hand allows a determination of the mass anomalous dimension with significantly less computational resources, in principle without having to measure the running of the coupling directly, and the value found has a small statistical uncertainty. The disadvantage of this method is that the systematic errors are less well understood. In particular, the current set

of matching observables are not sufficiently broad to uniquely identify matched actions, which leads to a systematic uncertainty due to a lack of knowledge of the running of the coupling. In addition the finite volume effects in this method are not fully understood.

For both the Technicolor models investigated the running of the coupling was found to be slow, but it was not possible to distinguish merely slow running from a fixed point. In the Schrödinger Functional simulations this is largely due to the difficulty in taking the continuum limit, whilst in the MCRG method the matching couplings predicted by different operators had a significant spread, leading to a large error on the final values.

The measurement of the anomalous mass dimension is much more tractable in both methods. In the Schrödinger Functional the continuum limit can be taken, and in the MCRG method the matching mass pairs predicted by different operators are very close, leading to small errors on the measured matching masses. However in both methods the limiting factor in the determination of the anomalous dimension remains the determination of the location of the IRFP in the coupling.

5.2 Outlook

Lattice studies are providing vital information for the building and testing of walking Technicolor models, which should be experimentally tested over the next few years at the LHC. Minimal Walking Technicolor has been investigated in a number of studies, all of which found results compatible with the theory containing an IRFP, but with an anomalous mass dimension that is too small for the theory to be phenomenologically viable. The candidate Conformal Technicolor theory investigated in this thesis on the other hand may yet be phenomenologically viable, as a large anomalous mass dimension was not excluded by our results, pending further studies of this theory.

Future Schrödinger Functional studies should be able to unambiguously determine the running of the coupling and the mass in these theories. To achieve this, larger lattices with an improved action are required to remove the $\mathcal{O}(a)$ effects and allow the continuum limit to be taken. A recent clover–improved lattice result [64] for MWT found a small value for the mass anomalous dimension,

consistent with our value, but taking the continuum limit remains a very difficult problem.

The MCRG method is a potentially valuable alternative method, and studies are in progress using larger lattices which will provide a better understanding of the systematic errors involved. Other MCRG methods, in addition to the 2–lattice matching method, are also being investigated, as well as potential additional matching observables to improve the 2–lattice matching method.

Ultimately however, all these techniques were developed for QCD and have been adapted to investigate these very different theories, and it seems unlikely that they are the most effective tools for this task. It may be that new techniques can be developed which are better suited to the task.

Appendix A

Scheme Dependence

A.1 Conformal Behaviour

A.1.1 Beta Function

The running of the coupling in a massless renormalisation scheme is defined by the beta function

$$\mu\frac{d\overline{g}}{d\mu} = \beta(\overline{g}). \tag{A.1}$$

A zero of the beta function in our scheme at some $\overline{g}^2 = u^*$ implies a fixed point in the theory. If we change to a different scheme, does the zero still exist, or could it just be a scheme-dependent artefact? For another arbitrary scheme X there will exist a function f such that

$$\overline{g}_X = f[\overline{g}]. \tag{A.2}$$

Using this we can relate the beta functions in two different schemes

$$\mu\frac{d\overline{g}_X}{d\mu} = \beta_X(\overline{g}_X) \tag{A.3}$$

$$\Rightarrow \beta_X(f[\overline{g}]) = \mu\frac{d\left(f[\overline{g}]\right)}{d\mu} = \mu\frac{df}{d\overline{g}}\frac{d\overline{g}}{d\mu} \tag{A.4}$$

$$\Rightarrow \beta_X(f[\overline{g}]) = \frac{df}{d\overline{g}}\beta(\overline{g}) \tag{A.5}$$

So assuming f is non-singular, a zero in the beta function of a scheme implies

the existence of the zero in all schemes.

A.1.2 Coupling Step Scaling

In the SF-scheme we don't directly measure β, instead we measure the step scaling function for the coupling

$$\sigma(s,u) = \overline{g}^2(sL)|_{\overline{g}^2(L)=u}. \tag{A.6}$$

Again there will exist some function $F[x] \equiv (f[x])^2$ such that

$$\overline{g}^2_X = F[\overline{g}^2]. \tag{A.7}$$

This can be used to relate the step scaling functions in different schemes

$$\begin{aligned} \sigma_X(s,u') &= \overline{g}^2_X(2L)|_{\left\{\overline{g}^2_X(L)=u'\right\}} \\ &= \overline{g}^2_X(2L)|_{\left\{\overline{g}^2(L)=F^{-1}[u']\right\}} \\ &= F\left[\overline{g}^2(2L)|_{\left\{\overline{g}^2(L)=F^{-1}[u']\right\}}\right] \\ &= F\left[\sigma(s,F^{-1}[u'])\right] \end{aligned} \tag{A.8}$$

A zero of the beta function in our scheme means that for some u^* we find

$$\sigma(s,u^*) = u^* \tag{A.9}$$

Does this zero exist in other schemes, or is it just a scheme-dependent artefact? Using the above relation, and choosing $u' = F[u^*]$ gives

$$\sigma_X(s,F[u^*]) = F[\sigma(s,F^{-1}[F[u^*]] = F[\sigma(s,u^*)] = F[u^*] \tag{A.10}$$

$$\Rightarrow \sigma_X(s,u') = u' \tag{A.11}$$

So we find the same scale invariant behaviour, regardless of the actual form of F (assuming F is not singular), and the zero exists in all renormalisation schemes.

A.1.3 Gamma Function

The running of the mass is given by

$$\mu\frac{d\overline{m}}{d\mu} = \gamma(\overline{g})\overline{m} \Rightarrow \gamma(\overline{g}) = \frac{d\ln|\overline{m}|}{d\ln|\mu|}. \tag{A.12}$$

A change of scheme will be defined by some function h such that $\overline{m}_X = h[\overline{g}]\overline{m}$, which we can use to relate γ in different schemes:

$$\gamma_X(\overline{g}_X) = \gamma_X(f[\overline{g}]) = \frac{d\ln|\overline{m}_X|}{d\ln|\mu|} = \frac{d\ln|h[\overline{g}]\overline{m}|}{d\ln|\mu|} = \gamma(\overline{g}) + \frac{\mu}{h[\overline{g}]}\frac{dh}{d\overline{g}}\frac{d\overline{g}}{d\mu}. \tag{A.13}$$

Substituting $\mu\frac{d\overline{g}}{d\mu} = \beta(\overline{g})$ gives

$$\gamma_X(f[\overline{g}]) = \gamma(\overline{g}) + \frac{d\ln|h[\overline{g}]|}{d\overline{g}}\beta(\overline{g}) \tag{A.14}$$

So at a fixed point where $\beta = 0$, γ is the same in all schemes.

A.1.4 Mass Step Scaling

In the SF scheme we measure the mass step scaling function

$$\sigma_P(u,s) = \left.\frac{Z_P(sL)}{Z_P(L)}\right|_{\overline{g}^2(L)=u} = \left.\frac{\overline{m}(L)}{\overline{m}(sL)}\right|_{\overline{g}^2(L)=u}. \tag{A.15}$$

This can be related to the same function in a different scheme:

$$\sigma_{PX}(F[u],s) = \left.\frac{\overline{m}_X(L)}{\overline{m}_X(sL)}\right|_{\overline{g}_X^2(L)=F[u]} = \left.\frac{\overline{m}(L)}{\overline{m}(sL)}\frac{h[\overline{g}(L)]}{h[\overline{g}(sL)]}\right|_{\overline{g}^2(L)=u} \tag{A.16}$$

$$\Rightarrow \sigma_{PX}(F[u],s) = \sigma_P(u,s)\frac{h[\overline{g}(sL)+\Delta\overline{g}]}{h[\overline{g}(sL)]} \tag{A.17}$$

where

$$\Delta\overline{g} = \int_{1/sL}^{1/L} -\beta d\ln|L|. \tag{A.18}$$

So if $\beta = 0$, then the step scaling function is that same in all schemes. Since in this case γ is constant, we can integrate the evolution equation

$$\int \gamma d\ln|\mu| = \int d\ln|\overline{m}| \Rightarrow \overline{m} \sim \left(\frac{1}{L}\right)^{\gamma}, \tag{A.19}$$

and we can relate the anomalous dimension to the step scaling function

$$\sigma_P(u,s) = \frac{(1/L)^{\gamma}}{(1/sL)^{\gamma}} = s^{-\gamma}. \tag{A.20}$$

A.2 Near-Conformal Behaviour

A.2.1 Beta Function

Technicolour models require a walking coupling, where the coupling is almost constant over a large range of scales. This translates to a small but non-zero beta function. Assuming the beta function is small, $\beta(\overline{g}) = \Delta_\beta$, when we change scheme

$$\beta_X(\overline{g}_X) = \beta_X(f[\overline{g}]) = \frac{df}{d\overline{g}}\beta(\overline{g}) = \frac{df}{d\overline{g}}\Delta_\beta. \tag{A.21}$$

But $\frac{df}{d\overline{g}}$ could be anything, so the beta function can be deformed at will by changing scheme, and the presence of a zero is the only scheme-independent feature. In particular the smallness of the beta function is not scheme independent.

A.2.2 Coupling Step Scaling

The step scaling function for a walking coupling will be of the form

$$\sigma(s,u^*) = u^* + \Delta, \tag{A.22}$$

where Δ is small. In our X–scheme choosing $u' = F[u^*]$ we find

$$\sigma_X(s,F[u^*]) = F[\sigma(s,u^*)] = F[u^* + \Delta]. \tag{A.23}$$

Expanding the RHS in powers of Δ

$$F[u^* + \Delta] = F[u^*] + \Delta \left.\frac{dF[u]}{du}\right|_{u=u^*} + O(\Delta^2) \tag{A.24}$$

$$\Rightarrow \sigma_X(s, u') = u' + \Delta \left.\frac{dF[u]}{du}\right|_{u=u^*} + O(\Delta^2). \tag{A.25}$$

Again $\frac{dF[u]}{du}$ could be anything - so near-conformal behaviour is scheme-dependent, and with a suitable choice of F, the coupling can be made to have any non-constant, monotonic scale dependence.

A.2.3 Gamma Function

Assuming the beta function is small, $\beta(\overline{g}) = \Delta_\beta$, when we change scheme

$$\gamma_X(f[\overline{g}]) = \gamma(\overline{g}) + \frac{d\ln|h[\overline{g}]|}{d\overline{g}}\Delta_\beta. \tag{A.26}$$

But since $\frac{d\ln|h[\overline{g}]|}{d\overline{g}}$ could be anything, then γ_X could be drastically different from γ even if β is very small.

A.2.4 Mass Step Scaling

For small beta, $\beta(\overline{g}) = \Delta_\beta$, the mass step scaling function can be related to the same function in a different scheme,

$$\sigma_{PX}(F[u], s) = \sigma_P(u, s)\frac{h[\overline{g}(sL) + \Delta\overline{g}]}{h[\overline{g}(sL)]}, \tag{A.27}$$

where

$$\Delta\overline{g} = \int_{1/sL}^{1/L} -\beta d\ln|L| \approx -\Delta_\beta \ln|s|. \tag{A.28}$$

Expanding h about $\overline{g}(L)$ gives

$$h[\overline{g}(sL)] = h[\overline{g}(L)] + \left(\left.\frac{dh}{dg}\right|_{\overline{g}^2(L)=u}\right)\Delta_\beta \ln|s| + O(\Delta_\beta^2). \tag{A.29}$$

Inserting this into the expression for the step scaling gives

$$\sigma_{PX}(F[u], s) = \sigma_p(u, s) \left[1 - \left. \frac{d \ln |h|}{dg} \right|_{\bar{g}^2 = u} + O(\Delta_\beta^2) \right] . \tag{A.30}$$

But again $\frac{d \ln |h|}{dg}$ could be anything, so the mass step scaling function could change drastically between schemes, even if the beta function is very small.

Appendix B

Error Analysis SF MWT

B.1 Coupling error analysis

We directly measure the Schrödinger Functional coupling $\overline{g}^2$ and perform multiple stages of interpolation and extrapolation to extract the continuum step scaling function $\sigma(u) \equiv \sigma(u, 4/3)$.

In order to estimate our errors for each of these stages we perform multiple bootstraps of the data. The full procedure to get a single estimate of $\sigma(u)$ can be summarised as follows:

- Generate $N_b \times N_a$ bootstrapped ensembles of the data and extract mean and error for each. Blocks of N_a ensembles are used to give interpolated data points with error bars, so from $N_b \times N_a$ bootstrapped ensembles N_a interpolated data points are generated, each with an associated error bar.
- For each bootstrap, interpolate in a/L to find values at $L = 9, 10\frac{2}{3}$.
- From each set of N_a of these find the mean and standard deviation, to give N_b interpolated data points with error bars.
- For each of the N_b bootstraps do a non-linear least squares fit for $\overline{g}^2(\beta, L)$ interpolation functions in β, an example is shown in Fig. B.1.
- Use these functions to find N_b estimates of $\Sigma(a/L, u)$ for $L = 8, 9$, and from this extract a mean and error for each a/L.

- Perform a single weighted continuum extrapolation in a/L using these points to give $\sigma(u)$.

This process is repeated N_m times, bringing the total number of bootstrap replicas of the data to $N_a \times N_b \times N_m$. This gives N_m estimates of $\sigma(u)$, from which a mean and 1-sigma confidence interval is extracted.

However, the systematic errors that result from varying the number of parameters in the interpolation functions or the continuum extrapolation functions are significantly larger than the statistical errors for the optimal set of parameters.

In order to quantify this, we repeated the entire bootstrapped process of calculating $\sigma(u)$ with a range of different interpolation and extrapolation functions, each of which gives an estimate for $\sigma(u)$, with an associated statistical error.

Specifically, we included two different choices for the number of parameters in the interpolating functions at each L. We kept the best fit, outlined in Tab. B.1 and added the function with the second lowest χ^2 per degree of freedom as shown in Tab. B.2. The error in the continuum extrapolation was estimated by including both constant and linear extrapolation functions. All possible combinations of these functions gave us a set of $2^5 = 32$ values for $\sigma(u)$, each with a statistical error, which spanned the range of the systematic variation.

For each value of u the resulting extremal values of $\sigma(u)$ were used as upper and lower bounds on the central value.

B.2 Mass error analysis

The mass error analysis follows the same procedure as outlined in Appendix B.1 with $\overline{g}^2$ replaced by Z_P. The function used to interpolate Z_P in β is

$$Z_P(\beta, L/a) = \sum_{i=0}^{n} c_i \left(\frac{1}{\beta}\right)^i \tag{B.1}$$

as given in Eq. 3.27, and an example fit is shown in Fig. B.2. The c_i giving the smallest reduced χ^2 are given in Tab. B.3 and those with the second smallest in Tab. B.4.

In addition, Z_P converges faster than $\overline{g}^2$ and we have better 16^4 data so we can use 3 points in our continuum extrapolations. Again the $L = 6$ data were

found to have large $O(a)$ artifacts so are not used in the continuum extrapolation, and for the constant extrapolation only the two points closest to the continuum limit are used. The fits for both $\overline{g}^2$ and Z_P are required to determine $\sigma_P(u)$, so independently varying the choice of the number of parameters for these now gives $2^{10} = 1024$ values for $\sigma_P(u)$, each with a statistical error.

$\overline{g}^2$	L/a				
	6	8	9	$10\frac{2}{3}$	12
c_0	1.113 ± 0.057	0.967 ± 0.050	1.010 ± 0.001	0.987 ± 0.003	0.988 ± 0.024
c_1	-0.560 ± 0.206	-0.064 ± 0.215	-0.259 ± 0.001	-0.216 ± 0.006	-0.226 ± 0.055
c_2	0.130 ± 0.216	-0.307 ± 0.328		-0.022 ± 0.003	-0.016 ± 0.028
c_3	0.366 ± 0.125	0.221 ± 0.211			
c_4	-0.136 ± 0.196	-0.059 ± 0.048			
c_5	-0.364 ± 0.234				
c_6	0.298 ± 0.127				
c_7	-0.064 ± 0.024				
$\frac{\chi^2}{dof}$	2.85	2.42	1.73	3.45	3.37
dof	8	7	4	3	4

Table B.1: Interpolation best fit parameters for $\overline{g}^2$.

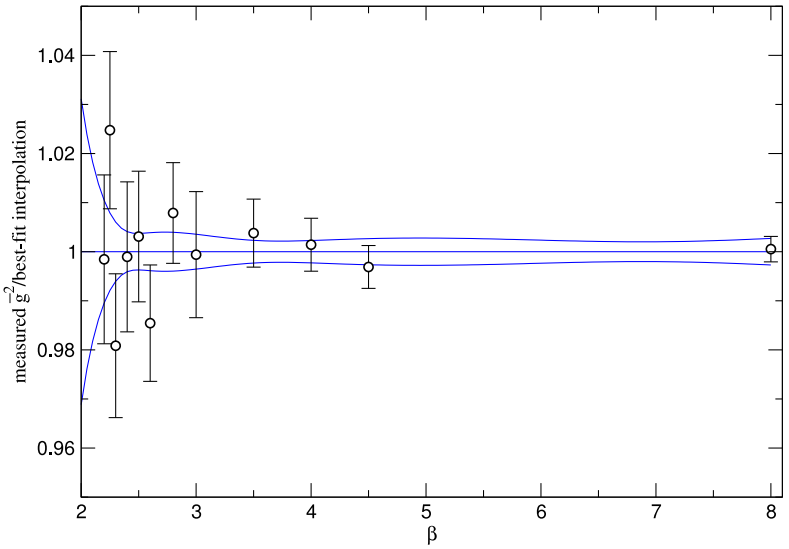

Figure B.1: Example of an interpolation function for $L = 8$, with a $\pm\sigma$ confidence interval, compared with measured $\overline{g}^2$ data points.

$\overline{g}^2$	L/a				
	6	8	9	$10\frac{2}{3}$	12
c_0	1.113 ± 0.057	0.967 ± 0.050	1.010 ± 0.001	0.987 ± 0.003	0.988 ± 0.024
c_1	-0.560 ± 0.206	-0.064 ± 0.215	-0.259 ± 0.001	-0.216 ± 0.006	-0.226 ± 0.055
c_2	0.130 ± 0.216	-0.307 ± 0.328		-0.022 ± 0.003	-0.016 ± 0.028
c_3	0.366 ± 0.125	0.221 ± 0.211			
c_4	-0.136 ± 0.196	-0.059 ± 0.048			
c_5	-0.364 ± 0.234				
c_6	0.298 ± 0.127				
c_7	-0.064 ± 0.024				
$\frac{\chi^2}{dof}$	2.85	2.42	1.73	3.45	3.37
dof	8	7	4	3	4

Table B.2: Interpolation next-best fit parameters for $\overline{g}^2$.

Z_P	L/a					
	6	8	9	$10\frac{2}{3}$	12	16
c_0	0.58 ± 0.30	0.93 ± 0.09	1.02 ± 0.01	1.00 ± 0.01	1.01 ± 0.01	1.01 ± 0.01
c_1	7.64 ± 6.85	-0.43 ± 1.74	-2.17 ± 0.10	-1.76 ± 0.01	-1.98 ± 0.08	-1.99 ± 0.09
c_2	-78.87 ± 60.50	-8.18 ± 12.64	4.70 ± 0.54	1.56 ± 0.05	2.30 ± 0.31	1.93 ± 0.43
c_3	361.79 ± 272.14	36.42 ± 43.33	-10.73 ± 1.27	-2.14 ± 0.06	-3.01 ± 0.34	-2.23 ± 0.64
c_4	-898.23 ± 662.83	-75.69 ± 71.04	7.96 ± 1.06			
c_5	1137.79 ± 833.32	57.07 ± 44.83				
c_6	-579.79 ± 424.25					
$\frac{\chi^2}{dof}$	2.42	1.66	2.24	4.82	6.68	6.67
dof	11	8	5	6	6	3

Table B.3: Interpolation best fit parameters for Z_P.

Z_P	L/a					
	6	8	9	$10\frac{2}{3}$	12	16
c_0	1.00 ± 0.07	1.14 ± 0.46	0.89 ± 0.02	1.00 ± 0.01	0.97 ± 0.03	0.99 ± 0.01
c_1	-1.85 ± 1.34	-5.14 ± 10.46	0.53 ± 0.40	-1.76 ± 0.14	-1.33 ± 0.46	-1.73 ± 0.03
c_2	5.09 ± 9.46	34.05 ± 93.82	-15.14 ± 2.87	1.60 ± 0.84	-1.40 ± 2.60	0.48 ± 0.08
c_3	-14.99 ± 31.38	-157.82 ± 428.42	58.03 ± 9.82	-2.22 ± 1.97	5.68 ± 6.05	
c_4	17.1 ± 49.72	405.88 ± 1059.89	-105.52 ± 15.92	0.07 ± 1.62	-7.18 ± 5.00	
c_5	-7.82 ± 30.32	-558.73 ± 1353.59	71.97 ± 9.92			
c_6		318.7 ± 700.1				
$\frac{\chi^2}{dof}$	2.46	1.75	2.32	5.97	7.47	8.03
dof	12	7	4	5	5	4

Table B.4: Interpolation next-best fit parameters for Z_P.

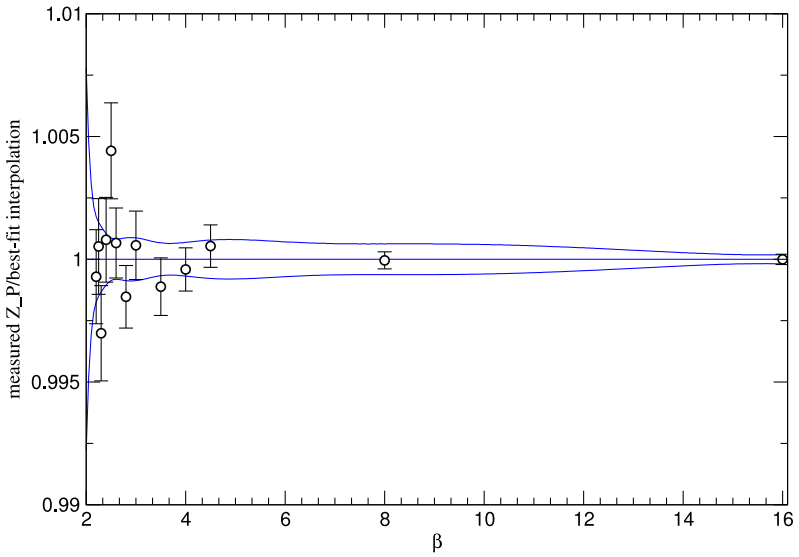

Figure B.2: Example of an interpolation function for $L = 8$, with a $\pm\sigma$ confidence interval, compared with measured Z_P data points.

Appendix C

SF Implementation

C.1 HiRep Modifications

HiRep [54] is an implementation of the RHMC algorithm [90] for gauge theories with any number of flavours and colours, and in a variety of representations of the gauge group, as described in Sec. 2.4.

The key modifications required to implement the Schrodinger Functional in HiRep are as follows:

- The fermionic boundary conditions defined in Eq. 3.6 are enforced both before and after the Dirac operator is applied.
- The gauge fields on the boundary are initially set to the background fields defined in Eq. 3.5.
- When the gauge fields are updated, or randomised, the fields on the boundary are not updated. (And their momenta remain zero throughout - or equivalently the boundary fields are missed out in all updates and their momenta are not included in the p^2 term in the action).
- The trial spinor used in the inversion code must obey the fermionic boundary conditions in Eq. 3.6 to avoid the zero modes of the Dirac operator in this formulation.
- The gauge observables used to calculate $\overline{g}^2$ as defined in Eq. 3.11 are added.

- The fermionic correlators f_P, f_A, f_1 used to calculate the PCAC mass described in Sec. 3.1.3 and the pseudoscalar fermion bilinear Z_P described in Sec. 3.1.4 are added.

C.2 Avoiding the Zero Modes

Upon applying the fermion boundary conditions the RHMC code fails when it tries to invert the H2 operator, which takes an input spinor and gives an output spinor, such that

$$\langle \psi_{in} | \psi_{out} \rangle = \langle \psi_{in} | H^2 | \psi_{in} \rangle = \langle H^2 \rangle, \tag{C.1}$$

where H is the hermitian Dirac operator

$$H = \gamma_5 D \tag{C.2}$$

and D is the Wilson–Dirac operator defined in Eq. 2.32.

This is because the Dirac operator, and hence H^2, has zero modes caused by the boundary conditions. For example consider an input spinor with non-zero components only for the left handed components on the $T = 0$ boundary, applying the boundary conditions gives a null spinor, i.e. a zero mode. The solution is to work in the subspace orthogonal to these zero modes of the operator.

Define $v_\alpha^{(n)}(x) = \delta_{x,x'}\delta_{\alpha,\alpha'}$, where x', α' lie on the boundary such that $\psi_{\alpha'}(x') = 0$ due to the boundary conditions, so that $n = 1, 2, \ldots, 4L^3$. [(2 time slices)*(2 spinor indices)*(L^3 spatial values)]. Then all the zero-mode components of a trial spinor ψ can be subtracted:

$$\psi_\alpha(x) \to \psi_\alpha(x) - \sum_n \langle \psi_\alpha(x) | v_\alpha^{(n)}(x) \rangle v_\alpha^{(n)}(x) \tag{C.3}$$

This is easy to implement, as it is equivalent to simply applying the fermionic boundary conditions of Eq. 3.6 to the trial solution.

Given an initial solution which lies within the orthogonal subspace, further iterations will remain in the subspace since any components outside it will be set to zero by the boundary conditions being applied before and after the Dirac operator.

C.3 Point Source PCAC Mass

The Dirac operator is inverted for a given source

$$D_{ab\alpha\beta}(x,y)\psi_{b\beta}^{(a_0)(\alpha_0)}(y) = \delta_{a,a_0}\delta_{\alpha,\alpha_0}\delta_{x,x_0} \tag{C.4}$$

for fixed a_0, α_0, x_0, where the upper indices in brackets are labels. This gives a $(VOL) \times 4D_R$ component complex vector

$$\psi_{b\beta}^{(a_0)(\alpha_0)}(y) = S_{ba_0\beta\alpha_0}(y,x_0) \tag{C.5}$$

The full propagator is formed from combining $4D_R$ of these into a matrix, one for each possible combination of α_0, a_0. We now have the propagator from all points y to this point x_0, which for each y is a $4D_R \times 4D_R$ complex matrix:

$$S_{ba\beta\alpha}(y,x_0) = \left[\begin{pmatrix} & & \\ S_{b0\beta0}(y,x_0) & & \\ & & \end{pmatrix} \begin{pmatrix} & & \\ S_{b1\beta0}(y,x_0) & & \\ & & \end{pmatrix} \ \ldots \ \begin{pmatrix} & & \\ S_{bD_R\beta3}(y,x_0) & & \\ & & \end{pmatrix} \right]$$

Due to the fermionic boundary conditions we cannot directly find the propagator to the boundary from a point in the bulk, but we can get the propagator to the site adjacent to the boundary. The propagators from the boundary to bulk can then be written in terms of these propagators from the point $x_0 = a$ to the bulk [118]:

$$\left[\zeta(x)\overline{\psi}(y)\right]_F = P_- U_{x-a\hat{0},0} S(x,y)|_{x_0=a} \tag{C.6}$$

$$\left[\zeta'(x)\overline{\psi}(y)\right]_F = P_+ U^\dagger_{x,0} S(x,y)|_{x_0=L-a} \tag{C.7}$$

$$\left\{\left[\psi(x)\overline{\zeta}(z)\right]_F\right\}^\dagger = \gamma_5 \left[\zeta(z)\overline{\psi}(x)\right]_F \gamma_5 \tag{C.8}$$

Substituting these definitions we get

$$f_P(x_0) = \frac{a^6}{2}\sum_{y,z}\left\langle \mathrm{Tr}\left\{P_- U_{z-a\hat{0},0} S(z,x)\gamma_5 \left[\gamma_5 P_- U_{y-a\hat{0},0} S(y,x)\gamma_5\right]^\dagger \gamma_5\right\}\right\rangle_G$$

$$= \frac{a^6}{2}\sum_{y,z}\left\langle \mathrm{Tr}\left\{P_- U_{z-a\hat{0},0} S(z,x)\left[P_- U_{y-a\hat{0},0} S(y,x)\right]^\dagger\right\}\right\rangle_G \quad \text{(C.9)}$$

$$f_A(x_0) = \frac{a^6}{2}\sum_{y,z}\left\langle \mathrm{Tr}\left\{P_- U_{z-a\hat{0},0} S(z,x)\gamma_0\left[P_- U_{y-a\hat{0},0} S(y,x)\right]^\dagger\right\}\right\rangle_G \quad \text{(C.10)}$$

where x is a fixed point in the centre of the lattice, and y, z are now summed over the constant time slice $y_0 = a$ and $z_0 = a$.

Similar expressions are obtained for the correlators from the other boundary:

$$f'_P(x_0) = \frac{a^6}{2}\sum_{y,z}\left\langle \mathrm{Tr}\left\{P_+ U^\dagger_{z,0} S(z,x)\left[P_+ U^\dagger_{y,0} S(y,x)\right]^\dagger\right\}\right\rangle_G \quad \text{(C.11)}$$

$$f'_A(x_0) = -\frac{a^6}{2}\sum_{y,z}\left\langle \mathrm{Tr}\left\{P_+ U^\dagger_{z,0} S(z,x)\gamma_0\left[P_+ U^\dagger_{y,0} S(y,x)\right]^\dagger\right\}\right\rangle_G \quad \text{(C.12)}$$

where x is a fixed point in the centre of the lattice, but y, z are now summed over the constant time slice $y_0 = L - a$ and $z_0 = L - a$.

Finally the trace is a sum of these dot products, if we have two propagators $S(x,y), S(z,x)$ for fixed points x, y, z, which are composed of a set of vectors $\psi^{(a)(\alpha)}$ and $\phi^{(b)(\beta)}$ respectively, then

$$\mathrm{Tr}\left[S(x,y)S(z,y)^\dagger\right] = \sum_{\alpha,\beta,a,b}\psi^{(\alpha)(a)}.\phi^{(\beta)(b)}\delta_{ab}\delta_{\alpha\beta} \quad \text{(C.13)}$$

$$\mathrm{Tr}\left[S(x,y)\gamma^0 S(z,y)^\dagger\right] = \sum_{\alpha,\beta,a,b}\psi^{(\alpha)(a)}.\phi^{(\beta)(b)}\delta_{ab} f_{\alpha\beta} \quad \text{(C.14)}$$

where

$$f_{\alpha\beta} = \begin{cases} -1 & \text{for} \quad (\alpha,\beta) = (2,0),(3,1),(0,2),(1,3) \\ 0 & \text{otherwise} \end{cases}$$

This method requires inverting a point source at $x_0 - 1, x_0, x_0 + 1$, so $3 \times (4N_F)$ inversions for both m_{pos} and m_{neg}. It only calculates the PCAC mass for a single point in the bulk, so while it is useful for testing the code, in practice the PCAC mass for a spatially averaged wall source is used.

C.4 Wall Source PCAC Mass

The point source implementation of the PCAC mass finds the propagator from a point in the middle to all points, then applies a projection and multiplies by a gauge link. The resulting correlators are averaged over all spatial points on the boundary. This gives both pos and neg PCAC masses with $3 \times (4N_F)$ inversions.

An alternative implementation is to use a wall source (a point source at all spatial points on a timeslice) at the timeslice adjacent to the boundary, which already has a projection and gauge link applied. Then the propagator to all interior points is calculated directly, and correlators are averaged over all spatial points for each timeslice. The advantages of this method are that it only requires $2 \times (4N_F)$ inversions (one for each boundary), and it gives $m_{pos}(x_0)$ and $m_{neg}(x_0)$ at all times x_0, with the correlators averaged over all spatial points for each timeslice. So not only does it require less inversions than the point source method, it measures the spatially averaged mass over all timeslices.

For the point source we inverted a unit source to get $S(x, y)$, which we then inserted into the expression:

$$\left[\zeta(y)\overline{\psi}(x)\right]_F = P_- U_{y-\widehat{0},0} S(y, x)|_{y_0=a} \tag{C.15}$$

However using the relation $\left\{\left[\psi(x)\overline{\zeta}(z)\right]_F\right\}^\dagger = \gamma_5 \left[\zeta(z)\overline{\psi}(x)\right]_F \gamma_5$, we could equally try to determine the expression:

$$\left[\psi(x)\overline{\zeta}(y)\right]_F = S(x, y) U^\dagger_{y-\widehat{0},0} P_+|_{y_0=a} \tag{C.16}$$

Since $S(x, y)$ is defined by $DS(x, y) = \delta_{xy}$, applying the Dirac operator to this gives:

$$D\left[\psi(x)\overline{\zeta}(y)\right]_F = \delta_{xy} U^\dagger_{y-\widehat{0},0} P_+|_{y_0=a} \tag{C.17}$$

So by inverting this source we find $\left[\psi(x)\overline{\zeta}(y)\right]_F$ directly, and similarly for the other boundary:

$$D\left[\psi(x)\overline{\zeta}'(y)\right]_F = \delta_{xy} U_{y,0} P_-|_{y_0=L-a} \tag{C.18}$$

These propagators can then be directly inserted into the original expressions for the correlation functions f_A, f_P, defined in Eqs. 3.14, 3.13. Since our source is now averaged over the boundary instead of a point in the bulk, we obtain the correlators spatially averaged over the boundary to all points in the bulk, instead

of just a single point in the bulk as in the point source method.

C.5 Boundary-to-Boundary Correlator

The boundary to boundary propagators can be written in terms of the unit source propagators as was done for the PCAC mass in Sec. C.3 [118]:

$$\left[\zeta(x)\overline{\zeta}'(y)\right]_F = P_- U_{x-a\hat{0},0} S(x,y) U_{y,0} P_-|_{x_0=a,y_0=T-a} \tag{C.19}$$

$$\left[\zeta'(x)\overline{\zeta}(y)\right]_F = P_+ U^\dagger_{x,0} S(x,y) U^\dagger_{y-a\hat{0},0} P_+|_{x_0=T-a,y_0=a} \tag{C.20}$$

However, actually summing over all these would require $2 \times L^3 \times (4N_F)$ inversions, which is clearly impractical. A small number of them could be randomly selected for each config and a stochastic estimate of the quantity could be found in this way, but once again using a wall source offers a better way to measure this quantity [118]. We can rewrite the boundary to boundary correlators in terms of the boundary to bulk correlators we already have from our wall source implementation in Sec. C.4:

$$\left[\zeta(x)\overline{\zeta}'(y)\right]_F = P_- U_{x-a\hat{0},0} \left[\psi(x)\overline{\zeta}'(y)\right]_F\Big|_{x_0=a,y_0=L-a} \tag{C.21}$$

$$\left[\zeta'(x)\overline{\zeta}(y)\right]_F = P_+ U^\dagger_{x,0} \left[\psi(x)\overline{\zeta}(y)\right]_F\Big|_{x_0=T-a,y_0=a} \tag{C.22}$$

where

$$D\left[\psi(x)\overline{\zeta}(y)\right]_F = \delta_{xy} U^\dagger_{y-\hat{0},0} P_+|_{y_0=a} \tag{C.23}$$

$$D\left[\psi(x)\overline{\zeta}'(y)\right]_F = \delta_{xy} U_{y,0} P_-|_{y_0=L-a} \tag{C.24}$$

These propagators can then be directly inserted into the expression for the boundary-to-boundary correlator f_1 in Eq. 3.20.

Appendix D

Tests of the SF Implementation

D.1 Introduction

A range of tests have been performed to ensure that the code is working correctly, including self-consistency checks, agreement with analytic predictions, reproduction of published results, and direct comparisons where possible with Chroma [119], an independent implementation of the Schrodinger Functional for certain representations and numbers of colours.

D.2 Existing Tests

The following existing tests work in the SF implementation, after modifications in some cases to ensure SF boundary conditions:

- Check that _group_represent is homomorphic
- Check gauge covariance of the Dirac operator
- Checks the old and the new implementation of the Dirac op
- Check of hermiticity of the Dirac op
- Check of the CG inversion
- Check of the MINRES inversion
- Check of QMR multishift

- Check the generators
- Check the eva module using a random field
- Check the consistency of spinor linear algebra
- Check the dirac_eva module using a random field
- Check that the 2AS is equivalent to FUND* for SU(3)
- Check reversibility of the molecular dynamics
- Check staples
- Check geometry

D.3 SF Boundary Conditions

The usual Dirac operator has a plane-wave analytic solution for unit gauge fields:

$$\psi = e^{i\mathbf{p}.\mathbf{x}} c_{\alpha\beta} \tag{D.1}$$

where α is the Dirac index, β is the colour index, and $c_{\alpha\beta}$ is constant in both. Unfortunately the Schrodinger Functional boundary conditions rule out such a solution with constant spinor components:

$$\left.\begin{array}{lcl} P_+\psi|_{x^0=0} = 0 & \Rightarrow & c_{0,\beta} = c_{1,\beta} = 0 \\ P_-\psi|_{x^0=T-a} = 0 & \Rightarrow & c_{2,\beta} = c_{3,\beta} = 0 \end{array}\right\} \Rightarrow c_{\alpha\beta} = 0 \tag{D.2}$$

However we can work out analytically what the dirac operator should produce when acting on a plane wave with the fermionic boundary conditions applied:

$$D_{x,y} = \delta_{xy}(m+4) - \frac{1}{2}\left[\delta_{x+\mu,y}(1+\gamma^\mu)U_{\mu,y} + \delta_{x-\mu,y}(1-\gamma^\mu){U^\dagger}_{\mu,y}\right] \tag{D.3}$$

$$\psi_x = \begin{cases} e^{i\mathbf{p}.\mathbf{x}} & \text{for} \quad a < x^0 < T - 2a \\ (0, 0, e^{i\mathbf{p}.\mathbf{x}}, e^{i\mathbf{p}.\mathbf{x}}) & \text{for} \quad x^0 = 0 \\ (e^{i\mathbf{p}.\mathbf{x}}, e^{i\mathbf{p}.\mathbf{x}}, 0, 0) & \text{for} \quad x^0 = T - a \end{cases} \tag{D.4}$$

In the bulk, i.e. $2a < x^0 < T - 3a$, we can set the gauge fields to the identity, and calculate the result of $D\psi$:

$$D_{xy}\psi_y = e^{i\mathbf{p}.\mathbf{x}}\left[(m+4) - \sum_{\mu=0}^{3}\{\cos(p_\mu) - i\gamma^\mu \sin(p_\mu)\}\right] \tag{D.5}$$

At $x^0 = a$, we can still set the gauge fields to the identity, but we need to take into account the boundary conditions in the x^0 direction:

$$\begin{aligned} D_{xy}\psi_y &= e^{i\mathbf{p}.\mathbf{x}}\left[(m+4) - \textstyle\sum_{\mu=1}^{3}\{\cos(p_\mu) - i\gamma^\mu \sin(p_\mu)\}\right] \\ &\quad -\tfrac{1}{2}\left[\begin{pmatrix} \cos(p_0) + i\sin(p_0) \\ 2\cos(p_0) \end{pmatrix} + \gamma^0 \begin{pmatrix} \cos(p_0) + i\sin(p_0) \\ 2i\sin(p_0) \end{pmatrix}\right] \end{aligned} \tag{D.6}$$

Similarly for $x^0 = T - 2a$:

$$\begin{aligned} D_{xy}\psi_y &= e^{i\mathbf{p}.\mathbf{x}}\left[(m+4) - \textstyle\sum_{\mu=1}^{3}\{\cos(p_\mu) - i\gamma^\mu \sin(p_\mu)\}\right] \\ &\quad -\tfrac{1}{2}\left[\begin{pmatrix} 2\cos(p_0) \\ \cos(p_0) - i\sin(p_0) \end{pmatrix} + \gamma^0 \begin{pmatrix} 2i\sin(p_0) \\ -\cos(p_0) + i\sin(p_0) \end{pmatrix}\right] \end{aligned} \tag{D.7}$$

At $x_0 = 0$ we need to take into account the background gauge fields as well as the boundary conditions, which includes applying the boundary conditions to the resulting spinor. The only gamma matrix which mixes the top two and bottom two components of the spinor is γ^0. Here the spatial gauge fields at $x_0 = 0$ are all the same, W:

$$\begin{aligned} D_{xy}\psi_y &= (m+4)\begin{pmatrix} 0 \\ \cos(p_0) + i\sin(p_0) \end{pmatrix} - \tfrac{1}{2}P_-\left[(1+\gamma^0)\, e^{ip_0 a} e^{i\mathbf{p}.\mathbf{x}}\right] \\ &\quad -\tfrac{1}{2}\textstyle\sum_{\mu=1}^{3}\left[(1+\gamma^\mu)We^{ip_\mu a}\begin{pmatrix} 0 \\ e^{i\mathbf{p}.\mathbf{x}} \end{pmatrix} + (1-\gamma^\mu)W^\dagger e^{-ip_\mu a}\begin{pmatrix} 0 \\ e^{i\mathbf{p}.\mathbf{x}} \end{pmatrix}\right] \end{aligned} \tag{D.8}$$

Similarly for $x^0 = T - a$, where the spatial gauge fields are denoted by W':

$$\begin{aligned} D_{xy}\psi_y &= (m+4)\begin{pmatrix} 0 \\ \cos(p_0) + i\sin(p_0) \end{pmatrix} - \tfrac{1}{2}P_+\left[(1-\gamma^0)\, e^{-ip_0 a} e^{i\mathbf{p}.\mathbf{x}}\right] \\ &\quad -\tfrac{1}{2}\sum_{\mu=1}^{3}\left[(1+\gamma^\mu)W' e^{ip_\mu a}\begin{pmatrix} 0 \\ e^{i\mathbf{p}.\mathbf{x}} \end{pmatrix} + (1-\gamma^\mu)(W')^\dagger e^{-ip_\mu a}\begin{pmatrix} 0 \\ e^{i\mathbf{p}.\mathbf{x}} \end{pmatrix}\right] \end{aligned} \tag{D.9}$$

This test is implemented and happily the code agrees with the results above. While this is not conclusive evidence that it is the correct physical operator, it is strong evidence that is has the correct boundary conditions, since it works for any allowed value of the plane wave momenta $p_\mu = \frac{2\pi n_\mu}{L}$ for integer n_μ, with random color components.

D.4 Eigenvalues in the Free Case

For the free (unit gauge field) case with zero bare mass, as the continuum limit is approached the smallest eigenvalue of the Dirac operator should approach $(\frac{\pi}{2L})$, with the full set of eigenvalues in this limit given by [94]

$$\lambda^2 = p_0^2 + \mathbf{p}^2 \tag{D.10}$$

where

$$\begin{aligned} p_0 &= \tfrac{\pi}{2L}(2n_0+1) \quad n_0 \in \mathcal{N} \geq 0 \\ \mathbf{p} &= \tfrac{2\pi}{L}(n_1, n_2, n_3) \quad n_i \in \mathcal{N} \end{aligned} \tag{D.11}$$

The expected values and multiplicities for the first few eigenvalues are listed in Tab. D.1

Eigenvalue / $(\pi/2L)^2$	Multiplicity / $4N_F$
1	1
9	1
17	6
25	7
33	12

Table D.1: Free field eigenvalues of the Dirac operator with their multiplicities.

These eigenvalues have been measured in the code for $L = 6, 8, \ldots, 28$, shown

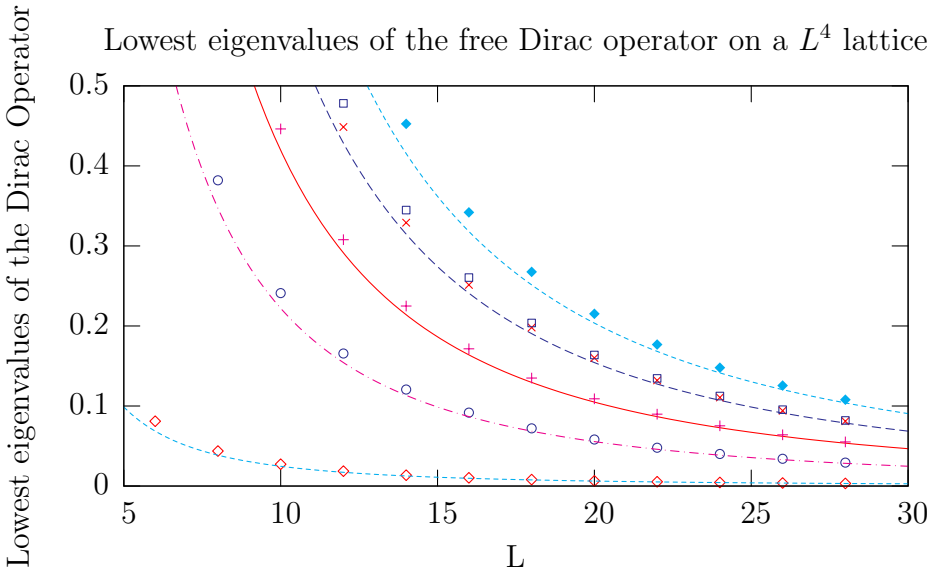

Figure D.1: Measured free field eigenvalues compared with the analytic predictions.

in Fig. D.1 along with the analytic predictions. They agree quite well with the expected analytic values: they have the correct approximate degeneracies, and the agreement improves as L is increased. This can be seen more clearly in Fig. D.2 where the L-dependence has been removed by dividing each eigenvalue by $(\pi/2L)^2$.

The eigenvalue spectrum has also been calculated in the continuum limit for the Abelian Gauge fields induced by the boundary gauge configs in SU(3) by Sint and Sommer [97]. They also measured the spectrum for $L = 6, 12, 24$, with both periodic spatial boundary conditions ($\theta = 0$), and twisted spatial boundary conditions ($\theta = \pi/5$). All these spectra were reproduced using the HiRep implementation and all values agreed within machine precision.

So this is very good evidence that the Dirac operator is correctly implemented, and also that the twisted boundary conditions are working.

D.5 Pure Gauge Results

The first non-trivial test of the code is to try to reproduce some published results for the pure gauge case. For a given SU(N) all that needs to be done is to insert the boundary gauge fields and change the λ term in the observable. This has

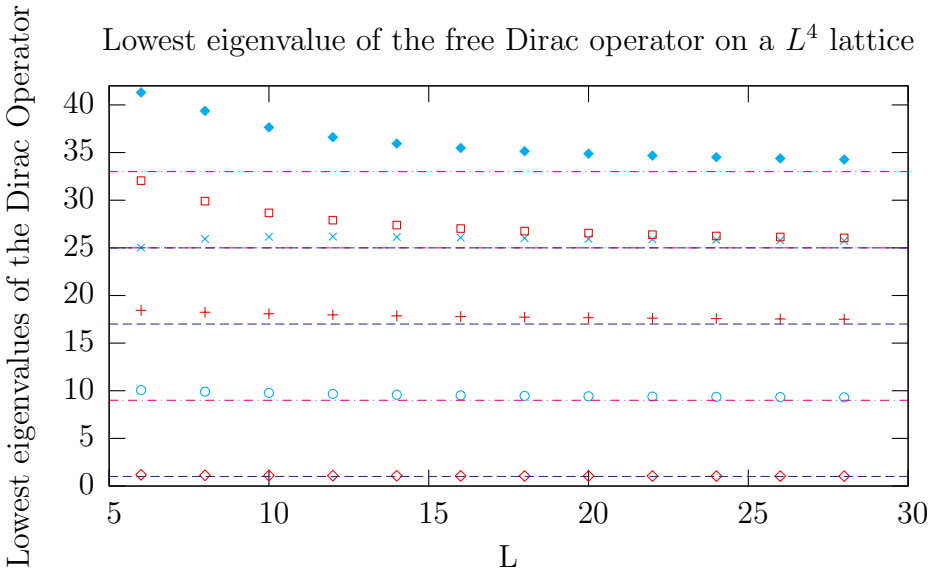

Figure D.2: Measured free field eigenvalues with L-dependence removed, compared with analytic predictions.

been done for $N = 2, 3, 4$ since there are results available for these values.

For $N = 2$, η is evaluated at $\eta = \pi/4$, with

$$C_k = \frac{i}{L}\begin{pmatrix} -\eta & 0 \\ 0 & \eta \end{pmatrix}, \quad C'_k = \frac{i}{L}\begin{pmatrix} \eta - \pi & 0 \\ 0 & \pi - \eta \end{pmatrix} \tag{D.12}$$

and $\lambda = \mathrm{diag}\,(1, -1)$. The results are shown in Fig D.3, for various values of β on various sizes of L^4 lattices. Each value is normalised by the published value in Ref. [96], (so that a value of 1 would indicate perfect agreement with the published value), and the agreement is very good.

For $N = 4$, η is evaluated at $\eta = 0$, with

$$C_k = \frac{i}{L}\begin{pmatrix} -\frac{1}{2}\eta - \frac{\sqrt{2}\pi}{4} & 0 & 0 & 0 \\ 0 & -\frac{1}{2}\eta - \frac{(2-\sqrt{2})\pi}{4} & 0 & 0 \\ 0 & 0 & \frac{1}{2}\eta + \frac{(2-\sqrt{2})\pi}{4} & 0 \\ 0 & 0 & 0 & \frac{1}{2}\eta + \frac{\sqrt{2}\pi}{4} \end{pmatrix}, \tag{D.13}$$

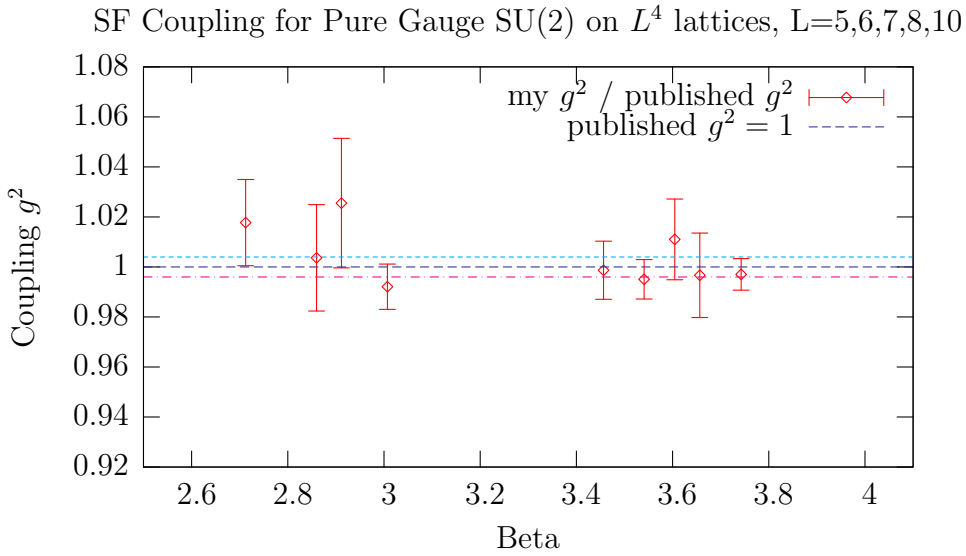

Figure D.3: SU(2) Pure gauge results compared with results from Ref. [96].

$$C'_k = \frac{i}{L}\begin{pmatrix} \frac{1}{2}\eta - \frac{(2+\sqrt{2})\pi}{4} & 0 & 0 & 0 \\ 0 & \frac{1}{2}\eta - \frac{(4-\sqrt{2})\pi}{4} & 0 & 0 \\ 0 & 0 & -\frac{1}{2}\eta + \frac{(4-\sqrt{2})\pi}{4} & 0 \\ 0 & 0 & 0 & -\frac{1}{2}\eta + \frac{(2+\sqrt{2})\pi}{4} \end{pmatrix}, \tag{D.14}$$

and $\lambda = \mathrm{diag}\left(\frac{1}{2}, \frac{1}{2}, -\frac{1}{2}, -\frac{1}{2}\right)$. Again the results normalised to the values in Ref. [120] are shown in Fig. D.4, and agree well.

For $N = 3$, η is evaluated at $\eta = 0$, with

$$C_k = \frac{i}{L}\begin{pmatrix} \eta - \frac{\pi}{3} & 0 & 0 \\ 0 & -\frac{1}{2}\eta & 0 \\ 0 & 0 & -\frac{1}{2}\eta + \frac{\pi}{3} \end{pmatrix}, \quad C'_k = \frac{i}{L}\begin{pmatrix} -\eta - \pi & 0 & 0 \\ 0 & \frac{1}{2}\eta + \frac{\pi}{3} & 0 \\ 0 & 0 & \frac{1}{2}\eta + \frac{2\pi}{3} \end{pmatrix} \tag{D.15}$$

and $\lambda = \mathrm{diag}\left(1, -\frac{1}{2}, -\frac{1}{2}\right)$. The values published in Ref. [121] use an improved action, with different weights for time-like plaquettes on the boundaries. Having added this improvement to the code, the SU(3) results are also consistent and are shown in Fig. D.5.

So the code appears to be working well for the pure gauge case, both with and without boundary improvement terms.

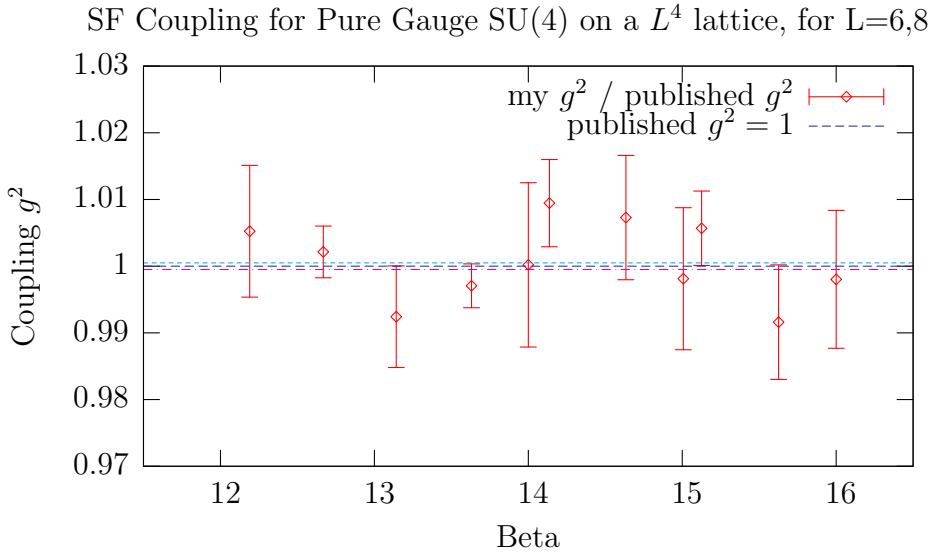

Figure D.4: SU(4) Pure gauge results compared with results from Ref. [120].

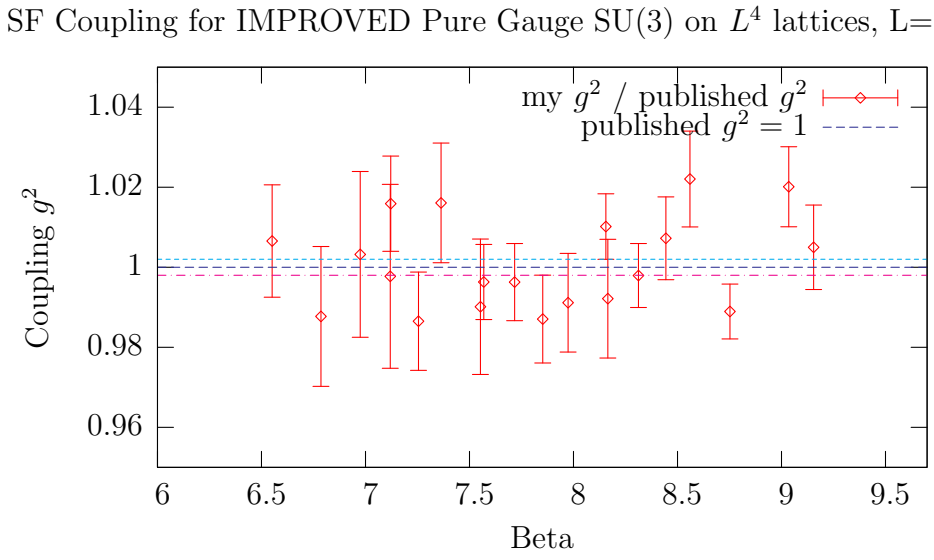

Figure D.5: SU(3) Improved pure gauge results compared with results from Ref. [121].

Representation	β	Pure Gauge g^2	RHMC g^2
SU(2) FUNDAMENTAL	3.5408	2.027(16)	1.986(31)
SU(2) FUNDAMENTAL	4.0000	1.623(4)	1.678(63)
SU(3) FUNDAMENTAL	7.5000	1.743(6)	1.683(63)
SU(3) FUNDAMENTAL	8.8997	1.205(4)	1.184(35)

Table D.2: Coupling $\overline{g}^2$ for heavy mass RHMC compared with pure gauge value.

D.6 RHMC Heavy Mass

Running the RHMC with a very large bare mass should decouple the quarks, reproducing the pure gauge results regardless of the chosen representation. The measured coupling g^2 for heavy masses along with the pure gauge value is shown in Tab. D.2, and they are consistent within statistical errors.

D.7 RHMC SU(2) Results

RHMC results for two dirac fermions in the fundamental representation of SU(2) for a range of κ at $\beta = 3.0$ were calculated using both HiRep and Chroma. The coupling $\overline{g}^2$ is shown in Fig. D.6, and the agreement between these independent implementations is very good.

The PCAC masses also agree well. The Chroma mass uses a wall source at the boundary and averages over the middle timeslice. This is compared to the HiRep implementation of the wall source PCAC mass in Fig. D.7. The point source PCAC mass in HiRep is also consistent with the Chroma wall source mass, as shown in Fig. D.8. Finally the two different methods in HiRep are also consistent with each other, as shown in Fig. D.9

D.8 PCAC Mass Consistency

A simple test of the inversion code is to check that:

$$S(x,y)^\dagger = \gamma_5 S(y,x)\gamma_5 \tag{D.16}$$

This was done between two points on the same config and the two propagators obeyed this relation.

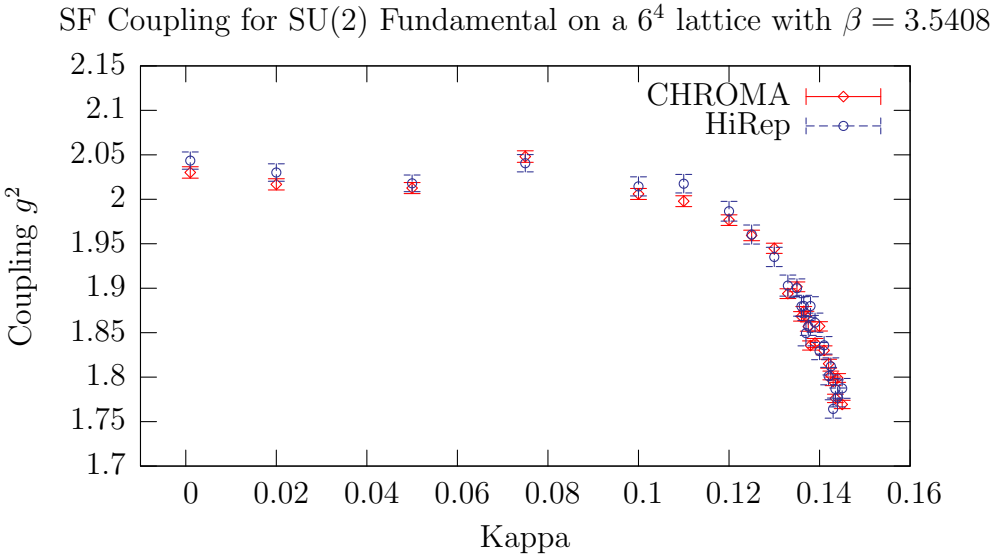

Figure D.6: Comparison of coupling between HiRep and Chroma for two dirac fermions in the fundamental representation of SU(2).

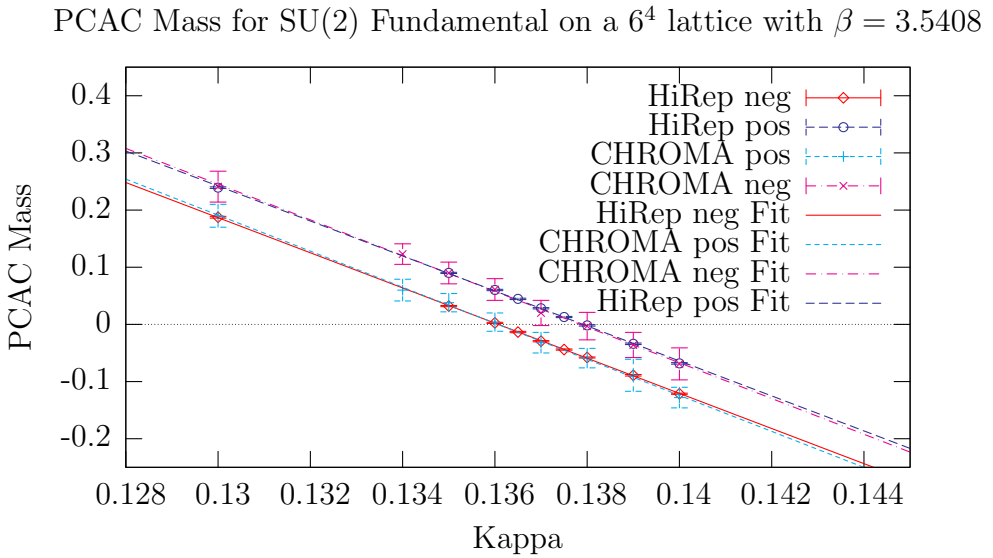

Figure D.7: RHMC SU(2) Fundamental comparison of wall source PCAC mass in HiRep with wall source PCAC mass in Chroma.

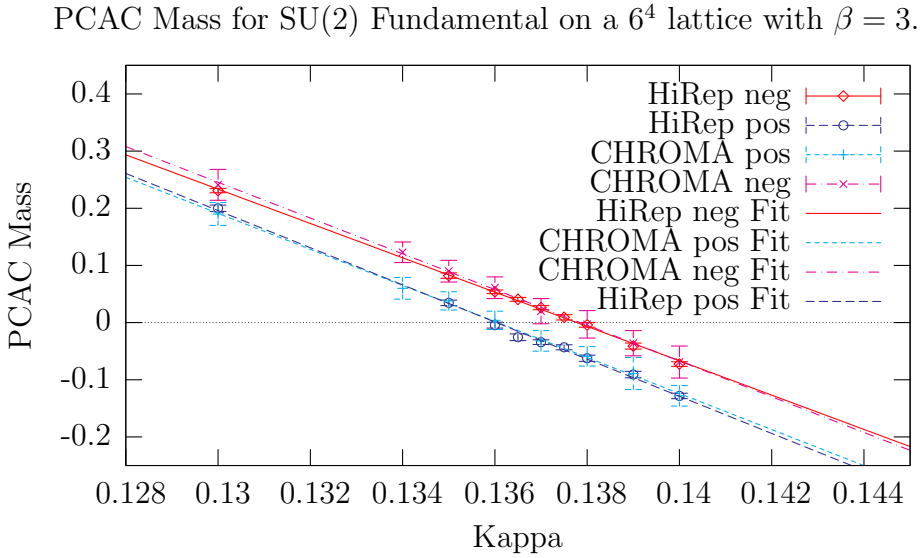

Figure D.8: RHMC SU(2) Fundamental comparison of point source PCAC mass in HiRep with wall source PCAC mass in Chroma.

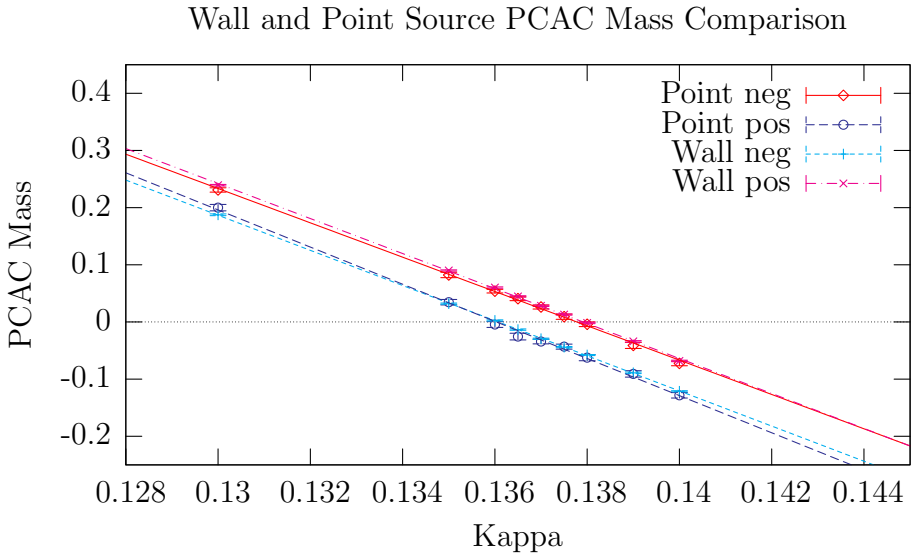

Figure D.9: RHMC SU(2) Fundamental comparison of point and wall source PCAC masses within HiRep.

It is also possible to directly compare the propagators created by the two different methods if the wall source is replaced by a point source. In the first case we invert a point source at the centre to get $S(y,x)$, the propagator from all points y to the central point x:

$$DS(y,x) = \delta_{y,x}|_{x=(L/2,0,0,0)} \tag{D.17}$$

The propagator from a point y on the boundary, to the central point x, is then given by:

$$\left[\zeta(y)\overline{\psi}(x)\right]_F = P_- U(y-\widehat{0},0)S(y,x)|_{y_0=a} \tag{D.18}$$

In the second case we multiply and project a source at $(y_0 = a, \mathbf{y})$, before inverting to get $H(x,y)$, the propagator from all interior points x to the point $(y_0 = 0, \mathbf{y})$ on the boundary:

$$DH(x,y) = \delta_{xy} U(y-\widehat{0},0)^\dagger P_+|_{y_0=a} \tag{D.19}$$

The propagator is then given by:

$$\left[\psi(x)\overline{\zeta}(y)\right]_F = H(x,y) \tag{D.20}$$

These two propagators can be related using the relation:

$$\left\{\left[\psi(x)\overline{\zeta}(z)\right]_F\right\}^\dagger = \gamma_5 \left[\zeta(z)\overline{\psi}(x)\right]_F \gamma_5 \tag{D.21}$$

On the same SU2 Fundamental config for two points x and y, the two propagators obeyed this relation:

$$\gamma_5 \left\{H(x,y)\right\}^\dagger \gamma_5 = S(y,x) \tag{D.22}$$

This is a strong test of the consistency of the two PCAC mass implementations.

D.9 Propagator Comparisons

Directly comparing elements of a propagator on the same config between HiRep and Chroma is a very strong test of both implementations. It is also quite

difficult due to different choices for the dirac matrix representation creating what is effectively a different dirac operator. Another issue is whether D or $\gamma_5 D$ is being inverted.

Checking the latter is simple, since it is the only difference which affects the trace of the propagator for a unit source. Using this fact it turned out that they were indeed inverting different operators:

$$\mathrm{Tr}(\gamma_5 S^H) = \mathrm{Tr}(S^C) \tag{D.23}$$

Specifically HiRep inverts $\gamma_5 D$, while Chroma inverts D. This is easily dealt with by multiplying the source in hirep by γ_5 before inverting.

Any representation of the dirac matrices can be rotated into another one by a unitary transformation

$$\gamma_\mu^C = U \gamma_\mu^H U^\dagger \tag{D.24}$$

So at this point the trace, and hence any correlators calculated using these propagators will agree for a unit source, but the matrices themselves are still different since they are acting on fermions in different dirac matrix representations.

In order to determine U we need to know how the chosen representations differ, and also how the dirac operator implementation differs.

The difference in dirac matrices is just an opposite sign for all except γ_2^H and γ_5^H. There is also a difference in convention for numbering them - the order is (t, x, y, z) in HiRep, but (x, y, z, t) in Chroma. The Dirac operator implementation seems to be the same for both.

$$\begin{aligned} \gamma_0^H &= -\gamma_3^C \\ \gamma_1^H &= -\gamma_0^C \\ \gamma_2^H &= \gamma_1^C \\ \gamma_3^H &= -\gamma_2^C \\ \gamma_5^H &= \gamma_5^C \end{aligned} \tag{D.25}$$

So the U required should just flip the sign of all the dirac matrices except γ_2^H and γ_5^H, i.e. $U = \gamma_0^H \gamma_1^H \gamma_3^H$. This can be simplified:

$$U = \gamma_0^H \gamma_1^H \gamma_3^H (\gamma_2^H \gamma_2^H) = -(\gamma_0^H \gamma_1^H \gamma_2^H \gamma_3^H)\gamma_2^H = -\gamma_5^H \gamma_2^H = \gamma_2^H \gamma_5^H \tag{D.26}$$

Since there are no γ_5^H's in the Dirac operator this can be further simplified. Consider it acting on a Dirac matrix γ_μ^H inside the Dirac operator:

$$(\gamma_2^H\gamma_5^H)\gamma_\mu^H(\gamma_2^H\gamma_5^H)^\dagger = -\gamma_2^H(\gamma_5^H\gamma_5^H)\gamma_\mu^H(\gamma_2^H)^\dagger = \gamma_2^H\gamma_\mu^H\gamma_2^H \tag{D.27}$$

So the final transformation required is very simple:

$$S^C = \gamma_2^H S^H \gamma_2^H \tag{D.28}$$

Given a source in Chroma, we need to rotate it to the HiRep basis, multiply by γ_5 to account for the different choice of operator to invert, and then the resulting propagator needs to be rotated back to the Chroma basis to be able to compare them directly. Explicity the steps are:

1. Invert some source ϕ in chroma: $S^C = (D^C)^{-1}\phi^C$
2. Rotate the source to the hirep basis: $\phi^H = \gamma_5\gamma_2\phi^C$
3. Invert this source in hirep: $S^H = (\gamma_5 D^H)^{-1}\phi^H$
4. Rotate back to the chroma basis: $S^H \to \gamma_2 S^H$
5. Check that they are the same: $S^H \stackrel{?}{=} S^C$

The above has been done on a shared SU(3) Fundamental gauge configuration with SF boundary conditions, and agreement was obtained for the following sources:

- Unit
- Unit multiplied by gauge link
- Unit projected
- Unit multiplied and projected
- Wall
- Wall multiplied and projected

The correlators $f_P(x)$ and $f_A(x)$ were compared for both boundaries on the same config, using the multiplied and projected wall sources, and the agreement was within machine precision, for the following representations:

- SU3 Fundamental
- SU2 Fundamental
- SU3 Adjoint
- SU2 Adjoint

This is a very strong test of the implementation of the PCAC mass in both Chroma and HiRep.

Appendix E

Conventions

E.1 HiRep Conventions

The lattice consists of a $L^3 \times T$ four-dimensional hypercubic lattice with spacing a. In Euclidean space the gamma matrices are hermitian,

$$\gamma_\mu^\dagger = \gamma_\mu, \quad \{\gamma_\mu, \gamma_\nu\} = 2\delta_{\mu\nu}, \quad \sigma_{\mu\nu} = \frac{i}{2}\left[\gamma_\mu, \gamma_\nu\right], \quad \sigma_{0,k} = \begin{pmatrix} \sigma_k & 0 \\ 0 & -\sigma_k \end{pmatrix}. \tag{E.1}$$

The explicit representation chosen in HiRep is

$$\gamma_0 = \begin{pmatrix} 0 & -I \\ -I & 0 \end{pmatrix}, \quad \gamma_k = \begin{pmatrix} 0 & -i\sigma_k \\ i\sigma_k & 0 \end{pmatrix}, \quad \gamma_5 = \begin{pmatrix} I & 0 \\ 0 & -I \end{pmatrix}, \tag{E.2}$$

where the chiral projectors take the simple form

$$P_+ = \tfrac{1}{2}(1+\gamma_5) = \begin{pmatrix} I & 0 \\ 0 & 0 \end{pmatrix}, \quad P_- = \tfrac{1}{2}(1-\gamma_5) = \begin{pmatrix} 0 & 0 \\ 0 & I \end{pmatrix}. \tag{E.3}$$

E.2 Group Invariants

Table E.1 lists group invariants for fundamental, adjoint, 2–index symmetric, and 2–index antisymmetric representations, reproduced here for convenience from Table 2 in Ref. [40].

R	d_R	T_R	$C_2(R)$
fund	N	$1/2$	$(N^2-1)/(2N)$
Adj$\equiv A$	N^2-1	N	N
2S	$N(N+1)/2$	$(N+2)/2$	$C_2(F)2(N+2)/(N+1)$
2AS	$N(N-1)/2$	$(N-2)/2$	$C_2(F)\frac{2(N-2)}{N-1}$

Table E.1: Group invariants used in this work

Appendix F

MCRG

F.1 Observables

Explicit expressions for the seven observables used in the matching are given by

$$\begin{aligned}
\mathcal{O}_1 &= \textstyle\sum_{\mu=1}^{4}\sum_{\nu=0}^{\mu} P(\mu,\nu), \\
\mathcal{O}_2 &= \textstyle\sum_{\mu=1}^{4}\sum_{\nu=0}^{\mu} L_6(\mu,\nu,\rho=(\mu+1) \bmod 4), \\
\mathcal{O}_3 &= \textstyle\sum_{\mu=1}^{4}\sum_{\nu=0}^{\mu} L_6(\mu,\nu,\rho=(\mu+2) \bmod 4), \\
\mathcal{O}_4 &= \textstyle\sum_{\mu=1}^{4}\sum_{\nu=0}^{\mu} L_6(\mu,\nu,\rho=(\mu+3) \bmod 4), \\
\mathcal{O}_5 &= \textstyle\sum_{\mu=1}^{4}\sum_{\nu=0}^{\mu} L_8(\mu,\nu,\rho=(\mu+1) \bmod 4,\alpha=(\mu+1) \bmod 4), \\
\mathcal{O}_6 &= \textstyle\sum_{\mu=1}^{4}\sum_{\nu=0}^{\mu} L_8(\mu,\nu,\rho=(\mu+2) \bmod 4,\alpha=(\mu+1) \bmod 4), \\
\mathcal{O}_7 &= \textstyle\sum_{\mu=1}^{4}\sum_{\nu=0}^{\mu} L_8(\mu,\nu,\rho=(\mu+3) \bmod 4,\alpha=(\mu+1) \bmod 4),
\end{aligned} \tag{F.1}$$

where

$$\begin{aligned}
P(\mu,\nu) &= \textstyle\sum_x \Re\mathrm{Tr}\left[U_{x,\mu}U_{x+\mu,\nu}U^\dagger_{x+\nu,\mu}U^\dagger_{x,\nu}\right], \\
L_6(\mu,\nu,\rho) &= \textstyle\sum_x \Re\mathrm{Tr}\left[U_{x,\mu}U_{x+\mu,\nu}U_{x+\mu+\nu,\rho}U^\dagger_{x+\nu+\rho,\mu}U^\dagger_{x+\nu,\rho}U^\dagger_{x,\nu}\right], \\
L_8(\mu,\nu,\rho) &= \textstyle\sum_x \Re\mathrm{Tr}\left[U_{x,\mu}U_{x+\mu,\nu}U_{x+\mu+\nu,\rho}U_{x+\mu+\nu+\rho,\alpha}U^\dagger_{x+\nu+\rho+\alpha,\mu}U^\dagger_{x+\nu+\rho,\alpha}U^\dagger_{x+\nu,\rho}U^\dagger_{x,\nu}\right].
\end{aligned} \tag{F.2}$$

F.2 PCAC masses

The PCAC mass measured on the 8^4 lattices suffers from a finite–volume effect, the time extent of the lattice is not sufficient for the mass to reach a plateau. This can be seen in Fig. F.1, where the PCAC mass for the same values of (β, m)

on lattices of size 8^4 and 16^4 are compared.

The lattice artefacts however seem to be small - the PCAC mass as a function of t agrees well between the two lattices. We use the PCAC mass measured at $t = 8$ on the 16^4 lattices throughout this paper to convert bare masses to PCAC masses. To estimate the systematic error due to this procedure, we can compare the PCAC mass at the same timeslice $t = 4$ on the two lattice sizes, as shown in Fig F.2. The difference is smaller than the statistical error on the PCAC mass for small masses, and increases approximately linearly with mass to ~ 0.005 at $\overline{m} = 0.20$. To include this source of error, a systematic error of $0.025\overline{m}$ was added linearly to the measured error on each matching mass.

The PCAC mass measured on a 32^4 lattice is also shown in Fig F.1, which has a clear plateau, and is consistent withe the value measured on a 16^4 lattice at $t = 8$, indicating that any residual finite size effects are small.

F.3 Matching mass range

We have assumed that the contribution from the irrelevant directions is negligible by the time we perform the matching. But in reality we match after only one or two steps, and there may still be a contribution coming from the coupling. We are forcing the matching coupling to the same value as the initial coupling. This causes a shift in the measured observable, which is then cancelled by a shift in the observed matching mass from the true value.

Consider the situation where we measure some observable $\mathcal{O}^{(n)}(\beta, m)$ on the larger lattice after n blocking steps. The correct matching done in both the coupling and the mass would give m', β' such that

$$\mathcal{O}^{(n-1)}(\beta', m') = \mathcal{O}^{(n)}(\beta, m)$$

Instead we fix $\beta' = \beta$ and find m'' such that

$$\mathcal{O}^{(n-1)}(\beta, m'') = \mathcal{O}^{(n)}(\beta, m)$$

Dropping the $^{(n-1)}$ superscript on $\mathcal{O}$ and taylor expanding around the correct matching values gives

$$\mathcal{O}(\beta, m'') = \mathcal{O}(\beta', m') + c_\beta(\beta - \beta') + c_m(m'' - m')$$

where

$$c_\beta = \left.\frac{\partial \mathcal{O}}{\partial \beta}\right|_{\beta', m'}, \quad c_m = \left.\frac{\partial \mathcal{O}}{\partial m''}\right|_{\beta', m'}$$

This gives the relation

$$m'' = m' - \frac{c_\beta}{c_m}(\beta - \beta').$$

So the effect of not matching in β' will cause the measured m'' matched to $m = 0$ to be shifted away from zero.

For this reason we excluded the matchings at $m < 0.02$ from the anomalous mass dimension fits, since they are likely to have significant contributions from the running of the coupling, although including them makes little difference to the fits.

In fact the size of this shift at $m = 0$ could give us an indirect way to measure the running of the coupling. At $m = 0$, we know that $m' = 0$, which gives the relation

$$(\beta - \beta') = -\frac{c_m}{c_\beta} m''.$$

The difficulty in determining c_m and c_β, as well as the relatively large uncertainty on the measurement of m'', means that although in principle this would be a way to measure $(\beta - \beta')$, in practice it is not feasible with our data.

F.4 Massless interpolation

The difference between the measured critical bare masses, and the values predicted by the interpolation function, are very small as shown in Fig F.3. This implies a systematic error $\lesssim 0.001$ on the PCAC masses due to the interpolating function.

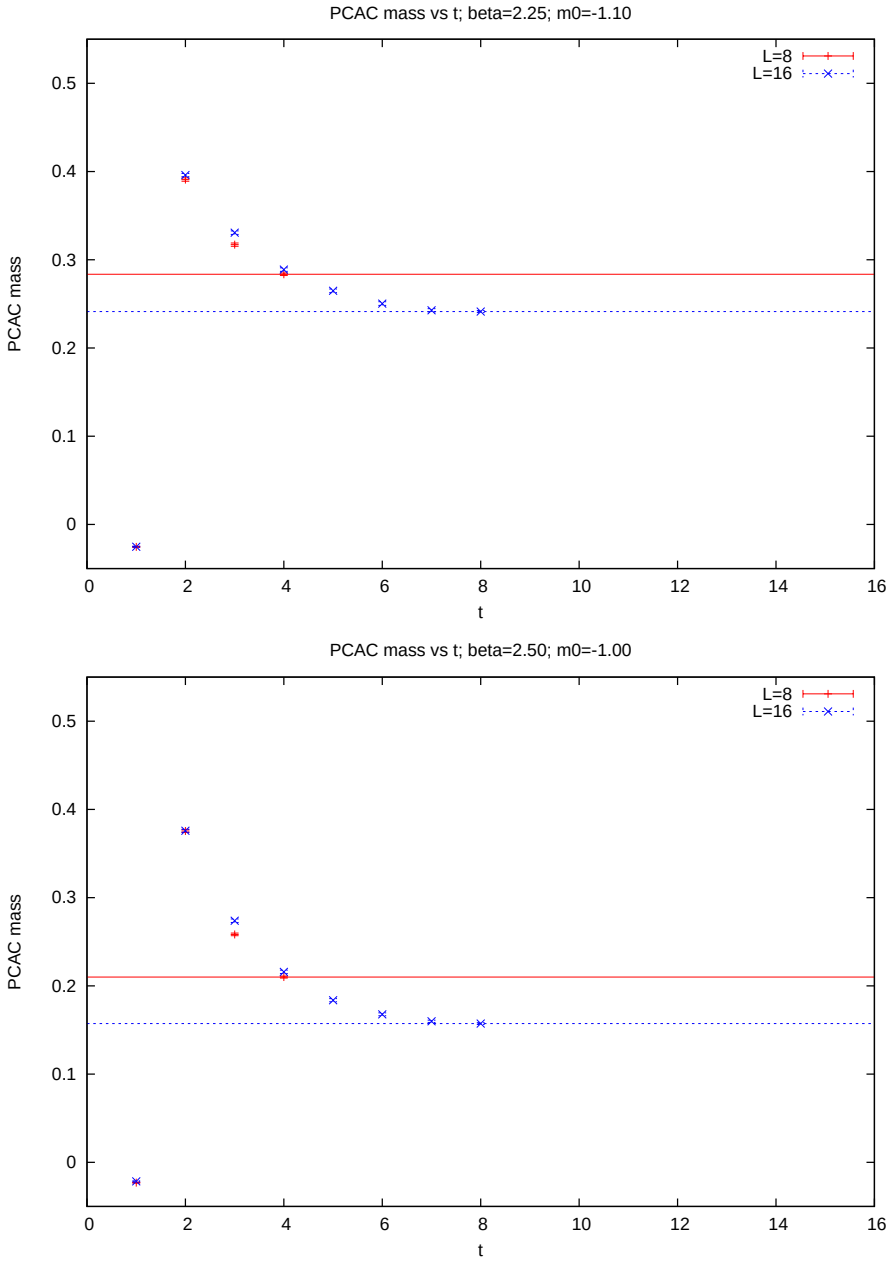

Figure F.1: PCAC mass as a function of time on 8^4 and 16^4 lattices.

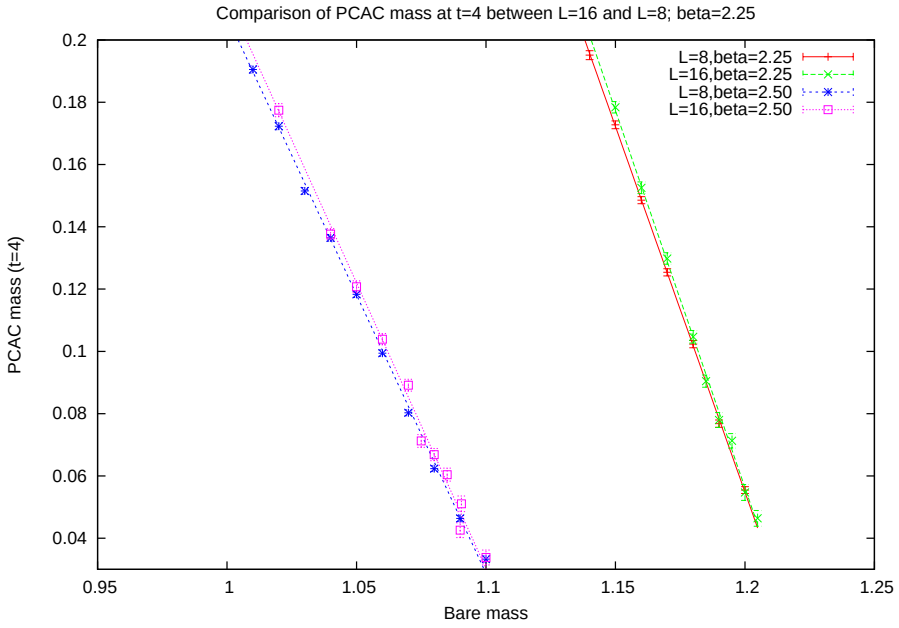

Figure F.2: PCAC mass at t=4 on 8^4 and 16^4 lattices.

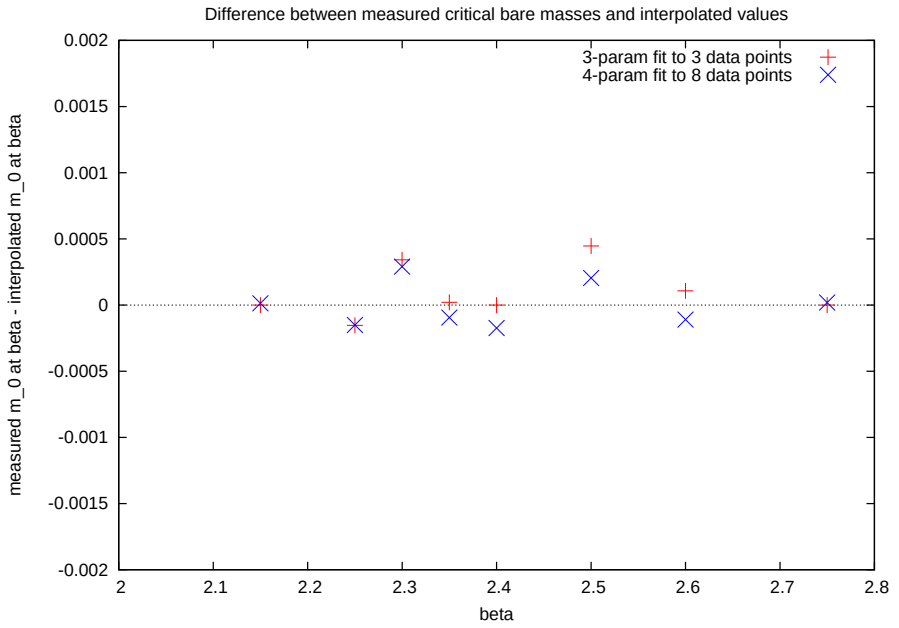

Figure F.3: To estimate the systematic error, here is the difference between measured critical bare masses, and the values given by a 3–parameter interpolation function fitted to only three of the measured values. Also shown is the difference between measured values and a 4–parameter interpolation function fit to all the data. The difference in PCAC mass is $(1.5 - 3.5)\times$ this bare mass difference, which is still $\lesssim 0.001$, and smaller than the statistical uncertainty on the measured PCAC mass.

Bibliography

[1] Steven Weinberg. A Model of Leptons. *Phys. Rev. Lett.*, 19:1264–1266, 1967.

[2] K Nakamura et al. Review of particle physics. *J. Phys.*, G37:075021, 2010.

[3] Peter W. Higgs. Broken symmetries, massless particles and gauge fields. *Phys. Lett.*, 12:132–133, 1964.

[4] F. Englert and R. Brout. BROKEN SYMMETRY AND THE MASS OF GAUGE VECTOR MESONS. *Phys. Rev. Lett.*, 13:321–322, 1964.

[5] G. S. Guralnik, C. R. Hagen, and T. W. B. Kibble. GLOBAL CONSERVATION LAWS AND MASSLESS PARTICLES. *Phys. Rev. Lett.*, 13:585–587, 1964.

[6] Jeffrey Goldstone, Abdus Salam, and Steven Weinberg. Broken Symmetries. *Phys. Rev.*, 127:965–970, 1962.

[7] J. Goldstone. Field Theories with Superconductor Solutions. *Nuovo Cim.*, 19:154–164, 1961.

[8] S. L. Glashow. Partial Symmetries of Weak Interactions. *Nucl. Phys.*, 22:579–588, 1961.

[9] Abdus Salam. Weak and Electromagnetic Interactions. Originally printed in *Svartholm: Elementary Particle Theory, Proceedings Of The Nobel Symposium Held 1968 At Lerum, Sweden*, Stockholm 1968, 367-377.

[10] Michael E. Peskin and Daniel V. Schroeder. An Introduction to quantum field theory. Reading, USA: Addison-Wesley (1995) 842 p.

[11] Leonard Susskind. Dynamics of Spontaneous Symmetry Breaking in the Weinberg- Salam Theory. *Phys. Rev.*, D20:2619–2625, 1979.

[12] David J. E. Callaway. Triviality Pursuit: Can Elementary Scalar Particles Exist? *Phys. Rept.*, 167:241, 1988.

[13] Hideki Yukawa. On the interaction of elementary particles. *Proc. Phys. Math. Soc. Jap.*, 17:48–57, 1935.

[14] Gian Francesco Giudice. Theories for the Fermi Scale. *J. Phys. Conf. Ser.*, 110:012014, 2008. `arXiv:0710.3294`.

[15] Edward Farhi and Leonard Susskind. Technicolor. *Phys. Rept.*, 74:277, 1981.

[16] Steven Weinberg. Implications of Dynamical Symmetry Breaking: An Addendum. *Phys. Rev.*, D19:1277–1280, 1979.

[17] E. Farhi and Leonard Susskind. A Technicolored G.U.T. *Phys. Rev.*, D20:3404–3411, 1979.

[18] Estia Eichten and Kenneth D. Lane. Dynamical Breaking of Weak Interaction Symmetries. *Phys. Lett.*, B90:125–130, 1980.

[19] Savas Dimopoulos and Leonard Susskind. Mass Without Scalars. *Nucl. Phys.*, B155:237–252, 1979.

[20] Christopher T. Hill and Elizabeth H. Simmons. Strong dynamics and electroweak symmetry breaking. *Phys. Rept.*, 381:235–402, 2003. `arXiv:hep-ph/0203079`.

[21] Michael E. Peskin and Tatsu Takeuchi. A New constraint on a strongly interacting Higgs sector. *Phys. Rev. Lett.*, 65:964–967, 1990.

[22] Guido Altarelli and Riccardo Barbieri. Vacuum polarization effects of new physics on electroweak processes. *Phys. Lett.*, B253:161–167, 1991.

[23] Michael E. Peskin and Tatsu Takeuchi. Estimation of oblique electroweak corrections. *Phys. Rev.*, D46:381–409, 1992.

[24] Kenneth Lane. Two lectures on technicolor. 2002. `arXiv:hep-ph/0202255`.

[25] Bob Holdom. Techniodor. *Phys. Lett.*, B150:301, 1985.

[26] Bob Holdom. FLAVOR CHANGING SUPPRESSION IN TECHNICOLOR. *Phys. Lett.*, B143:227, 1984.

[27] Koichi Yamawaki, Masako Bando, and Ken-iti Matumoto. Scale Invariant Technicolor Model and a Technidilaton. *Phys. Rev. Lett.*, 56:1335, 1986.

[28] Raman Sundrum and Stephen D. H. Hsu. Walking technicolor and electroweak radiative corrections. *Nucl. Phys.*, B391:127–146, 1993. `arXiv:hep-ph/9206225`.

[29] Thomas Appelquist and Francesco Sannino. The Physical Spectrum of Conformal SU(N) Gauge Theories. *Phys. Rev.*, D59:067702, 1999. `arXiv:hep-ph/9806409`.

[30] Zhi-yong Duan, P. S. Rodrigues da Silva, and Francesco Sannino. Enhanced global symmetry constraints on epsilon terms. *Nucl. Phys.*, B592:371–390, 2001. `arXiv:hep-ph/0001303`.

[31] Francesco Sannino and Kimmo Tuominen. Orientifold theory dynamics and symmetry breaking. *Phys. Rev.*, D71:051901, 2005. `arXiv:hep-ph/0405209`.

[32] Dennis D. Dietrich and Francesco Sannino. Walking in the SU(N). *Phys. Rev.*, D75:085018, 2007. `arXiv:hep-ph/0611341`.

[33] J. R. Andersen et al. Discovering Technicolor. 2011. arXiv:1104.1255.

[34] Francesco Sannino. Dynamical Stabilization of the Fermi Scale: Phase Diagram of Strongly Coupled Theories for (Minimal) Walking Technicolor and Unparticles. 2008. arXiv:0804.0182.

[35] Francesco Sannino. Technicolor and Beyond: Unification in Theory Space. *J. Phys. Conf. Ser.*, 259:012003, 2010. arXiv:1010.3461.

[36] Luigi Del Debbio. The conformal window on the lattice. *PoS*, LATTICE2010:004, 2010.

[37] Thomas DeGrand. Lattice studies of QCD-like theories with many fermionic degrees of freedom. 2010. arXiv:1010.4741.

[38] J. Chyla. INFRARED FIXED POINTS IN ASYMPTOTICALLY FREE FIELD THEORIES: WHAT DO THEY TELL US? *Phys. Rev.*, D38:3845–3849, 1988.

[39] Einan Gardi and Georges Grunberg. The conformal window in QCD and supersymmetric QCD. *JHEP*, 03:024, 1999. arXiv:hep-th/9810192.

[40] Luigi Del Debbio, Mads T. Frandsen, Haralambos Panagopoulos, and Francesco Sannino. Higher representations on the lattice: perturbative studies. *JHEP*, 06:007, 2008. arXiv:0802.0891.

[41] T. van Ritbergen, J. A. M. Vermaseren, and S. A. Larin. The four-loop beta function in quantum chromodynamics. *Phys. Lett.*, B400:379–384, 1997. arXiv:hep-ph/9701390.

[42] Steven Weinberg. New approach to the renormalization group. *Phys. Rev.*, D8:3497–3509, 1973.

[43] Francis Bursa, Luigi Del Debbio, Liam Keegan, Claudio Pica, and Thomas Pickup. Mass anomalous dimension in SU(2) with two adjoint fermions. *Phys. Rev.*, D81:014505, 2010. arXiv:0910.4535.

[44] J. A. M. Vermaseren, S. A. Larin, and T. van Ritbergen. The 4-loop quark mass anomalous dimension and the invariant quark mass. *Phys. Lett.*, B405:327–333, 1997. arXiv:hep-ph/9703284.

[45] Roshan Foadi, Mads T. Frandsen, Thomas A. Ryttov, and Francesco Sannino. Minimal Walking Technicolor: Set Up for Collider Physics. *Phys. Rev.*, D76:055005, 2007. arXiv:0706.1696.

[46] Hidenori S. Fukano and Francesco Sannino. Conformal Window of Gauge Theories with Four-Fermion Interactions and Ideal Walking. *Phys. Rev.*, D82:035021, 2010. arXiv:1005.3340.

[47] Deog Ki Hong, Stephen D. H. Hsu, and Francesco Sannino. Composite Higgs from higher representations. *Phys. Lett.*, B597:89–93, 2004. arXiv:hep-ph/0406200.

[48] Edward Witten. An SU(2) anomaly. *Phys. Lett.*, B117:324–328, 1982.

[49] Dennis D. Dietrich, Francesco Sannino, and Kimmo Tuominen. Light composite Higgs from higher representations versus electroweak precision measurements: Predictions for LHC. *Phys. Rev.*, D72:055001, 2005. arXiv:hep-ph/0505059.

[50] Claudio Pica and Francesco Sannino. Beta Function and Anomalous Dimensions. 2010. arXiv:1011.3832.

[51] Thomas A. Ryttov and Francesco Sannino. Supersymmetry Inspired QCD Beta Function. *Phys. Rev.*, D78:065001, 2008. arXiv:0711.3745.

[52] Claudio Pica and Francesco Sannino. UV and IR Zeros of Gauge Theories at The Four Loop Order and Beyond. *Phys. Rev.*, D83:035013, 2011. arXiv:1011.5917.

[53] Simon Catterall and Francesco Sannino. Minimal walking on the lattice. *Phys. Rev.*, D76:034504, 2007. arXiv:0705.1664.

[54] Luigi Del Debbio, Agostino Patella, and Claudio Pica. Higher representations on the lattice: numerical simulations. SU(2) with adjoint fermions. *Phys. Rev.*, D81:094503, 2010. arXiv:0805.2058.

[55] Simon Catterall, Joel Giedt, Francesco Sannino, and Joe Schneible. Phase diagram of SU(2) with 2 flavors of dynamical adjoint quarks. *JHEP*, 11:009, 2008. arXiv:0807.0792.

[56] Luigi Del Debbio, Agostino Patella, and Claudio Pica. Fermions in higher representations. Some results about SU(2) with adjoint fermions. *PoS*, LATTICE2008:064, 2008. arXiv:0812.0570.

[57] Ari J. Hietanen, Jarno Rantaharju, Kari Rummukainen, and Kimmo Tuominen. Spectrum of SU(2) lattice gauge theory with two adjoint Dirac flavours. *JHEP*, 05:025, 2009. arXiv:0812.1467.

[58] Ari Hietanen, Jarno Rantaharju, Kari Rummukainen, and Kimmo Tuominen. Spectrum of SU(2) gauge theory with two fermions in the adjoint representation. *PoS*, LATTICE2008:065, 2008. arXiv:0810.3722.

[59] L. Del Debbio, B. Lucini, A. Patella, C. Pica, and A. Rago. Conformal vs confining scenario in SU(2) with adjoint fermions. *Phys. Rev.*, D80:074507, 2009. arXiv:0907.3896.

[60] Claudio Pica, Luigi Del Debbio, Biagio Lucini, Agostino Patella, and Antonio Rago. Technicolor on the Lattice. 2009. arXiv:0909.3178.

[61] Luigi Del Debbio, Biagio Lucini, Agostino Patella, Claudio Pica, and Antonio Rago. Mesonic spectroscopy of Minimal Walking Technicolor. *Phys. Rev.*, D82:014509, 2010. arXiv:1004.3197.

[62] Luigi Del Debbio, Biagio Lucini, Agostino Patella, Claudio Pica, and Antonio Rago. The infrared dynamics of Minimal Walking Technicolor. *Phys. Rev.*, D82:014510, 2010. arXiv:1004.3206.

[63] Ari J. Hietanen, Kari Rummukainen, and Kimmo Tuominen. Evolution of the coupling constant in SU(2) lattice gauge theory with two adjoint fermions. *Phys. Rev.*, D80:094504, 2009. arXiv:0904.0864.

[64] Thomas DeGrand, Yigal Shamir, and Benjamin Svetitsky. Infrared fixed point in SU(2) gauge theory with adjoint fermions. 2011. arXiv:1102.2843.

[65] Markus A. Luty. Strong Conformal Dynamics at the LHC and on the Lattice. *JHEP*, 04:050, 2009. arXiv:0806.1235.

[66] Jamison Galloway, Jared A. Evans, Markus A. Luty, and Ruggero Altair Tacchi. Minimal Conformal Technicolor and Precision Electroweak Tests. *JHEP*, 10:086, 2010. arXiv:1001.1361.

[67] Zoltan Fodor, Kieran Holland, Julius Kuti, Daniel Nogradi, and Chris Schroeder. Probing technicolor theories with staggered fermions. *PoS*, LATTICE2008:066, 2008. arXiv:0809.4890.

[68] Albert Deuzeman, Maria Paola Lombardo, and Elisabetta Pallante. The physics of eight flavours. *Phys. Lett.*, B670:41–48, 2008. arXiv:0804.2905.

[69] Albert Deuzeman, Maria Paola Lombardo, and Elisabetta Pallante. The physics of eight flavours. *PoS*, LATTICE2008:060, 2008. arXiv:0810.1719.

[70] Albert Deuzeman, Elisabetta Pallante, Maria Paola Lombardo, and E. Pallante. Hunting for the Conformal Window. *PoS*, LATTICE2008:056, 2008. arXiv:0810.3117.

[71] A. Deuzeman, M. P. Lombardo, and E. Pallante. Evidence for a conformal phase in SU(N) gauge theories. *Phys. Rev.*, D82:074503, 2010. arXiv:0904.4662.

[72] Albert Deuzeman, Maria Paola Lombardo, and Elisabetta Pallante. Traces of a fixed point: Unravelling the phase diagram at large Nf. *PoS*, LAT2009:044, 2009. arXiv:0911.2207.

[73] Zoltan Fodor, Kieran Holland, Julius Kuti, Daniel Nogradi, and Chris Schroeder. Calculating the running coupling in strong electroweak models. *PoS*, LAT2009:058, 2009. arXiv:0911.2934.

[74] Zoltan Fodor, Kieran Holland, Julius Kuti, Daniel Nogradi, and Chris Schroeder. Chiral symmetry breaking in nearly conformal gauge theories. *PoS*, LAT2009:055, 2009. arXiv:0911.2463.

[75] Xiao-Yong Jin and Robert D. Mawhinney. Lattice QCD with Eight Degenerate Quark Flavors. *PoS*, LATTICE2008:059, 2008. arXiv:0812.0413.

[76] Zoltan Fodor, Kieran Holland, Julius Kuti, Daniel Nogradi, and Chris Schroeder. Topology and higher dimensional representations. *JHEP*, 08:084, 2009. arXiv:0905.3586.

[77] Zoltan Fodor, Kieran Holland, Julius Kuti, Daniel Nogradi, and Chris Schroeder. Nearly conformal gauge theories in finite volume. *Phys. Lett.*, B681:353–361, 2009. arXiv:0907.4562.

[78] Thomas Appelquist, George T. Fleming, and Ethan T. Neil. Lattice Study of the Conformal Window in QCD-like Theories. *Phys. Rev. Lett.*, 100:171607, 2008. arXiv:0712.0609.

[79] George T. Fleming. Strong Interactions for the LHC. *PoS*, LATTICE2008:021, 2008. arXiv:0812.2035.

[80] Thomas Appelquist, George T. Fleming, and Ethan T. Neil. Lattice Study of Conformal Behavior in SU(3) Yang-Mills Theories. *Phys. Rev.*, D79:076010, 2009. arXiv:0901.3766.

[81] Anna Hasenfratz. Investigating the critical properties of beyond-QCD theories using Monte Carlo Renormalization Group matching. *Phys. Rev.*, D80:034505, 2009. arXiv:0907.0919.

[82] Anna Hasenfratz. Conformal or Walking? Monte Carlo renormalization group studies of SU(3) gauge models with fundamental fermions. *Phys. Rev.*, D82:014506, 2010. arXiv:1004.1004.

[83] M. Hayakawa et al. Running coupling constant of ten-flavor QCD with the Schródinger functional method. 2010. arXiv:1011.2577.

[84] Thomas DeGrand and Carleton E. Detar. Lattice methods for quantum chromodynamics. New Jersey, USA: World Scientific (2006) 345 p.

[85] Martin Luscher. Advanced lattice QCD. 1998. arXiv:hep-lat/9802029.

[86] J. Smit. Introduction to quantum fields on a lattice: A robust mate. *Cambridge Lect. Notes Phys.*, 15:1–271, 2002.

[87] A. Zichichi. New Phenomena in Subnuclear Physics. Part A. Proceedings: First Half of the 1975 International School of Subnuclear Physics, Erice, Sicily, Jul 11-Aug 1 1975. New York 1977, 1-558.

[88] Marco Bochicchio, Luciano Maiani, Guido Martinelli, Gian Carlo Rossi, and Massimo Testa. Chiral Symmetry on the Lattice with Wilson Fermions. *Nucl. Phys.*, B262:331, 1985.

[89] Ferenc Niedermayer. Exact chiral symmetry, topological charge and related topics. *Nucl. Phys. Proc. Suppl.*, 73:105–119, 1999. arXiv:hep-lat/9810026.

[90] M. A. Clark and A. D. Kennedy. Accelerating Dynamical Fermion Computations using the Rational Hybrid Monte Carlo (RHMC) Algorithm with Multiple Pseudofermion Fields. *Phys. Rev. Lett.*, 98:051601, 2007. arXiv:hep-lat/0608015.

[91] K. Symanzik. Schrodinger Representation and Casimir Effect in Renormalizable Quantum Field Theory. *Nucl. Phys.*, B190:1, 1981.

[92] M. Luscher. SCHRODINGER REPRESENTATION IN QUANTUM FIELD THEORY. *Nucl. Phys.*, B254:52–57, 1985.

[93] Martin Luscher, Rajamani Narayanan, Peter Weisz, and Ulli Wolff. The Schrodinger functional: A Renormalizable probe for nonAbelian gauge theories. *Nucl. Phys.*, B384:168–228, 1992. arXiv:hep-lat/9207009.

[94] Stefan Sint. On the Schrodinger functional in QCD. *Nucl. Phys.*, B421:135–158, 1994. arXiv:hep-lat/9312079.

[95] Stefan Sint and Peter Weisz. The running quark mass in the SF scheme and its two-loop anomalous dimension. *Nucl. Phys.*, B545:529–542, 1999. arXiv:hep-lat/9808013.

[96] Martin Luscher, Rainer Sommer, Ulli Wolff, and Peter Weisz. Computation of the running coupling in the SU(2) Yang- Mills theory. *Nucl. Phys.*, B389:247–264, 1993. arXiv:hep-lat/9207010.

[97] Stefan Sint and Rainer Sommer. The Running coupling from the QCD Schrodinger functional: A One loop analysis. *Nucl. Phys.*, B465:71–98, 1996. arXiv:hep-lat/9508012.

[98] Martin Luscher, Stefan Sint, Rainer Sommer, and Peter Weisz. Chiral symmetry and O(a) improvement in lattice QCD. *Nucl. Phys.*, B478:365–400, 1996. arXiv:hep-lat/9605038.

[99] Rainer Sommer. Non-perturbative renormalization of QCD. 1997. arXiv:hep-ph/9711243.

[100] Michele Della Morte et al. Computation of the strong coupling in QCD with two dynamical flavours. *Nucl. Phys.*, B713:378–406, 2005. arXiv:hep-lat/0411025.

[101] Michele Della Morte et al. Non-perturbative quark mass renormalization in two-flavor QCD. *Nucl. Phys.*, B729:117–134, 2005. arXiv:hep-lat/0507035.

[102] Martin Luscher, Stefan Sint, Rainer Sommer, Peter Weisz, and Ulli Wolff. Non-perturbative O(a) improvement of lattice QCD. *Nucl. Phys.*, B491:323–343, 1997. arXiv:hep-lat/9609035.

[103] Michele Della Morte, Roland Hoffmann, Francesco Knechtli, Rainer Sommer, and Ulli Wolff. Non-perturbative renormalization of the axial current with dynamical Wilson fermions. *JHEP*, 07:007, 2005. arXiv:hep-lat/0505026.

[104] Stefano Capitani, Martin Luscher, Rainer Sommer, and Hartmut Wittig. Non-perturbative quark mass renormalization in quenched lattice QCD. *Nucl. Phys.*, B544:669–698, 1999. arXiv:hep-lat/9810063.

[105] Francis Bursa, Luigi Del Debbio, Liam Keegan, Claudio Pica, and Thomas Pickup. Mass anomalous dimension in SU(2) with six fundamental fermions. 2010. arXiv:1007.3067.

[106] R. H. Swendsen. Monte Carlo Renormalization Group. *Phys. Rev. Lett.*, 42:859–861, 1979.

[107] A. Hasenfratz, P. Hasenfratz, Urs M. Heller, and F. Karsch. THE beta FUNCTION OF THE SU(3) WILSON ACTION. *Phys. Lett.*, B143:193, 1984.

[108] K. C. Bowler et al. MONTE CARLO RENORMALIZATION GROUP STUDIES OF SU(3) LATTICE GAUGE THEORY. *Nucl. Phys.*, B257:155–172, 1985.

[109] A. Hasenfratz, P. Hasenfratz, Urs M. Heller, and F. Karsch. IMPROVED MONTE CARLO RENORMALIZATION GROUP METHODS. *Phys. Lett.*, B140:76, 1984.

[110] Simon Catterall, Luigi Del Debbio, Joel Giedt, and Liam Keegan. MCRG Minimal Walking Technicolor. *PoS*, LATTICE2010:057, 2010. arXiv:1010.5909.

[111] Anna Hasenfratz and Francesco Knechtli. Flavor symmetry and the static potential with hypercubic blocking. *Phys. Rev.*, D64:034504, 2001. arXiv:hep-lat/0103029.

[112] M. Albanese et al. Glueball Masses and String Tension in Lattice QCD. *Phys. Lett.*, B192:163–169, 1987.

[113] Stefan Sint. The Schroedinger functional with chirally rotated boundary conditions. *PoS*, LAT2005:235, 2006. arXiv:hep-lat/0511034.

[114] Stefan Sint. The chirally rotated Schródinger functional with Wilson fermions and automatic O(a) improvement. 2010. arXiv:1008.4857.

[115] B. Sheikholeslami and R. Wohlert. Improved Continuum Limit Lattice Action for QCD with Wilson Fermions. *Nucl. Phys.*, B259:572, 1985.

[116] Tuomas Karavirta, Kimmo Tuominen, Anne-Mari Mykkanen, Jarno Rantaharju, and Kari Rummukainen. Perturbative improvement of SU(2) gauge theory with two Wilson fermions in the adjoint representation. *PoS*, LATTICE2010:056, 2010. arXiv:1011.2057.

[117] Tuomas Karavirta, Anne Mykkanen, Jarno Rantaharju, Kari Rummukainen, and Kimmo Tuominen. Nonperturbative improvement of SU(2) lattice gauge theory with adjoint or fundamental flavors. 2011. arXiv:1101.0154.

[118] M. Luscher and P. Weisz. O(a) improvement of the axial current in lattice QCD to one-loop order of perturbation theory. *Nucl. Phys.*, B479:429–458, 1996. `arXiv:hep-lat/9606016`.

[119] Robert G. Edwards and Balint Joo. The Chroma software system for lattice QCD. *Nucl. Phys. Proc. Suppl.*, 140:832, 2005. `arXiv:hep-lat/0409003`.

[120] Biagio Lucini and Gregory Moraitis. Determination of the running coupling in pure SU(4) Yang- Mills theory. *PoS*, LAT2007:058, 2007. `arXiv:0710.1533`.

[121] Martin Luscher, Rainer Sommer, Peter Weisz, and Ulli Wolff. A Precise determination of the running coupling in the SU(3) Yang-Mills theory. *Nucl. Phys.*, B413:481–502, 1994. `arXiv:hep-lat/9309005`.

Publications

S. Catterall, L. Del Debbio, J. Giedt and L. Keegan.
"MCRG Minimal Walking Technicolor."
PoS **LATTICE2010** 057 (2010). arXiv:1010.5909 [hep-ph].

F. Bursa, L. Del Debbio, L. Keegan, C. Pica and T. Pickup.
"Mass anomalous dimension in SU(2) with six fundamental fermions."
PoS **LATTICE2010** 070 (2010). arXiv:1010.0901 [hep-ph].

F. Bursa, L. Del Debbio, L. Keegan, C. Pica and T. Pickup.
"Mass anomalous dimension in SU(2) with six fundamental fermions."
Phys. Lett. B **696**(4), 374 (2011). arXiv:1007.3067 [hep-ph].

F. Bursa, L. Del Debbio, L. Keegan, C. Pica and T. Pickup.
"Mass anomalous dimension in SU(2) with two adjoint fermions."
Phys. Rev. D **81**, 014505 (2010). arXiv:0910.4535 [hep-ph].

F. Bursa, L. Del Debbio, L. Keegan, C. Pica, and T. Pickup.
"Running of the coupling and quark mass in SU(2) with two adjoint fermions."
PoS **LAT2009** 056 (2009). arXiv:0910.2562 [hep-ph].

Glossary

BSM	Beyond Standard Model, (page i)
ETC	Extended Technicolor, (page 4)
EWSB	Electroweak Symmetry Breaking, (page i)
FCNC	Flavor Changing Neutral Current, (page 5)
IRFP	Infrared Fixed Point, (page i)
LHC	Large Hadron Collider, (page i)
MCRG	Monte Carlo Renormalisation Group, (page i)
MCT	Minimal Conformal Technicolor, (page 12)
MWT	Minimal Walking Technicolor, (page 10)
PCAC	Partially Conserved Axial Current, (page 25)
RHMC	Rational Hybrid Monte Carlo, (page 91)
SF	Schrödinger Functional, (page 22)
TC	Technicolor, (page 4)